AD-A084 863 ARMY MILITARY PERSONNEL CENTER ALEXANDRIA VA F/G 20/8
THE Z2/A DEPENDENCE IN HEAVY-ION FUSION FOR THE REACTIONS OF CH--ETC(U)
JUN 80 A C DIRIENZO

UNCLASSIFIED NL

1 OF 2
AD
A084863

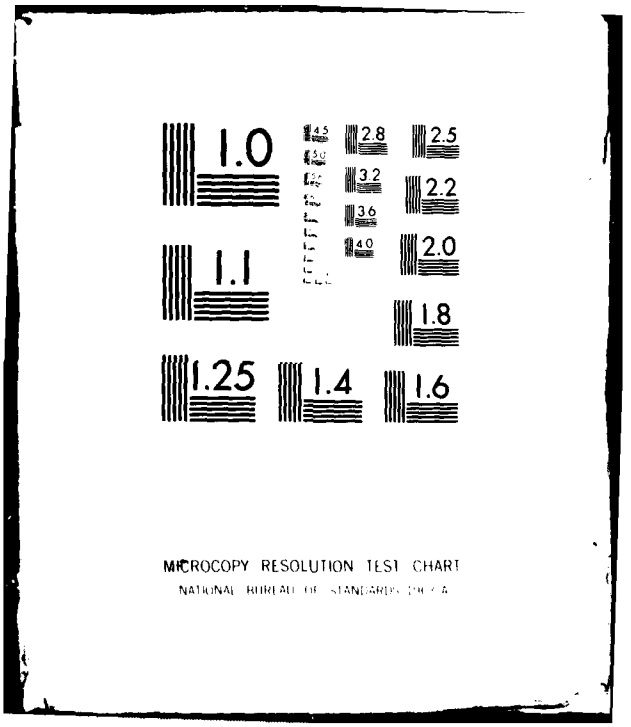
1.0
1.1
1.25
1.4
1.6
1.8
2.0
2.2
2.5
2.8
3.2
3.6
4.0
4.5
5.0
MICROCOPY RESOLUTION TEST CHART
NATIONAL BUREAU OF STANDARDS 1963-A

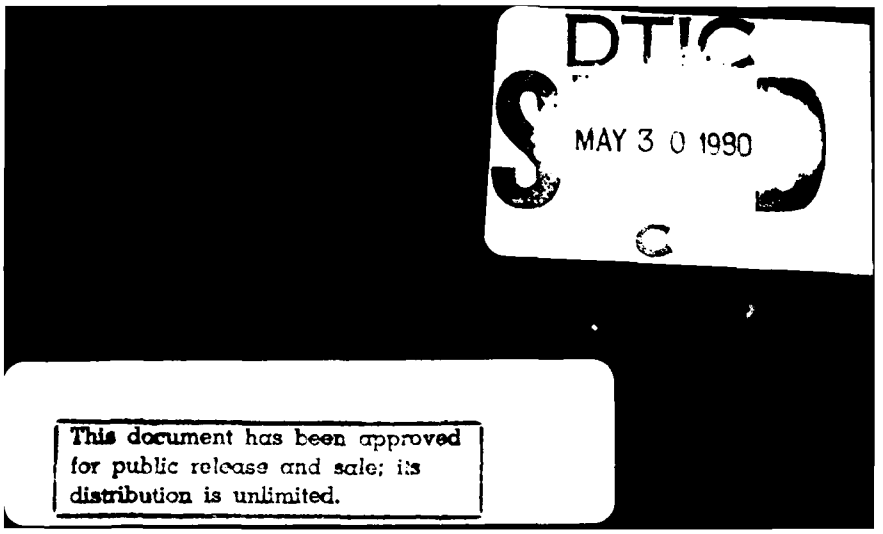
DTIC
MAY 3 0 1990
This document has been approved for public release and sale; its distribution is unlimited.

SECURITY CLASSIFICATION OF THIS PAGE (When Data Entered)

REPORT DOCUMENTATION PAGE		READ INSTRUCTIONS BEFORE COMPLETING FORM
1. REPORT NUMBER	2. GOVT ACCESSION NO. AD-A084863	3. RECIPIENT'S CATALOG NUMBER
4. TITLE (and Subtitle) The Z^2/A Dependence in Heavy Ion Fusion for the Reactions of Chlorine on Thulium [illegible], Tantalum and Tungsten		5. TYPE OF REPORT & PERIOD COVERED Final Report 7May 1980
		6. PERFORMING ORG. REPORT NUMBER
7. AUTHOR(s) Anthony C. DiRienzo		8. CONTRACT OR GRANT NUMBER(s)
9. PERFORMING ORGANIZATION NAME AND ADDRESS Student, HQDA, MILPERCEN (DAPC-OPP-E), 200 Stovall Street, Alexandria, VA 22332		10. PROGRAM ELEMENT, PROJECT, TASK AREA & WORK UNIT NUMBERS
11. CONTROLLING OFFICE NAME AND ADDRESS HQDA, MILPERCEN, ATTN: DAPC-OPP-E, 200 Stovall Street, Alexandria, VA 22332		12. REPORT DATE 7 May 1980
		13. NUMBER OF PAGES 133
14. MONITORING AGENCY NAME & ADDRESS (if different from Controlling Office)		15. SECURITY CLASS. (of this report) UNCLASSIFIED
		15a. DECLASSIFICATION/DOWNGRADING SCHEDULE

16. DISTRIBUTION STATEMENT (of this Report)

Approved for public release; distribution unlimited.

17. DISTRIBUTION STATEMENT (of the abstract entered in Block 20, if different from Report)

18. SUPPLEMENTARY NOTES

Thesis, S.M. Degree, Mass. Institute of Technology, Heavy Ion Group, Laboratory for Nuclear Science.

19. KEY WORDS (Continue on reverse side if necessary and identify by block number)

Prepared in conjunction with Dr. Harald Enge's work with Heavy Ion particle beams at Brookhaven Nat'l Laboratory. Presented at American Physical Society Conference, Heavy Ion Session, April 1980. Possible publication in Physical Review. cont

20. ABSTRACT (Continue on reverse side if necessary and identify by block number)

Evaporation residues produced in the reactions 35Cl+169Tm and 37Cl+169Tm, 175Lu, 181Ta and 186W were observed at zero degree utilizing the Mass Inst of Tech.- Brookhaven Nat'l Lab Recoil Mass Spectrometer. The recoiling nuclei were separated from the beam and refocused onto a surface barrier detector by a combination of electrostatic and magnetic fields and magnetic quadrupole lenses. The residual nuclei are alpha radioactive

DD FORM 1 JAN 73 1473 EDITION OF 1 NOV 65 IS OBSOLETE

SECURITY CLASSIFICATION OF THIS PAGE (When Data Entered)

19. Key Words: Heavy Ion Fusion
Particle Beam Control
Statistical Evaporation Codes
Stability of Heavy Nuclei

20. Abstract:
and can thus be identified by a characteristic alpha line observed after the arrival pulse of the evaporation residue. The recoiling nuclei also pass through a gas ionization chamber whereas the decay alpha do not. A separate anti-coincidence spectrum therefore displayed the alphas background free. Trends of evaporation residue cross section were charted versus Z²(proton #)/ A(atomic#) and compared to statistical evaporation codes.

Z²/A

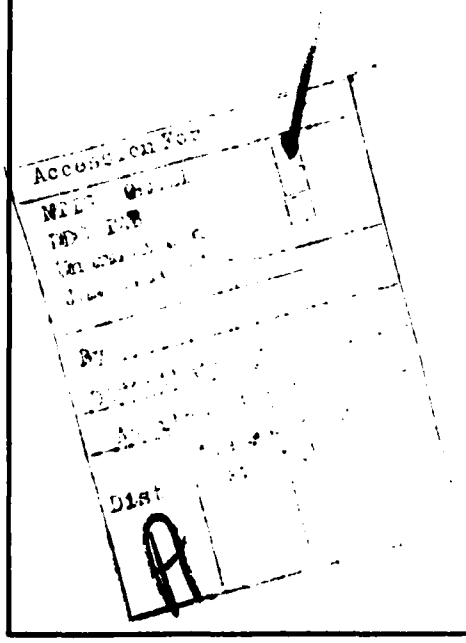

THE Z^2/A DEPENDENCE IN HEAVY-ION FUSION FOR THE REACTIONS OF CHLORINE ON THULIUM, LUTETIUM, TANTALUM AND TUNGSTEN.

by

ANTHONY CHARLES DiRIENZO

B.S., United States Military Academy
(1972)

SUBMITTED IN PARTIAL FULFILLMENT
OF THE REQUIREMENTS FOR THE
DEGREE OF

MASTER OF SCIENCE

at the

MASSACHUSETTS INSTITUTE OF TECHNOLOGY

JUNE 1980

Signature of Author.....
Department of Physics, May 5 , 1980

Certified by.....
Thesis Supervisor

Accepted by.....
George F. Koster, Chairman, Department Committee

THE Z^2/A DEPENDENCE IN HEAVY-ION FUSION FOR THE REACTIONS OF CHLORINE ON THULIUM, LUTETIUM, TANTALUM AND TUNGSTEN

by

ANTHONY CHARLES DiRIENZO

Submitted to the Department of Physics on May 5, 1980 in partial fulfillment of the requirements for the Degree of Master of Science.

ABSTRACT

Evaporation residues produced in the reactions 35Cl+169Tm and 37Cl+169Tm,175Lu,181Ta and 186W were observed at zero degree utilizing the MIT-BNL Recoil Mass Separator (RMS). The recoiling nuclei were separated from the beam and refocused onto a surface barrier detector by a combination of electrostatic and magnetic fields and magnetic quadrupole lenses. The residual nuclei are alpha radioactive and can thus be identified by a characteristic alpha line observed after the arrival pulse of the evaporation residue. The recoiling nuclei also passed through a gas ionization chamber whereas the decay alpha did not. A separate anticoincidence spectrum therefore displayed the alphas background free. Trends of evaporation residue cross section were charted versus Z^2/A and compared to statistical evaporation codes.

Thesis Supervisor: H.A.Enge
Title: Professor of Physics

For Fanny

ACKNOWLEDGEMENTS

First, and foremost, I would like to thank my thesis advisor, Professor Harald A. Enge for his patience and subtle guidance throughout my studies. His emminence in the field of ion optics was continually demonstrated to me. I am grateful for the opportunity to absorb even a small portion of his knowledge.

This thesis is not the result of individual effort but instead a chronical of the work of many individuals and I wish to express my appreciation to those who shared in the task.

Anthony Sperduto, who made my transition into the Heavy Ion Group most enjoyable, deserves my thanks for his assistance during all of the BNL runs, APS meetings and laboratory work. Anthony Luongo, who made the targets, provided invaluable advice on many subjects. Robert Ledoux, a good friend, provided theoretical and electronic advice and made my stay at MIT most enjoyable. Matti Salomaa's ability to keep the electronic black boxes working deserves my special thanks. I would like also to extend my appreciation to Dr. Martin Beckerman for his teaching me the use and interpretation of the ALICE and MBII codes.

Also deserving of thanks are John Molitoris, who helped on runs, Joel Karp and Stuart Gazes who provied computer support, John Elliot who provided the regression analysis and Ed Druek who provided BNL support. Debi Lauricella deserves appreciation for

(2)

THE Z^2/A DEPENDENCE IN HEAVY ION FUSION FOR THE REACTIONS OF CHLORINE ON THULIUM, LUTETIUM, TANTALUM AND TUNGSTEN

CPT ANTHONY C. DIRIENZO
HQDA, MILPERCEN (DAPC-OPP-E)
200 Stovall Street
Alexandria, VA 22332

Final report 7 May 1980

A thesis submitted to the Massachusetts Institute of Technology, Cambridge MA in partial fulfillment of the requirements for the degree of Master of Science.

the masterful typing of this draft. Finally, my special thanks to Dr. Walter Schier who provided leadership, insight and expertise throughout the study.

TABLE OF CONTENTS

LIST OF ILLUSTRATIONS

LIST OF TABLES

CHAPTER I

INTRODUCTION

Since the Second World War, the alchemists dream of transmutation has become a commonplace, if not very economical event. The table nuclides has been increased in both length and breadth and there are now more than a thousand known nuclides. The table has been extended far past the fringe of the line of stability on a curve of Z vs. N to include very large nuclei that are unstable to spontaneous fission and alpha decay. The chart has also been considerably extended toward the proton drip line where beta decay predominates on the fringe and alpha decay toward the center. While there is no expectation of finding stable nuclei at these fringe areas, their production serves to further the limited body of knowledge concerning the systematics of the stability of nuclei to various decays as well as further refining the machinery for their production and detection. The other direction of search, at higher A, has resulted in a logjam near element 105 due primarily to the increased fission competition. The various methods of heavy ion fusion to produce these more and more massive systems have resulted in little success. This may be the result of theoretical inadequacies in the fusion reactions producing transfermium nuclides or in the methodology and apparatus used to form and detect them.

For many years there has been an effort to produce nuclides far beyond the fringe of the line of stability; the superheavy nuclei. The destabilizing effects of the large Coulomb repulsion should be overcome by the stabilizing effects of the closed proton shell at 114, 116 or possibly 126. Many avenues of approach have been attempted to achieve fusion coupled with survival from fission in this area, but to no avail utilizing any of the present heavy ion accelerators.

One method is to bombard a very heavy nuclide with another very heavy one such as uranium on uranium. Here it is hoped that the massive compound nucleus would fission with one fragment in the super heavy region. A transfer reaction may also take place between two massive nuclei producing a superheavy. Some modest attempts at these reactions have been unsuccessful so far and it is felt that the superheavy fragment may be produced in such an elongated state as to fission itself.

Several interesting programs have been undertaken to search for superheavy nuclei. The Russians[1] (Flerov, 1972) have studied medieval stained glass windows on the premise that a superheavy nuclei, chemically similar to lead, could be found in lead glass. A British group[2] (Marinov, et al., 1971) studied tungsten beam stops from the 30 GeV CERN proton synchrotron. They estimated that a recoiling tungsten nucleus, after stopping a 30 GeV proton, would have sufficient energy to fuse with another tungsten nucleus. It was hoped that a long-lived superheavy nucleus might be a fission

product of such a reaction. Terrestrial ores, lead and platinum, have been studied and nuclear emulsions exposed to high altitude cosmic rays have been searched for extra-terrestrial superheavies. All of these attempts have failed.

Another, more promising method has been to bombard a heavy nuclide with a medium ion such as ^{48}Ca (e.g., $^{48}Ca + ^{248}Cm \rightarrow ^{296}116^*$). Reactions of this type in the superheavy compound nucleus region have also been unsuccessful so far. The problem has been the dependence of stability against fission on the excitation of the compound nucleus. It is not known whether production of a "cold" nucleus to minimize fission is favored by more spherical or deformed nuclei. Currently a modest study (below uranium) of the dependence of fusion on the excitation of the compound nucleus is being conducted by the M.I.T. Heavy Ion Group, which has studied the reactions:

$$^{65}Cu + ^{139}La \rightarrow ^{204}Rn \qquad E_{ex} = 35\text{-}50 \text{ MeV}$$

$$^{35}Cl + ^{169}Tm \rightarrow ^{204}Rn \qquad E_{ex} = 42\text{-}72 \text{ MeV}$$

The lack of success in producing any of several superheavy elements is cause to reevaluate the theoretical and experimental techniques involved. The concept of the stability of the Coulomb barrier may need revision since there is some suggestion that under the distortion of heavy ion interactions the increased oblateness of the projectile results in an increased barrier.[3] The liquid

drop model may also be lacking in its failure to predict the resistance to deformation for both spherical and permanently deformed nuclei.[4] Experimental modifications need also to be made to enhance the detection of fusion products and to further resolve the peculiar energies of their decay.

Compound nucleus formation, using a relatively light projectile and a heavy target nucleus, continues to give copious results and that is the method followed in this work and by the M.I.T. Heavy Ion Group.

In order to methodically attack the problem of production of superheavy nuclei, a deliberate approach has been conducted in compound nucleus formation in known regions of the chart in order to gain an insight into the mechanisms of compound nucleus formation and to validate or modify current theories.

The M.I.T. Heavy Ion Group has aggressively pursued this methodical approach and has conducted or has approval to conduct(*) the following reactions:

$^{32}S + {}^{58}Ni$

$^{32}S + {}^{70}Ge$

$^{32}S + {}^{112}Sn$

$^{58}Ni + {}^{58}Ni^{**}$

$^{58}Ni + {}^{64}Ni^{**}$

$^{64}Ni + {}^{64}Ni^{**}$

$^{32}S + {}^{144}Sm$

$^{35}Cl + {}^{169}Tm^{+}$

$^{65}Cu + {}^{139}La^{+}$

$^{37}Cl + {}^{169}Tm^{\dagger}$

$^{37}Cl + {}^{175}Lu^{\dagger}$

$^{37}Cl + {}^{181}Ta^{\dagger}$

$^{37}Cl + {}^{186}W^{\dagger}$

$^{40}Ca + {}^{161,162,163,164}Dy^{*}$

Foot Notes

†present work

$^{+}$cold nucleus

*extension of compound nucleus along line at constant Z.

**sub barrier fusion.[5]

These reactions have been selected since the predicted stable superheavy elements should be proton rich. With the exception of the Tungsten Reaction and the Dysprosium group(*) the most proton deficient isotope has been selected to give a proton rich compound nucleus that falls in the area of alpha decay.

The experiments described in this work, ^{37}Cl on ^{169}Tm, ^{175}Lu, ^{181}Ta and ^{186}W are a continuation of the Heavy Ion Group's program. This set of reactions was chosen for its gradual, short stepped, march up the chart of nuclides. This work is an attempt to quantify the Z^2/A dependence of the fusion cross section and to compare it with existing theory, primarily the ALICE code.[6] It was seen immediately that the cross section diminished rapidly at each step and these four reactions were taken to test the validity of the ALICE predictions.

Here is where the limitations of the detection device became paramount. While the ALICE code predicts a certain cross section that takes into account all compound nucleus evaporation residues, the "machine" does not detect them all due to its limited angular, charge and velocity acceptance. The kinematics program BETH[7] was utilized to specify the angular and velocity distributions of compound nucleus formation. The code RAYTRACE[8] was used to quantify the charge and velocity acceptance for the apparatus.

The term "evaporation residue", above, is used to explain what happens to the compound nucleus after fusion and coalescence has occurred. The compound nucleus, highly excited, will normally

fission. However, a small fraction will survive to undergo particle evaporation. This highly excited nucleus then de-excites by neutron, proton and alpha particle emission. The large nucleus left after emission of a few particles is the evaporation residue. These then embed themselves in a solid state detector and decay by alpha emission with discrete, identifiable, energies. All experiments are conducted at Brookhaven National Laboratory utilizing the Tandem Van de Graaff Generator to provide a copious beam of ions and the M.I.T. Recoil Mass Separator (RMS) to separate fusion products from the beam particles. This separation is necessary since simple momentum considerations show the fusion products to be forward scattered within less than 4° on the beam line. With such small cross sections involved, it is imperative to move these precious few products out of line and focus them into a single high resolution, solid state detector. This the RMS does.

What follows is but a small portion of the variety of experiments of the Heavy Ion Group. Concurrent and complementary experiments have been conducted at Berkeley and Darmstadt and it is hoped that, as the body of knowledge concerning the formation and stability of compound nuclei increases, and as larger accelerators are brought on line, that the theory of superheavy formation will come to fruition.

CHAPTER II

THEORY

A. General

Any group of theories that concerns itself with such a tremendously complex subject as heavy nuclei must, of course, have an empirical basis. Coefficients and form factors and "normalizations" are needed for a theory to match any collected data. Some theories, such as the shell model, work only for specific nuclei in specific states. Usually, in attempting to fit theory to data, or vice versa, more questions are raised than answered. This, reasonably enough, is how the model is improved and is a basis for careful experimentation, in order to minimize errors in the refinement of existing theory. The work presented here, hopefully, both adds refinement to existing theoretical models as well as improve the equipment utilized in that refinement.

B. Reactions Between Complex Nuclei

When two complex nuclei enter into collisions, two main classes of phenomena may occur.

When the system follows a grazing trajectory, elastic scattering is the dominant effect and only the extreme tails of the nuclear matter densities overlap. The total cross section is a

function of the summation of partial waves of ℓ values. Grazing interactions are related to the largest ℓ waves whose transmission coefficient T_ℓ is near zero. (See Figure 1.)

Figure 2 represents the two-body interaction potential restricted to one dimension. It consists of the nuclear and coulomb potentials for s-wave interactions. The fusion barrier is defined as the height of the interaction potential at zero slope. The intention is that at a zero slope potential the system can be trapped sufficiently long for fusion to occur. The "effective" radius is defined as that which is found when the fusion barrier is equated to the coulomb potential. Neglecting the nuclear potential will result in an effective radius larger than the actual fusion radius. As target and projectile charge (and therefore coulomb forces) increase, a larger nuclear potential is necessary to offset the greater Coulomb repulsion.

It is obvious that when a compound nucleus is formed a large portion of the kinetic energy is transformed into excitation energy of the compound system. This fraction is equal to $A_2/(A_1 + A_2)$. Fragments of this compound system possess a kinetic energy much smaller than the entrance channel kinetic energy, showing that nuclear matter has been exchanged.[9] As was suggested by Cohen, et al. (1974),[10] a composite nucleus is formed for a system that "may well correspond to an intimate contact of transient amalgamation of target and projectile." If this fused system lasts for a sufficiently

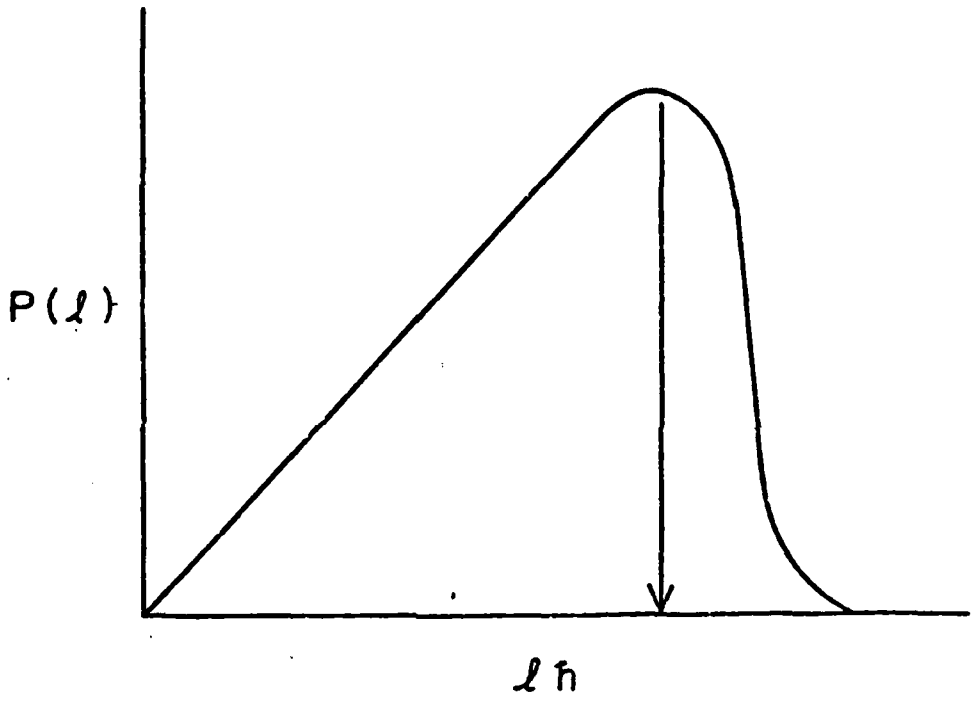

PARTIAL WAVE CROSS SECTION SUMMATION

FIGURE 1

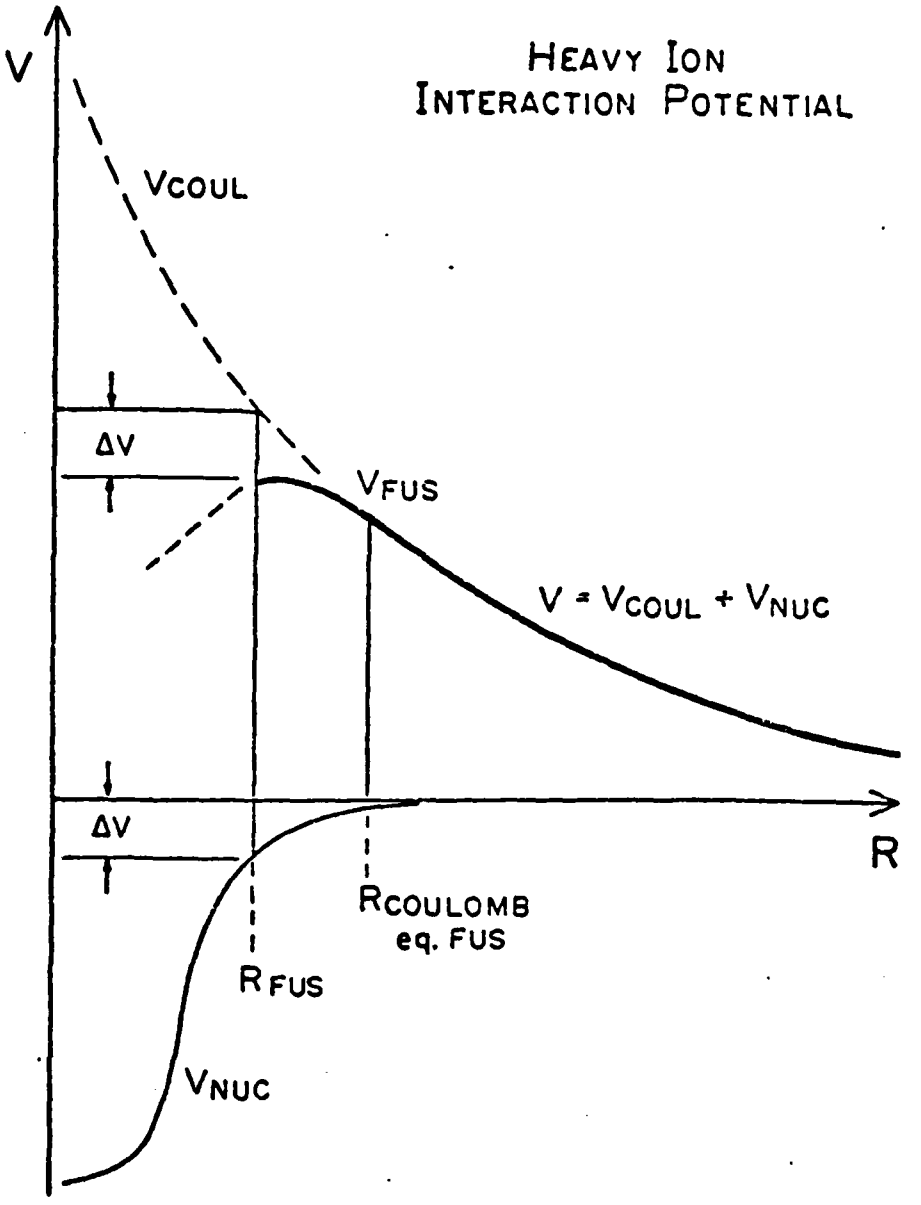
HEAVY ION
INTERACTION POTENTIAL
V
VCOUL
ΔV
VFUS
V = VCOUL + VNUC
ΔV
R
RCOULOMB
eq. FUS
RFUS
VNUC

FIGURE 2

long time, it is called a compound nucleus.

Compound nucleus formation has several features that allow simple methods of analysis and yet are sensitive to particular aspects of nuclear structure. For the reaction to take place, the projectile nucleus must over the coulomb barrier between itself and the target. $E_{CB} = Z_1 Z_2 e^2/R$ where $R = R_1 + R_2$ is the separation of the centers of the two ions. At the coulomb barrier energies, the corresponding heavy ion wavelengths are much less than their radii so that their motion is similar to that of a classical particle. (See Table I.)

$$E_{CB} = \frac{Z_1 Z_2 e^2}{R_1 + R_2}; \quad E_{LAB} = \frac{m + M}{m} E_{CB}; \quad \lambda\!\!\!^{-} = \left[\frac{\hbar^2}{2mE_{LAB}}\right]^{\frac{1}{2}}; \quad R_1, R_2 = r_o A^{1/3}$$

Absorption of a complex projectile by a complex target means that, after a time, the nucleus of both take on new characteristics in a single nuclear potential.[11] The total mass $(A_1 + A_2)$ recoils with an energy $E_R = E_i A_1/(A_1 + A_2)$ in the direction defined by the incoming projectile A_1 with incident energy E_i. Since the nucleus is highly excited by this stage, it quickly de-excites. This poses problems for its detection unless the path of its de-excitation is known and the de-excited "evaporation residues" are easy to identify. From the simple kinematics above, it is obvious that any fused nuclei will be forward scattered in the direction of the beam and, of course, have a much greater mass $(A_1 + A_2)$ than either the beam or any knocked out target nuclei. The angular distribution of the compound nucleus is within quite a small range as can be seen in the

TABLE I

Wavelengths of the Projectiles in the Laboratory System

Projectile (m)	Target (M)	Coulomb Barrier E_B (MeV)	E_{lab} (MeV)	$\lambda\!\!\!^{-}_{proj}$ (fm)	$R_1 + R_2$** (fm)
* ^{12}C	^{12}C	7.9	15.7	1.15	6.59
* ^{40}Ca	^{120}Sn	119.7	159.6	0.36	12.03
† ^{37}Cl	^{169}Tm	132.2	161.1	0.37	12.76
† ^{37}Cl	^{186}W	138.9	166.6	0.36	13.02
* ^{40}Ca	^{208}Pb	175.5	209.2	0.32	13.46
*^{208}Pb	^{208}Pb	567.4	1134.9	0.14	17.06

*Hodgson, Nuclear Heavy Ion Reactions, Ch. 4, Oxford 1978.

†Present Work

**$R_1, R_2, = 1.44\ A^{1/3}$

angular distribution figures accompanying the experimental results. Nearly all of the distribution is within 8 degrees of the beam direction.

Since the compound nucleus formation cross section, σ_{CN}, is less than the reaction cross section, σ_R, the compound nucleus formation cross section is therefore the sum of all cross section σ_ℓ up to ℓ_{CR}:

$$\sigma_{CN} = \pi\lambda\!\!\!^{-2} \sum_{\ell=0}^{\ell_{CR}} (2\ell + 1)\, T_\ell$$

where ℓ_{CR} is some critical angular momentum beyond which there is no more contribution to compound nucleus formation and T_ℓ is the transmission coefficient for a particular ℓ value. One of the simplest modes that is often compared to experiment is due to Bass (1973).[12] The critical value ℓ_{CR} is determined by estimating the balance between centrifugal, coulomb and nuclear forces in the two body system at the contact distance. Complete fusion is presumed to occur when the attractive nuclear force is larger than the sum of the centrifugal and coulomb repulsion.[13] At this point the total potential is:

$$V_{TOT} = \frac{Z_1 Z_2 e^2}{R_{12}} + \frac{\ell_{CR}(\ell_{CR} + 1)\hbar^2}{2\mu R_{12}^2} - \frac{d a_s A_1^{1/3} A_2^{1/3}}{R_{12}}$$

since the nuclear potential has the radial form

$$V_N(r) = \frac{a_s A_1^{1/3} A_2^{1/3} d}{R_{12}} \exp\left[-\frac{r + R_{12}}{d}\right]$$

where $R_{12} = r_0(A_1^{1/3} + A_2^{1/3})$

a_s is the surface energy constant in the liquid drop mass formula

d is the diffuseness parameter

μ is the reduced mass

(a_s = 17 MeV, r_0 = 1.07 fm, d = 1.35 fm)

This relation fits the increase of ℓ_{CR}^2 with the incident energy until saturation is reached

$$\ell_{CR}\hbar = \left[2\mu R_{12}^2\left(E_{cm} - \frac{Z_1Z_2e^2}{R_{12}} + \frac{da_sA_1^{1/3}A_2^{1/3}}{R_{12}}\right)\right]^{1/2}$$

$$\bar{E}_{SAT} = \frac{Z_1Z_2e^2}{R_{12}} + \frac{49}{25}\,\frac{R_{12}a_sA_1^{1/3}A_2^{1/3} - Z_1Z_2e^2}{2R_{12}} - \frac{a_sdA_1^{1/3}A_2^{1/3}}{R_{12}}$$

The factor 49/25 comes from the assumption that the angular momentum decreases by 5/7 at the point of contact (complete sticking and rigid rotation of two equal masses as a whole). Above $\bar{E}_{SAT}$, ℓ_{CR} no longer depends upon energy and this result disagrees with experiment. The sharp conversion of radial kinetic energy at the barrier assumes that there is no friction until the system reaches the barrier and then infinite friction is assumed.[14] The choice of r_0 = 1.07 is also somewhat arbitrary.

Compound nucleus formation, at the energies and masses used in this study, comprises only a small portion of the total reaction

cross section. Only a small fraction survives fission to result in evaporation residues. Due to the deep potential well to charged particles in heavy compound nuclei, the primary method of de-excitation is neutron emission except for very proton rich nuclei. However with increased excitation, the compound system can de-excite more efficiently through the emission of protons and especially alphas with their high binding energy and large angular momenta. Each excitation function rises rapidly from zero as the threshold energy is passed, attains a broad maximum and then falls due to competition from reactions emitting more neutrons. (See Figure 3.)

The energy spectra and angular distributions of particles evaporated from a compound nucleus may be calculated by semiclassical statistical theory (Weisskopf, 1937) providing the spin of the incident particle is small compared with that of the compound nucleus.[15] The probability of emission of particle γ with energy E_γ and spin S_γ in a direction θ is given by

$$\sigma(\theta,E_\gamma) = A\int_0^\infty 2JT_J dJ \frac{1}{\Gamma_\gamma}(2S_\gamma+1)\rho(E_{x\gamma},0)\times\int_0^\infty 2LT_L^{(\gamma)}\exp\left\{-\left[\frac{J^2+L^2}{2\sigma_\gamma^2}\right]J_0\left[\frac{iJL}{\sigma_\gamma^2}\right]W_{JL}(\theta E_\gamma)dL\right\}$$

where

$$W_{JL}(\theta,E_\gamma) = \frac{1}{4\pi}\left\{J_0\left[\frac{iJL}{\sigma_\gamma^2}\right]\right\}^{-1}\sum_k(-1)^k(4k+1)\left\{\frac{(2k)!}{(2^k k!)^2}\right\}^2 J_{2k}\left[\frac{iJL}{\sigma_\gamma^2}\right]P_{2k}\cos\theta$$

and T_J and T_L are the transmission coefficients in the entrance and

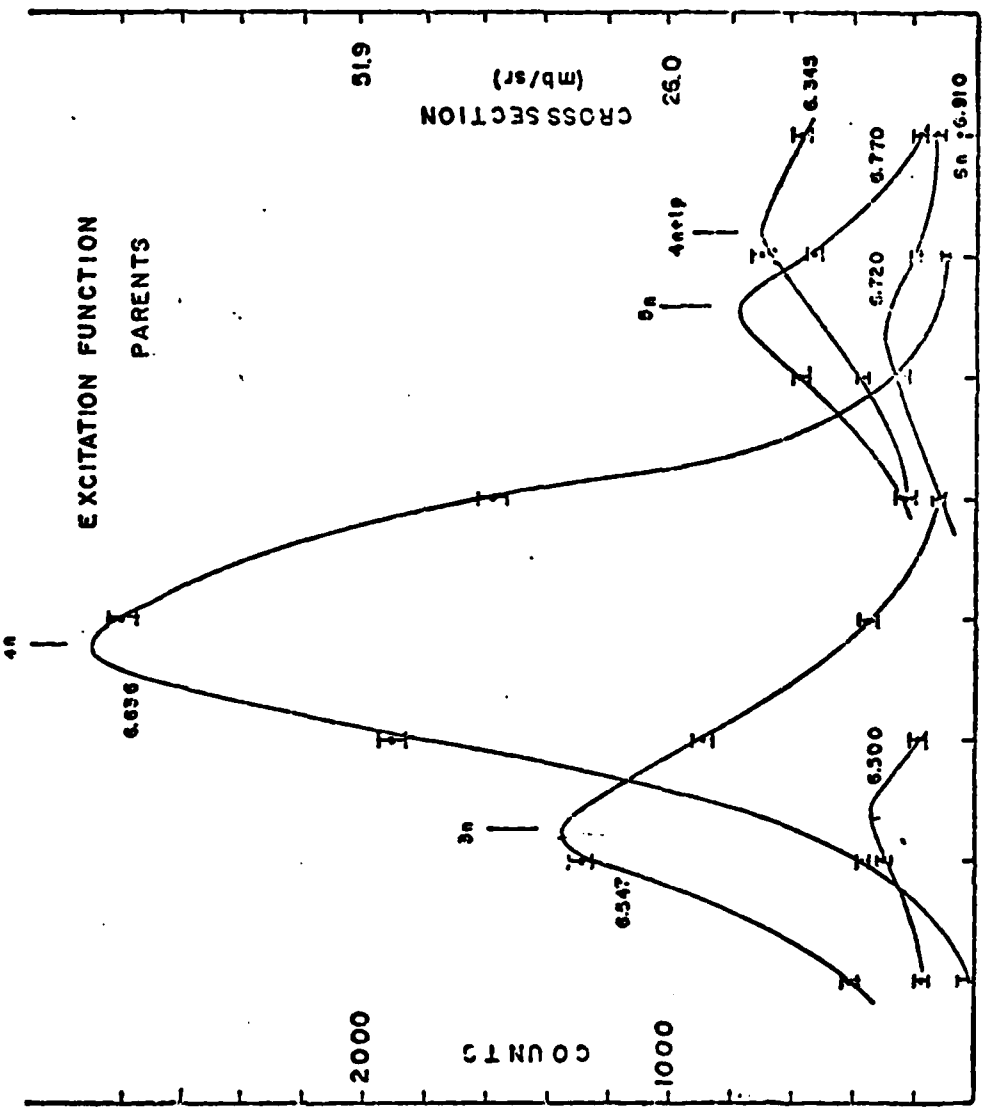
EXCITATION FUNCTION
PARENTS
CROSS SECTION
(mb/sr)
51.9
26.0
COUNTS
2000
1000
151
161
171
181
ENERGY (MeV)
4n
6.636
3n
6.547
6.300
5n
4n+1p
6.345
6.770
5n+1p
6.910
6.720

FIGURE 3

exit channels, J is the spin of the compound nucleus, L is the angular momentum of the emitted particle and Γ_J is the total decay width. The level density $\rho(E_{x\gamma},J)$ of the residual nucleus at the excitation energy $E_{x\gamma}$ and spin J may be obtained from the expression of Long (1966)[16] and Thomas (1968)[17] for the density of states with energy E and spin J.

$$\rho(E,J) = \frac{2J+1}{12\, a^{1/4}(E+t)^{5/4}(2\sigma^2)^{3/2}} \exp\left\{2(ae)^{1/2} - \frac{\left(J+\frac{1}{2}\right)^2}{2\sigma^2}\right\}$$

where t is the nuclear temperature, a is the single particle level density parameter, $\sigma^2 = I_r t/h^2$ the spin cut-off parameter and, I_r the rigid body moment of Inertia. The nuclear temperature is related to the excitation energy E by

$$E = at^2 - \frac{3}{2}t + \frac{M^2t^2}{2I}$$

The compound nucleus, in its excited state, emits a variety of particles (alphas, neutrons, protons and gammas). However, the probability of emission differs depending on both the angular momentum and excitation energy of the compound system. A system with large angular momentum favors alpha particle emission since each alpha can carry off more angular momentum than the others. When the excitation energy of the compound system is less than the neutron binding energy (and above the yrast energy) then gamma emission is favored. (Grover and Gelat, 1967)[18] Figure 4 shows the results of Grover's

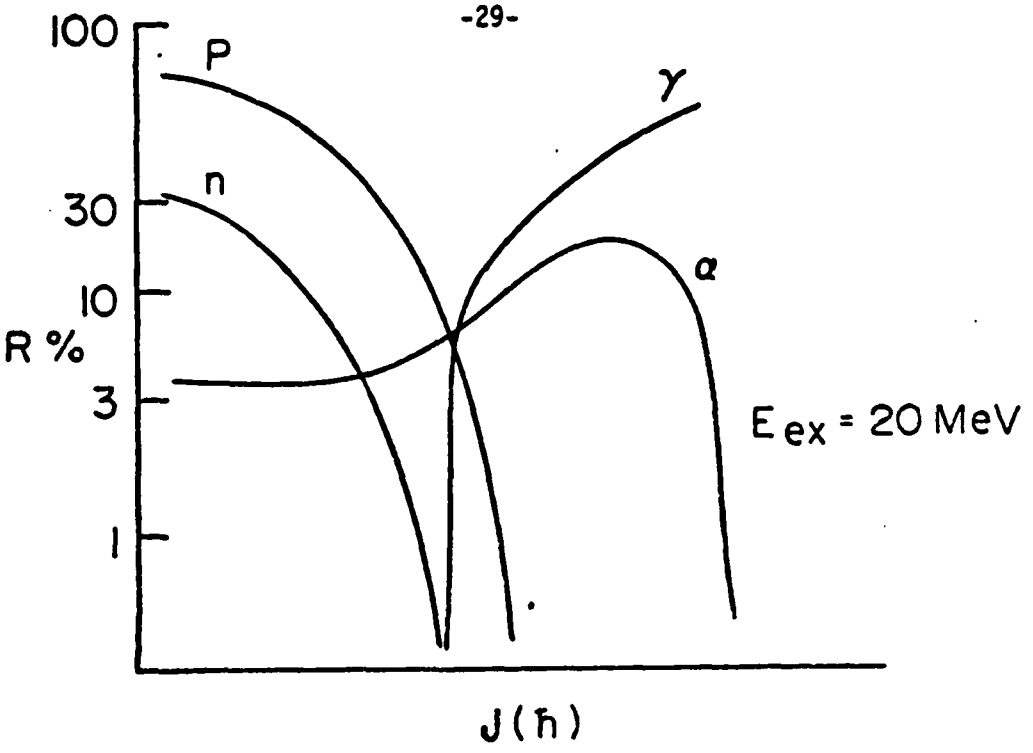

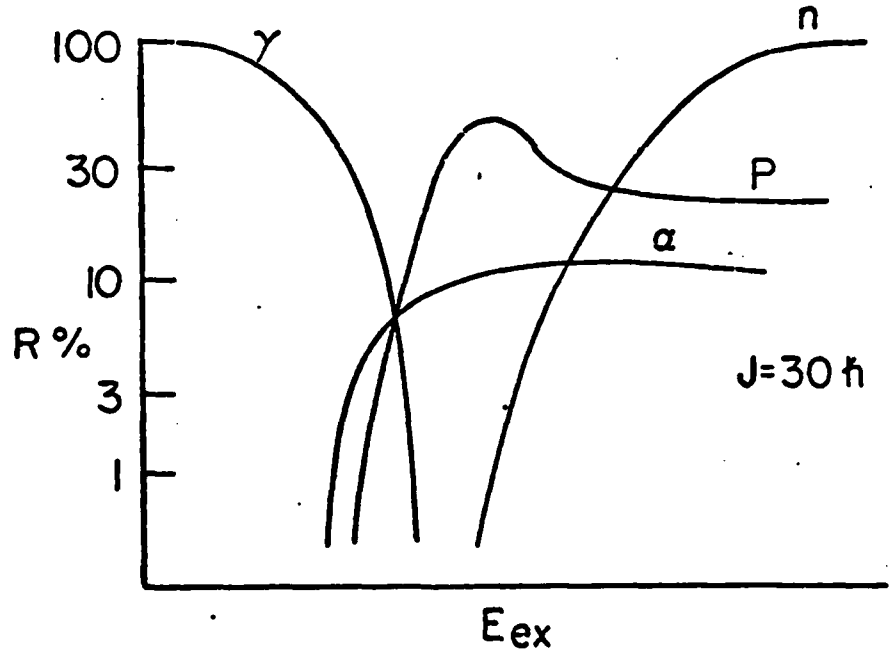

RELATIVE PROBABILITIES FOR VARIOUS PARTICLE EMISSION

FIGURE 4

calculations for ^{120}Xe.

C. Statistical Evaporation Codes

The statistical theory of Weisskopf and Ewing is utilized by the ALICE code to describe the de-excitation of a compound nucleus through particle emission. The relation

$$\rho_\nu(\varepsilon)d\varepsilon = \frac{(2s+1)_\nu\ \mu_\nu\ \varepsilon\sigma_\nu(\varepsilon)\rho(E_f)d\varepsilon}{\sum_{\nu=1}^{\mu}(2s+1)_\nu\ \mu_\nu \int_0^\infty \varepsilon\ \sigma_\nu(\varepsilon)\rho(E_f)d\varepsilon}$$

describes the probability of emission of a particle ν with energy between ε and $\varepsilon + d\varepsilon$, spin S, reduced mass μ and inverse cross section $\sigma(\varepsilon)$ from an excited nucleus to form a nucleus of level density $\rho(E_f)$. This density can be approximated by the Fermi gas level density $\rho(E, J = 0) \propto E^{-2}$, $\exp 2\sqrt{2aE}$ where a is the nuclear level density parameter taken to be about A/10 MeV^{-1}*. The assumption that $\rho(E,J) = (2J + 1)\rho(E, J = 0)$ is also made.

The evaporation code ALICE calculates the probabilities of emission of various particles for each possible step of an evaporation cascade. This then leads to a prediction of the cross section, for a specific bombardment energy, for the eventual evaporation residue. It also calculates the total reaction cross sections from the inverse

*Calculations for this study varied the parameter from A/12 to A/8.

parabolic model, the inverse reaction cross sections from the optical model and fission competition utilizing the rotating liquid drop model of Cohen, Plasil and Swiatecki.[19] As noted by D. Horn (1976)[20] the ALICE code fails to accurately decrement the probability distribution for J values in each residual nucleus once a particle has been evaporated. This deficiency is partially offset by a program option that allows specific amounts of angular momentum to be removed for each kind of particle emitted. Utilizing this option, D. Horn determined the difference to be only minimal. A second deficiency concerns the level density parameter. The level density was calculated as a function of the excitation energy E rather than E minus the rotation energy, E_{rot}.

$$\rho(E,J) \propto (2J+1)\left[E - \frac{J(J+1)\hbar^2}{2I}\right] \exp 2\sqrt{2\left(E - \frac{J(J+1)\hbar^2}{2I}\right)}$$

I = Nuclear Moment of Inertia

This more exact level density was not used nor the deficiency calculated in this study.

The inverse cross sections were calculated using the optical model with a volume absorption Woods-Saxon potential, which utilized the global parameters of Perey[21] (for proton evaporations) and of Wilmore and Hodgson[22] (for neutron evaporation). Alpha particle parameters were from the potentials of Huizenga and Igo.[23]

The following parameters were used:

A. Neutrons

$V = 47.01 - 0.267\ E - 0.00118E^2$ MeV
$W_D = 9.52 - 0.053$ MeV
$V_{so} = W_{so} - 0$ MeV
$r_o = 1.322 - (7.6 \times 10^{-4})A + (4 \times 10^{-6}A^2 - (8 \times 10^{-9})A^3$ fm
$a = 0.66$ fm
$r_D = 1.266 - (3.7 \times 10^{-4})A + (2 \times 10^{-6})A^2 - (4 \times 10^{-9})A^3$ fm
$a_D = 0.48$ fm
$W_{so} = 7.0$
$r_{so} = r_D$
$a_{so} = a_D$

B. Protons

$V = 53.3 - 0.55\ E + 27(N-Z)/A - 0.42\ A^{1/3}$
$r_o = 1.25$
$a = 0.65$
$W_D = 13.5$
$r_D = 1.25$
$a_D = 0.47$
$W_{so} = 7.5$
$r_{so} = r_D, a_{so} = a_D$

C. Alphas

$V = 50.2$
$W = 12.3$
$r_o = 1.2 + 1.5\ A^{-1/3}$
$a = 0.564$
$r_c = 1.3$

The optical model assumes that the nucleus is translucent to the incident particle wave. The projectile therefore has a specific mean free path within the nucleus; the size of the mean free path then determines if absorption occurs. The optical potential has the form:

$$V = V_c - Vf(x) - i\left[Wf(x)_w - 4W_D \frac{d}{dx} F(X_D)\right] + \left(\frac{h}{m_\pi c}\right)^2 V_{so} \vec{\sigma}\cdot\vec{\ell} \frac{1}{r} \frac{d}{dr} f(X_{so})$$

where V_c = Coulomb potential

V = Real potential

W = Volume absorption potential

W_D = Surface absorption potential

V_{so} = Spin orbit potential

$$f(x) = (1 + e^{x_b})^{-1}$$

$$x_b = (r - r_b) A^{1/3}/a_b$$

As previously mentioned, the decomposition of the total cross section into partial waves is given by:

$$\sigma_{CN} = \pi\lambda^2 \sum_{\ell=0}^{\ell_{CR}} (2\ell + 1)T_\ell$$

where the transmission coefficients T_ℓ are related to the barrier height, B, and excitation energy, E, by:

$$T_\ell = [1 + \exp\{2(B-E)/\hbar\omega_\ell\}]^{-1}$$

The ω_ℓ are the vibrational frequencies of a harmonic oscillator having a potential energy function given by -V and are related to the real part of the potential by:

$$\omega_\ell = \left|\frac{1}{m}\frac{d^2V}{dr^2}\right|^{\frac{1}{2}}$$

where V is the total potential used to determine the total fusion cross section:

$$V = \frac{Z_1 Z_2 e^2}{r} + \frac{h^2}{2\mu}\frac{\ell(\ell+1)}{r^2} - V_o \exp\left[-\frac{(r-R)}{2}\right]$$

where V_o = 67 MeV

$R = r_o(A_1^{1/3} + A_2^{1/3})$ fm

a = .57 fm

The ALICE code approximates this total potential by an inverse parabolic potential matched in position and curvature at its maximum. Nuclear binding energies are calculated by the use of the Myers-Swiatecki Mass formula.[24]

The most imperative fit that must be made with the ALICE code is the evaporation to fission ratio, or the total evaporation residue cross section. There are over 45,000[25] combinations of

options that can be selected by the user and, given a set of potentials and angular momentum parameters, the fission barrier must be adjusted. This adjustment is made by varying the ratio of single particle level densities, CLD, the level density parameter, PLD, and the barrier factor, BARFAC, in the ALICE input deck.

The most important parameters of the statistical/rotating liquid drop model are the ratios of the single particle level densities of the fissioning nuclei (at the saddle point deformation) to those of the residual (evaporating) nuclei (at the equilibrium deformation), a_f/a_ν, and the fission barriers.[26] A main objective of this work is to determine a_f/a_ν ratios and fission barriers that best fit the experimental data. Fission barriers B(I) are given by the differences between rotating energies of the nucleus at the saddle point deformation, $E_{sp}(I)$, and the rotating nucleus at the equilibrium deformation, $E_{min}(I)$.[27]

$$E_{sp}(I) = E_{min}(I) + B(I)$$

The barrier factor BARFAC or B_f was used to scale the rotating liquid drop fission barriers, B(I). This was accomplished by replacing $E_{sp}(I)$ by $E'_{sp}(I)$, where

$$E'_{sp}(I) = E_{min}(I) + B(I)B_f$$

Results of 10 different parameter sets are shown in a later chapter.

Figure 5 shows the complete fusion cross sections for the studied reactions as generated by the ALICE code. The total fusion cross section is shown only to establish a reference for l-values, whereas the ratio of fission to evaporation is the interesting quantity. The two processes are in competition at the lower l-values and there is a multiple chance for the compound nucleus to fission after each successive particle boiloff. Fission is completely dominant at the higher l-values. Figure 6 shows the evaporation residue cross sections for the studied reactions. Note that this represents the sum of all of the possible evaporation channels by which the compound nucleus can de-excite. Note also the expanded scale as well as the dashed line representing the average complete fusion cross section from the previous figure. For these reactions the evaporation residue cross sections are very small (total cross sections are obtained by integrating over all l-values) as compared to the fission cross sections.

Table II shows the measured and calculated evaporation residue cross sections, the latter determined by the ALICE code for 10 different parameter sets.

Having determined the best fit set of entry parameters to obtain a fit, or bracket, of the total evaporation residue cross section, a check must be made to determine the adequacy of the

TABLE II

Calculated and Measured Evaporation Residue Cross Sections (in μb)

PARAMETERS B_f	PLD	a_f/a_ν	$^{37}Cl + ^{169}Tm$	$^{35}Cl + ^{169}Tm$	$^{37}Cl + ^{175}Lu$	$^{37}Cl + ^{181}Ta$	$^{37}Cl + ^{186}W$
.7	A/9	1.00	603.4		19.8	2.02	9.68
.9	A/9.5	1.10	547.8		12.4	.41	1.36
.9	A/12	1.00	24853.7		3604.4	666.7	2011.9
.8	A/10	1.00	5119.4		335.8	44.2	161.1
.8	A/9.5	1.00	4291.7	3029	243.6	29.2	106.9
.8	A/9.5	1.10	64.8		1.03	.031	.129
.8	A/9.5	1.20	.253		$.872 \times 10^{-3}$	$.006 \times 10^{-3}$	$.022 \times 10^{-3}$
.8	A/9.5	1.06	536.4		11.1	.72	3.3
.8	A/9.5	1.05	814.9	444.6	20.2		6.8
.8	A/9.5	1.03	1727	1053	60.4	5.56	23.6
EXPERIMENTAL			1600 ± 300	487 ± 109	139 ± 27	9.96 ± 2.55	8.04 ± 4.4

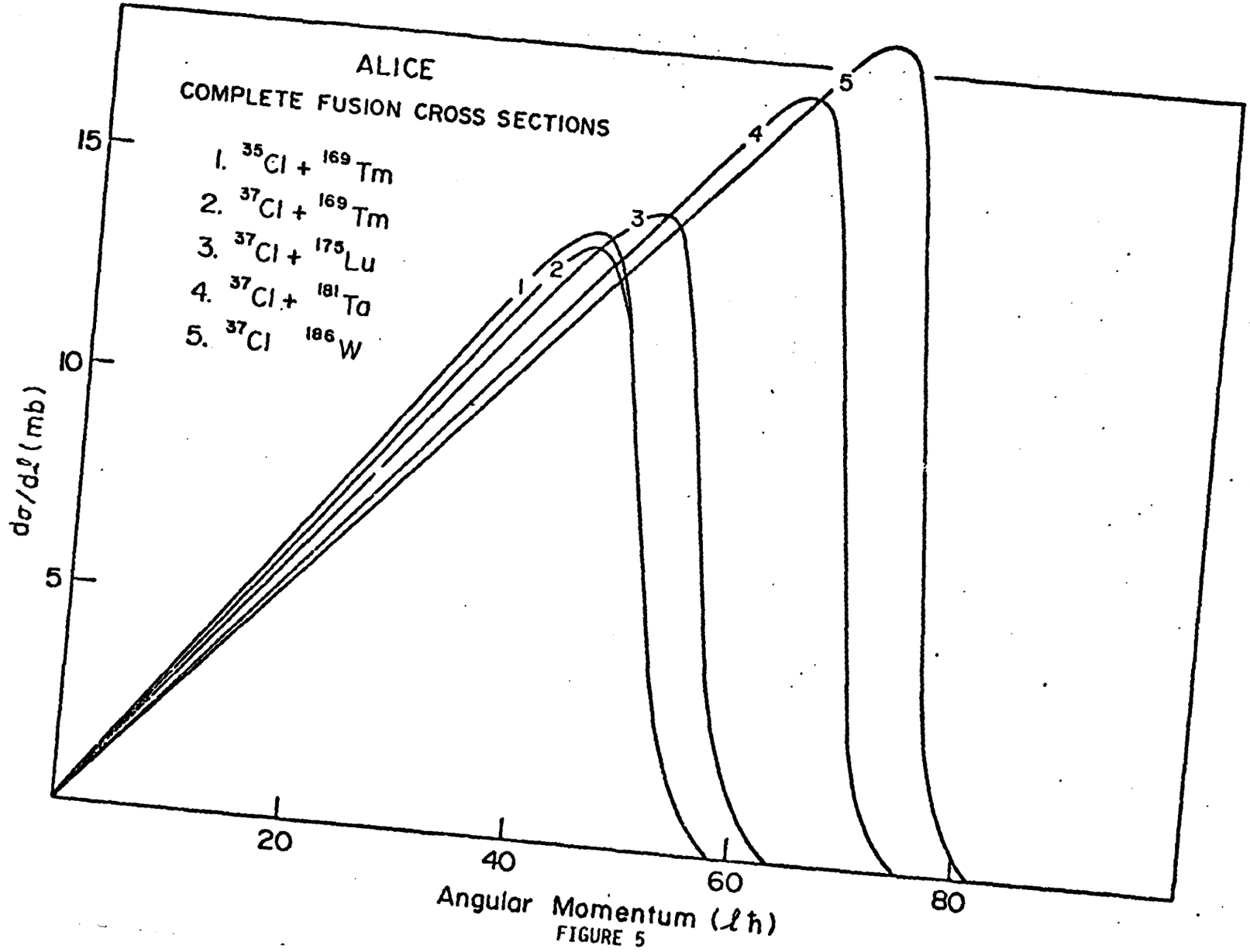
ALICE
COMPLETE FUSION CROSS SECTIONS
1. $^{35}Cl + ^{169}Tm$
2. $^{37}Cl + ^{169}Tm$
3. $^{37}Cl + ^{175}Lu$
4. $^{37}Cl + ^{181}Ta$
5. $^{37}Cl \; ^{186}W$
15
10
5
$d\sigma/d\ell$ (mb)
20
40
60
80
Angular Momentum ($\ell\hbar$)

FIGURE 5

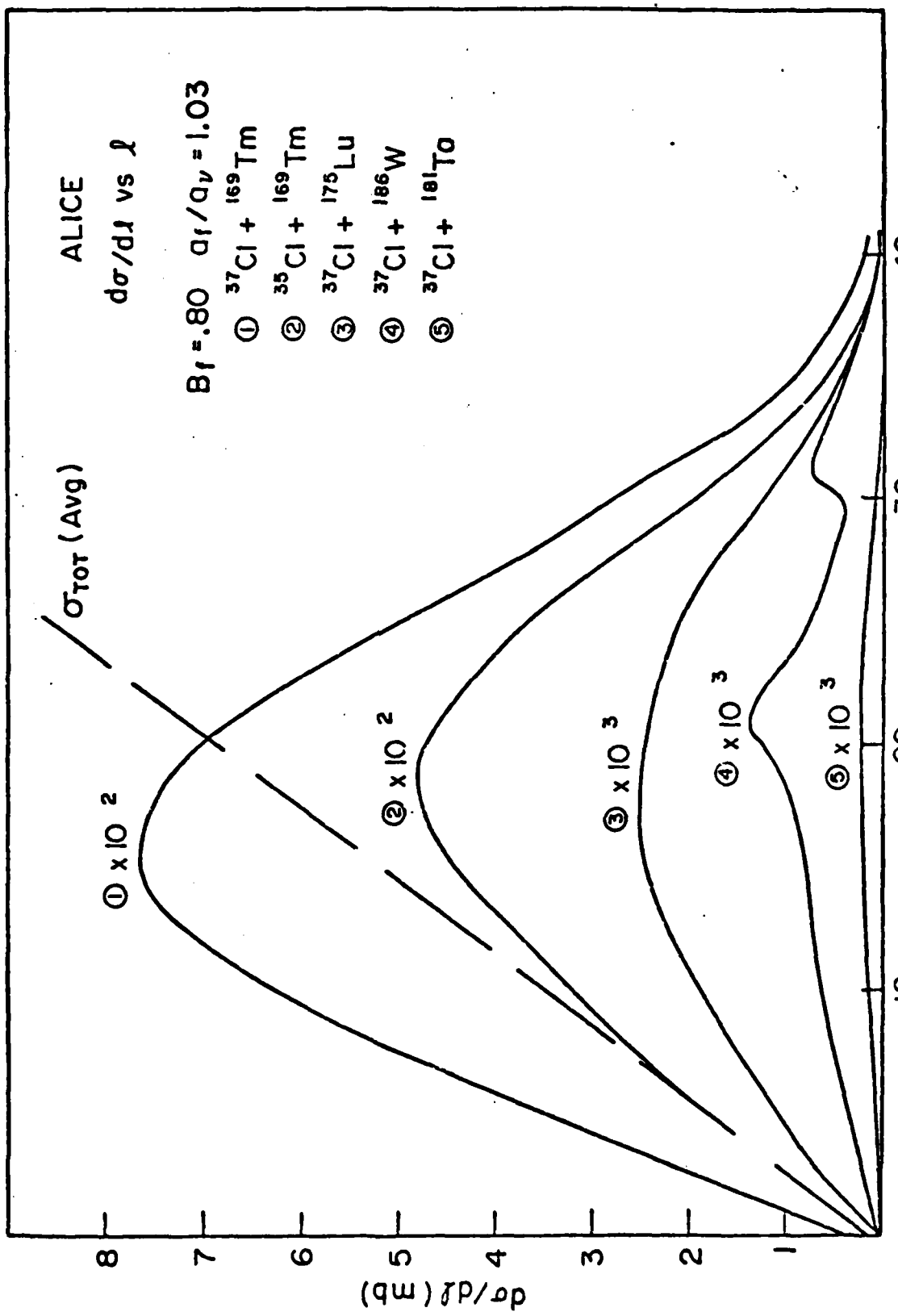
ALICE
dσ/dl vs l
Bf =.80 af/av = 1.03
① 37Cl + 169Tm
② 35Cl + 169Tm
③ 37Cl + 175Lu
④ 37Cl + 186W
⑤ 37Cl + 181To
σTOT (Avg)
① x 10 2
② x 10 2
③ x 10 3
④ x 10 3
⑤ x 10 3
dσ/dl (mb)
Angular Momentum (l ħ)
1
2
3
4
5
6
7
8
10
20
30
40

FIGURE 6

individual excitation functions for each evaporation channel. For this study the lower total evaporation residue cross section limit is given by parameter set B_f = 0.80, a_f/a_ν = 1.03, PLD = 9.5, will be utilized. This set was chosen as the closest set to the experimental data that, in the majority of the cases, was less than the experimental values. Many studies have shown ALICE to overestimate the evaporation residue cross sections and it is hoped that this study, with several low values, will help to show that ALICE can be an effective, and cost effective, tool in first estimations of heavy ion fusion reactions. Table VIII shows the calculated and measured evaporation residue cross section values for the parameter a_f/a_ν = 1.03. The table includes the lighter systems (A_{CN} = 98 to 172) presented by Beckerman and Blann[28] as well as the heavier systems from this work (A_{CN} = 204 -223). The values of a_f/a_ν = 1.03 continues to show promise in predicting total evaporation residue cross section. Note, however, that the fission barrier factors, B_f, increase with A_{CN}. This constancy of the ratio of single particle level densities of the fissioning nuclei to those of the residual nuclei as well as the linearity of the fission barrier factor may prove helpful in predicting the survivability of heavier systems.

Figure 6 shows the differential cross section versus angular momentum shows smooth functions for all reactions except the Tungsten reaction. This compound nucleus differs from the other four in that it posesses an odd unpaired proton. The Tungsten target is an

even-even nucleus (resulting in an odd-even compound nucleus) while all others considered were odd-even targets (resulting in even-even compound systems). This shell effect has been taken into account by the ALICE code. The total differential cross section for the Tungsten reaction is not smooth, but appears with two intermediate peaks. These are the result of a favored evaporation channel ($3n\alpha$) that is the major contributor to the total evaporation cross section and that peaks strongly in the same two areas. This may be the result of the particular deformation of the compound system, ^{223}Pa (odd-even), that favors alpha emission at specific angular momenta.

The assumption made by ALICE, that the emitting nucleus loses angular momentum at the rate of $1\hbar$ for neutrons $3\hbar$ for protons and $10\hbar$ for alphas, depends very much on the size of the compound nucleus. At high A this assumption becomes even less valid. The code MBIIZ handles the angular momentum loss much better by coupling the emitted particle angular momenta to that of the compound system. This shows up favorably in suppressing the multiple charge particle boiloffs that are seldom seen (i.e. 3pXn and 2αXn). The MBIIZ code is costly to run and should be used only as a refinement upon ALICE data.

D. Velocity and Angular Distributions Generated by the BETH Code

Since the velocity selector of the RMS passes a range of velocities rather than a single velocity, an experimental distribution

F(v), is a convolution of the true velocity profile, g(v), and the velocity dependent solid angle function, $\Omega(v-v')$.

$$F(v) = \int_{-\infty}^{\infty} g(v')\ \Omega(v-v')dv'$$

The BETH code (Bolton, 1978)[29] calculates the velocity distribution, g(v'), of the particular evaporation residues. Since the compound nucleus de-excites through neutron, proton and alpha emission (or a combination of these three), the evaporation residue (the large nucleus remaining) recoils in a distribution about the center-of-mass velocity, v_{cm}. Their direction, relative to the beam line, is also a distribution around $\theta = 0°$ rather than straight along it. The BETH program assumes that particle evaporation is sequential and isotropic. The assumption of an isotropic distribution of evaporation residues has been studied by Britt and Quintan[30] who found that the anisotropy of alpha evaporation is small. As an example he cites that the ratio of the observed anisotropy for 10.5 MeV/nucleon C + Au in the center-of-mass distribution is 1.20 ± 0.20. This is consistent with evaporation theory presented by Ericson to first order in $\cos^2\theta$

$$W(\theta) = 1 + (M_\alpha R^2/I)(E_{rot}/2T)\cos^2\theta$$

where R is the radius, I the moment of inertia, T the temperature and E_{rot} the rotational energy of the compound nucleus. Ericson's

formula gives $W(\theta)$ as approximately 1.3 to 1.4 (or 1.09 if the rigid body moment of inertia is used). The BETH assumption of isotropic emission, then, is sufficient to give a general overview of the angular distribution of alpha emission.

The following parameters were used by C. Bolton in the BETH program:

VELOCITY DISTRIBUTION IN CM FRAME

$$\frac{d^3\sigma}{dv^3}(\alpha,\beta,\varepsilon,\vec{v}) \propto \int \frac{d^3\sigma}{dv'^3}(\alpha',\beta',\varepsilon',\vec{v}')\,\frac{d^3\alpha}{dv^3}(\alpha'',\beta'',\varepsilon'',\vec{v}'')\,d^3v'$$

where $\alpha = \alpha' + \alpha''$ (alpha particles)

$\beta = \beta' + \beta''$ (protons)

$\varepsilon = \varepsilon' + \varepsilon''$ (neutrons)

$\alpha',\beta',\varepsilon',$ = 1 or 0

$\alpha'',\beta'',\varepsilon'',$ = 1 or 0

$\vec{V} + \vec{V}' = \vec{V}''$

INDIVIDUAL (α, p or n) VELOCITY DISTRIBUTIONS

$$\frac{d\sigma}{dV}(001) \propto Ee^{-\psi E}$$

$$\frac{d\sigma}{dV}(010) \propto \begin{cases} \sqrt{E}\,\sqrt{E-E_0}\,e^{-\phi(E-E_0)} & E > E_0 \\ 0 & E < E_0 \end{cases}$$

$$\frac{d\sigma}{dV}(100) \propto \begin{cases} -\Delta(E-E_{max})^2 + \Gamma & E < E_{max} \\ \sqrt{E}\ \sqrt{E-E_1}\ e^{-\gamma(E-E_1)} & E > E_{max} \end{cases}$$

where $E_0 = E_K - 5.2$

$E_K = .961\ Z/A^{1/3}$ $(r_0 = 1.5\ fm)$

$E_{max} = .206\ Z + 2.53$

$\psi = .9$

$\phi = .24$

$\gamma = 1/2(E_{max} - E.)$

$E_1 = E_{max} + (\ln\chi)^{-1}$

$$\chi = \frac{E_{max} - E_1}{2(E_{max} + 2 - E_1)}$$

Δ,Γ were determined by making the velocity distribution a continuous fit to experimental data.

The BETH program required a weighted set of evaporation cascades to generate the function $q(v')$. These were determined from the code ALICE. Once generated, each distribution is added (by weight) to yield a theoretical velocity profile that is then transformed to the lab system and convoluted with $\Omega(v - v')$ to yield a velocity distribution that can be compared to measured values. The transformation is the Jacobian:

$$|J| = \left| \frac{\partial \cos\theta_\ell}{\partial \cos\theta_{cm}} \frac{\partial V_\ell}{\partial V_{cm}} - \frac{\partial \cos\theta_\ell}{\partial V_{cm}} \frac{\partial V_\ell}{\partial \cos\theta_{cm}} \right| = \left(\frac{V_{cm}}{V_\ell} \right)^2$$

E. Charge Distribution

To determine apparatus settings (covered later), an average charge state $\bar{q}$ was needed. A starting point for determining the distribution was to use the formulae of Betz, et al.[31] and Nikolaev and Dimitriev[32]

BETZ	NIKOLAEV
$\frac{\bar{q}}{Z} = 1 - C \exp \frac{-V}{V_0 Z^b}$	$\frac{\bar{q}}{Z} = [1 + (Z^{-a} v/v')^{1/k}]^{-k}$
$c = 1.03$	$a = .45$
$b = .513$	$k = .60$
$V_0 = 2.188 \times 10^8$ cm/sec	$v' = 3.6 \times 10^8$ cm/sec

The width of the charge state distribution was determined as:

BETZ	NIKOLAEV
$d = d_2 \bar{q} \left[1 - \left(\frac{\bar{q}}{Z} \right)^{1/k} \right]^{1/2}$	$d = d_1 Z^w$
$d_2 = .5$	$d_1 = .25$
$k = .6$	$w = .5$

The charge state determined through the BETZ formula was always found to be too low by three to fine charge states. This is consistent with the BETZ experimental data that was used to generate the formula. These also compare with the RAYTRACE acceptance function shown in figure 12, where the percent change in charge state is plotted versus several velocities.

F. Stability of Nuclei as a Function of a Critical Value of Z^2/A

Fission may be viewed as a study of nuclear shape deformations taken to an extreme limit, resulting in separation into two or more fragments. Only binary fission will be discussed here. Adiabaticity, that the velocity of the collective motion, here the fragment of separation, is much slower than the individual motion of the nucleons, is also assumed. The use of the liquid drop model offers a first approximation of the observed features of fission since the microscopic motions of the nucleons are not accounted for.[33]

The surface of the nuclear drop can be described by:

$$R(\theta) = R\left[1 + \sum_{n=2}^{N} \alpha_n P_n \cos \theta\right]$$

where $R = r_o A^{1/3}$ fm

The coefficients α_n are generalized deformation coordinates

constrained by the conditions of nuclear incompressibility and the constancy of the center-of-mass coordinate (origin)

(Incompressibility)

$$\int_0^{\pi} \pi R^2(\theta)\left(-\frac{dR(\theta)}{d\theta}\cos\theta + R\sin\theta\right)\sin^2\theta d\theta = \frac{4}{3}\pi R_o^3 = 7.25\ A^{1/3}\ fm^3$$

(Constancy of cm)

$$\int_0^{\pi} R^3(\theta)\left(-\frac{dR(\theta)}{d\theta}\cos\theta + R\sin\theta\right)\cos\theta\sin^2\theta d\theta = 0$$

The surface energy is proportional to the surface area for a spherical drop:

$$E_S(\theta) \doteq 4\pi R_o^2 S$$

where S is the surface tension

$$E_S(\alpha_2,\alpha_3,\ldots) = 4\pi S\int_0^{\pi} R^2(\theta)\left(1 + \frac{1}{R(\theta)}\frac{dR(\theta)}{d\theta}\right)^{1/2}\sin\theta d\theta^*$$

if the deformation parameters are small

$$E_S(\alpha_2,\alpha_3,\ldots) = 4\pi R_o^2 S\left(1 + \frac{2}{5}\alpha_2^2 + \frac{5}{7}\alpha_3^2 + \ldots\right)$$

---

*The incompressibility and constance of center of mass equations require α_0 and $\alpha_1 = 0$.

The coulomb energy of a charge distribution of density $\rho(r)$ is

$$E_c = \tfrac{1}{2} \int \frac{\rho(\vec{r})\rho(\vec{r}')}{|\vec{r} - \vec{r}'|} \, d\vec{r} d\vec{r}'$$

with a uniform charge and constant volume the charge density (also constant) becomes

$$\rho = Ze/\tfrac{4}{3} \pi R_o^3 = .414 \; Ze/A$$

and

$$E_c(0) = \tfrac{3}{5} (Ze)^2/1.2 \; A^{1/3}$$

For small distortions the coulomb potential then becomes:

$$E_c(\alpha_2, \alpha_3, \ldots) = \frac{3}{5} \frac{(Ze)^2}{1.2 \; A^{1/3}} \left(1 - \frac{1}{5} \alpha_2^2 - \frac{10}{49} \alpha_3^2 + \ldots\right)$$

The deformation energy is the combination of the coulomb and surface terms.

$$\Delta E = \left(\frac{2}{5} \alpha_2^2 + \frac{5}{7} \alpha_3^2 + \ldots\right) E_S(0) + \left(-\frac{1}{5} \alpha_2^2 - \frac{10}{49} \alpha_3^2 + \ldots\right) E_c(0)$$

By restricting the potential only to quadrupole deformations we

find

$$\Delta E = \frac{2}{5} \alpha_2^2 E_s(0)(1 - \chi)$$

where χ is the fissility parameter

$$\chi = \frac{Z^2}{A} \frac{3e^2}{40 \pi (1.2)^3 S}$$

For $\chi < 1$ the drop is stable and $\chi > 1$ unstable against spontaneous fission.

$$\left(\frac{Z^2}{A}\right)_{CRIT} = \frac{40 \pi (1.2)^3 S}{3e^2} \simeq 40\text{-}50$$

A critical value of Z^2/A becomes the dominant factor in the stability of heavy nuclei. As seen in figure 7 above a value of $Z^2/A = 40$, the spontaneous fission half life is very low. There, the probability of fission versus other decay modes becomes very high. In heavy ion fusion reactions in the regime presented in this work, from $Z^2/A = 35.9$ to 37.2, the nucleus must contend with its own natural desire to fission as well as the high excitation energy imparted by the fusion reaction itself, all of which greatly increases the instability of the compound system. This results in a high incidence of fission, occurring at all angular momentum values as shown by ALICE (see figure 6), with very little remaining to be

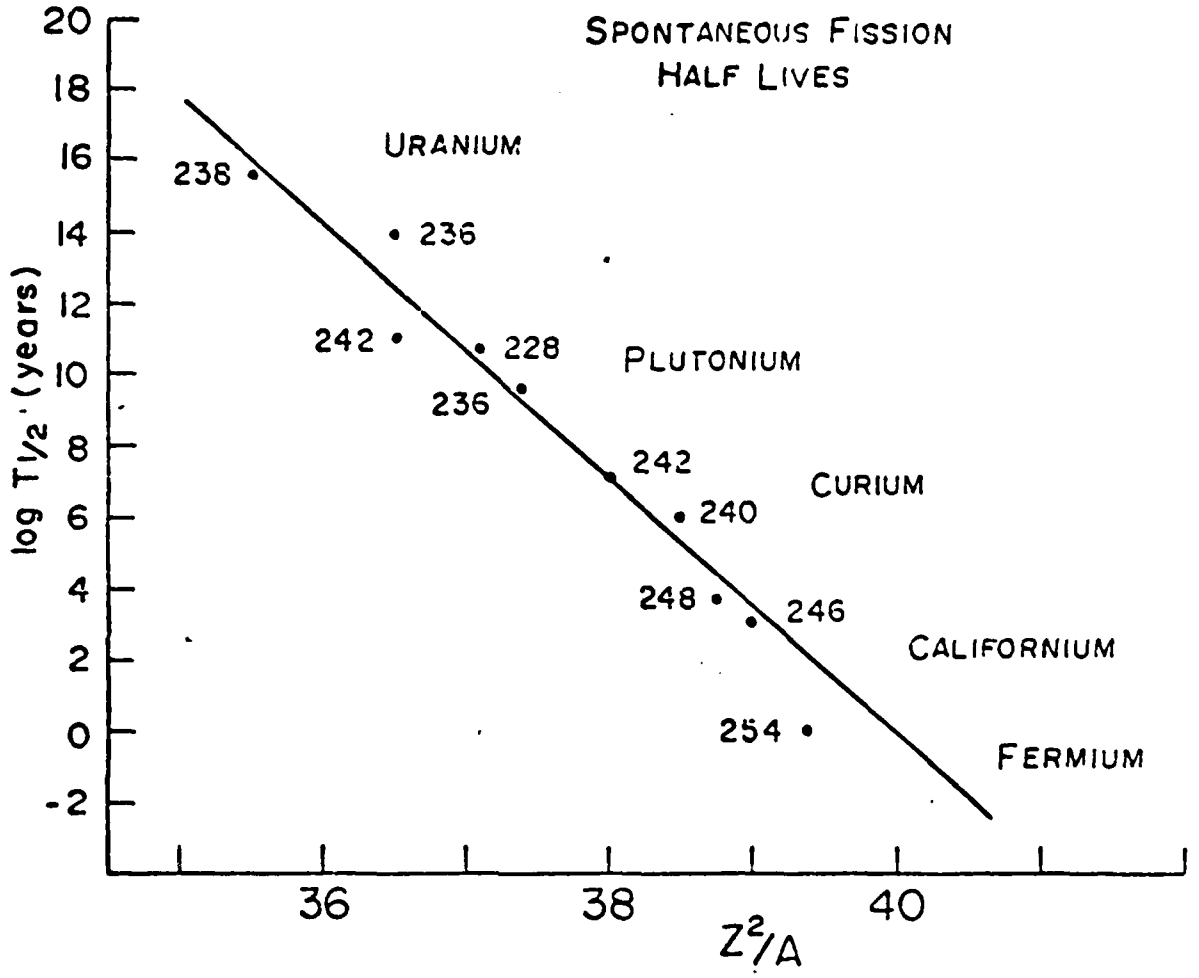
SPONTANEOUS FISSION
HALF LIVES
URANIUM
PLUTONIUM
CURIUM
CALIFORNIUM
FERMIUM
238
236
242
228
236
242
240
248
246
254
log T1/2 (years)
20
18
16
14
12
10
8
6
4
2
0
-2
36
38
40
Z²/A

FIGURE 7

de-excited by particle emission. This is the point of departure of this work; to quantify the stability of the compound systems as Z^2/A increases toward a critical point. While that critical point is not reached, the trend of instability is quantified.

CHAPTER III

EXPERIMENTAL APPARATUS

A. The Recoil Mass Selector

The purpose of the RMS is to separate fusion products from the projectile ion beam. The beam is collimated and centered onto a thin foil target, where fusion occurs. The majority of the beam is scattered. This scattering, along with the fusion products if forward peaked in the beam direction, however the fusion products have significantly less velocity and are deflected more than the faster moving beam by a series of electric and magnetic fields. These fusion products (plus a small portion of the beam slowed by scattering) are then focused onto a solid state detector through a series of quadrupole magnets. This apparatus is well suited for detection of the evaporation residues of the fusion products which exhibit a small angular distribution and a low yield. Here, zero degree separation is a necessity and is accomplished by the removal of the evaporation residues from the line of the projectile beam.

The beam is obtained from the BNL MP-7 Tandem Van de Graaff Generator with a maximum terminal voltage of about 14 MeV. The beam is directed, focused and shaped magnetically as it enters the target room. A collimator consisting of two aperture sets separated by a 20 inch pipe is the first portion of the RMS encountered. The

apertures are mounted on a base that allows the selection of a variety of sizes. For this series of experiments a 0.375 inch diameter was selected. The apertures are lined with gold foil to minimize any undesirable reaction products that may result from the beam striking the aperture edge. Electrical connections are made to monitor as current any beam particles impinging on the collimator.

The collimated beam enters the target chamber (see Figure 8) which consists of a round drum with an exit port cut through a sliding tape, a rectangular slit, a target ladder, and two 25 mm^2 solid state detectors (as monitors of Rutherford scattering for normalization purposes). The rectangular slit consists of four independently adjustable spectroscopy grade carbon rods. Current is monitored from each rod and optimal beam collimation occurs when these currents are at a minimum. Slit dimensions were 0.055 in. vertical and 0.150 in. horizontal during these experiments. The target chamber has several view ports to inspect the interior of the target chamber while under vacuum. The target ladder is mounted one inch behind this final collimator and is capable of supporting four target frames. This affords the ability to change targets without interrupting the vacuum.

Two 25 mm^2 solid state detectors are mounted at angles of 28.8° and distances of 23.28 cm from the beam spot on the target ladder. This results in a solid angle of acceptance for the two monitor detectors of 0.07317 msr (monitor aperture is 1/16 in.).

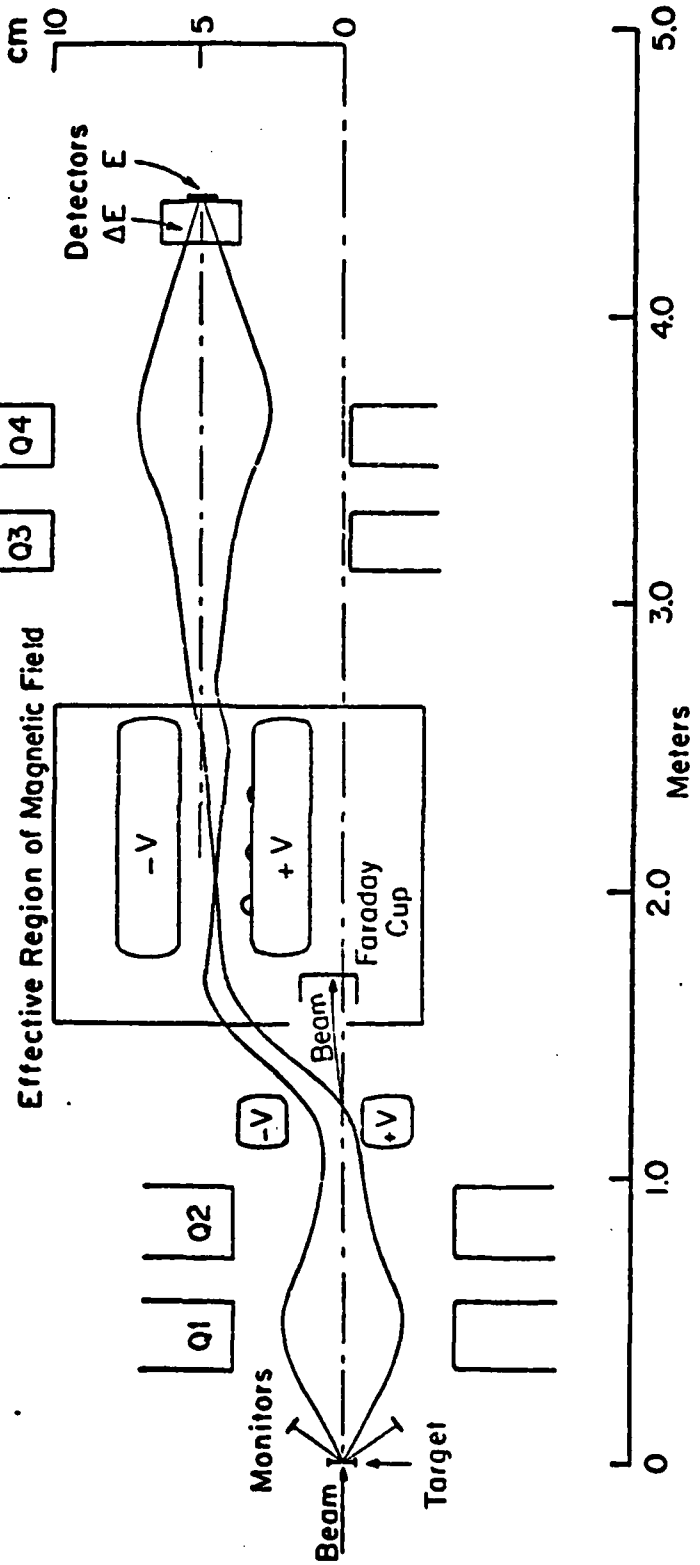
cm
10
5
0
Detectors
E
ΔE
Q4
Q3
Effective Region of Magnetic Field
-V
+V
Faraday Cup
Beam
-V
+V
Q2
Q1
Monitors
Beam
Target
0
1.0
2.0
3.0
4.0
5.0
Meters

FIGURE 8

The exit port of the target chamber (0.5 in. diameter) is mounted on a sliding steel tape pressed against a neoprene gasket that is sealed to preserve the vacuum. This equates to a 7.5 msr solid angle at the target chamber exit. The entire recoil mass selector apparatus, over four meters long, connects to this two inch wide tape and 1/2 inch hole and can rotate about the target spot. This enables the RMS to be utilized for a variety of experiments requiring observations at other than zero degree.

The fusion products and beam exiting the target chamber first encounter a magnetic quadrupole pair at 26 cm from target (the 15/16 in. aperture* here equates to 4.2 msr). This pair of quadrupoles is designed to focus the exiting particles into the velocity selector in order to increase the acceptance solid angle.

A charged particle with velocity $\vec{v}$ experiences a force $\vec{F}$ when moving in an electromagnetic according to the Lorentz equation:

$$\vec{F} = q(\vec{E} + \vec{v} \times \vec{B})$$

Thus a positively charged ion moving in the +z direction will experience a Lorentz force:

$$F_x = -\frac{VB_o x}{R} \qquad F_y = +\frac{VB_o y}{R}$$

*n.b. All aperture holes mentioned are tapered to afford easy solid angle calculations.

The sign of the force component is significant since it shows a focusing in the $\hat{x}$ direction and a defocusing in the $\hat{y}$ direction. Applying the thin lens approximation,* valid for $f_0 >> \ell$, the effective length, the focal length is then

$$\frac{1}{f_0} = \frac{B_0}{R}\frac{\ell}{B_p} \qquad f_x = f_0 = -f_y$$

For a quadrupole with hyperbolic pole pieces,

$$B_x = \frac{B_0}{R} y \qquad B_y = \frac{B_0}{R} x$$

where R is the aperture radius and B_0 is the field at the pole tip.

In order to focus a beam of charged particles, two quadrupoles are utilized. The first acts a converging lens in the $\hat{x}$ direction and a diverging lens in the $\hat{y}$ direction. The second acts in an opposite manner diverging $\hat{x}$ and converging $\hat{y}$ (see Figure 9).

The pole pieces used in the quadrupoles are 6 in. long with an aperture diameter of 3.0 in. The coils are water-cooled and each quad is protected by a McDonnell flow switch connected to the power supply. The power is supplied by two Hewlett Package 6269B power amplifiers. The purpose of the first pair of quadrupoles is to focus a larger cone of particles into the Wien filter than would be

---

*n.b. Thin lens approximation: that the length of the effective field is much less than mv_o/B_q.

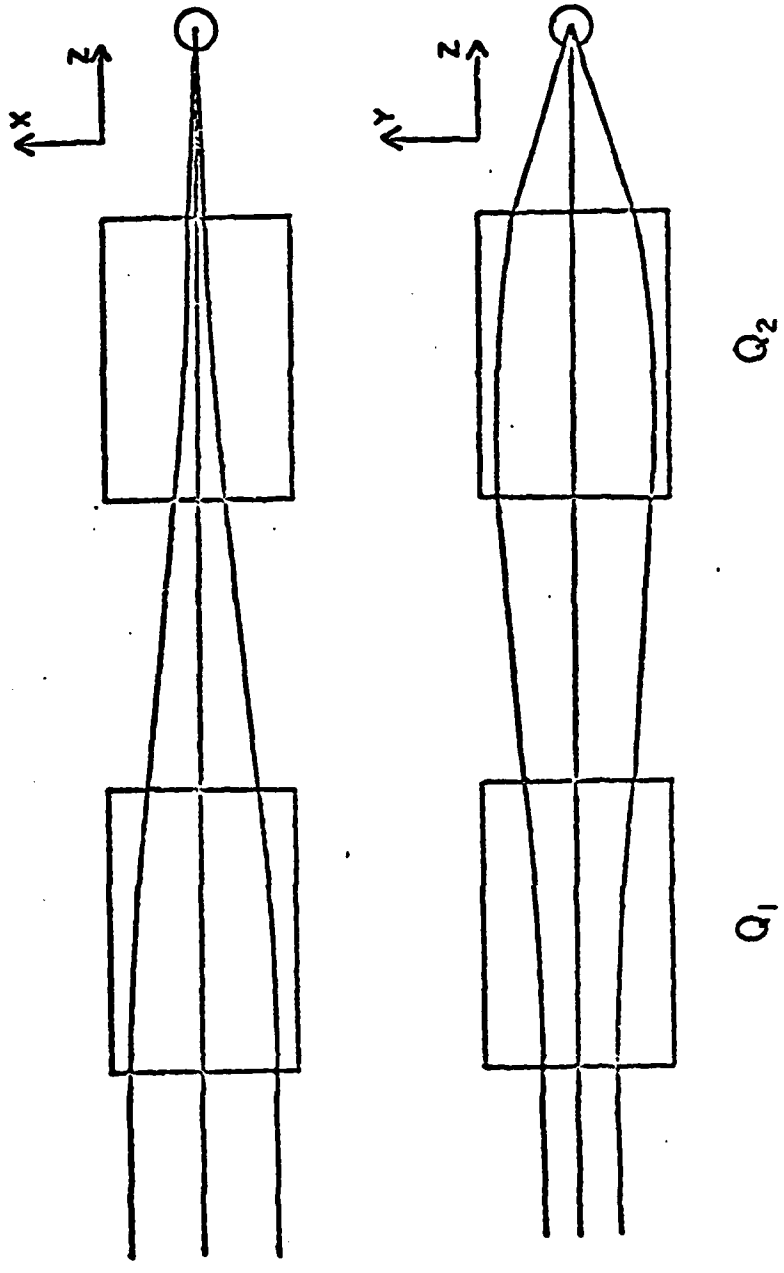

QUADRUPOLE PAIR FOCUSING

FIGURE 9

available geometrically over the distance to the target. The Wien Filter[34,35] analyzes the charged particles according to velocity. The fields are arranged perpendicular to and mutually along the path of the particle. The Lorentz force will vanish if its velocity is equal to the ratio of the Electric to the magnetic field strengths. (v_o = E/B). With no force acting on it, the particle will not be deflected. On the other hand, a particle with less velocity will be deflected up while the one of higher velocity deflected down. This will also hold true in the fringing fields where the strengths are no longer constant.

The fringing fields introduce complications, however. Upon encountering the velocity selector, the particle experiences a magnetic force which deflects it and then an electric force to straighten out the orbit. However, since the air gap is larger in the magnet than in the electrostatic deflector, the latter's fringing field is correspondingly narrower. While the electrostatic force straightens the orbit, it offsets the trajectory at the entrance and exit of the field. This offset is espressed by

$$\Delta x = IB_q \frac{D_m^2 - D_E^2}{mv_o}$$

where D_m and D_E are the magnetic and electric air gaps and I is the fringing field shape dependent integral,[36] (see Figure 10). In the present device I = 0.85, D_m = 10 cm, D_E = 2.54 cm and B_q/mv_o = 169 cm

VELOCITY SELECTOR

From Enge, Nucl. Inst. & Methods 145 (1977) 280

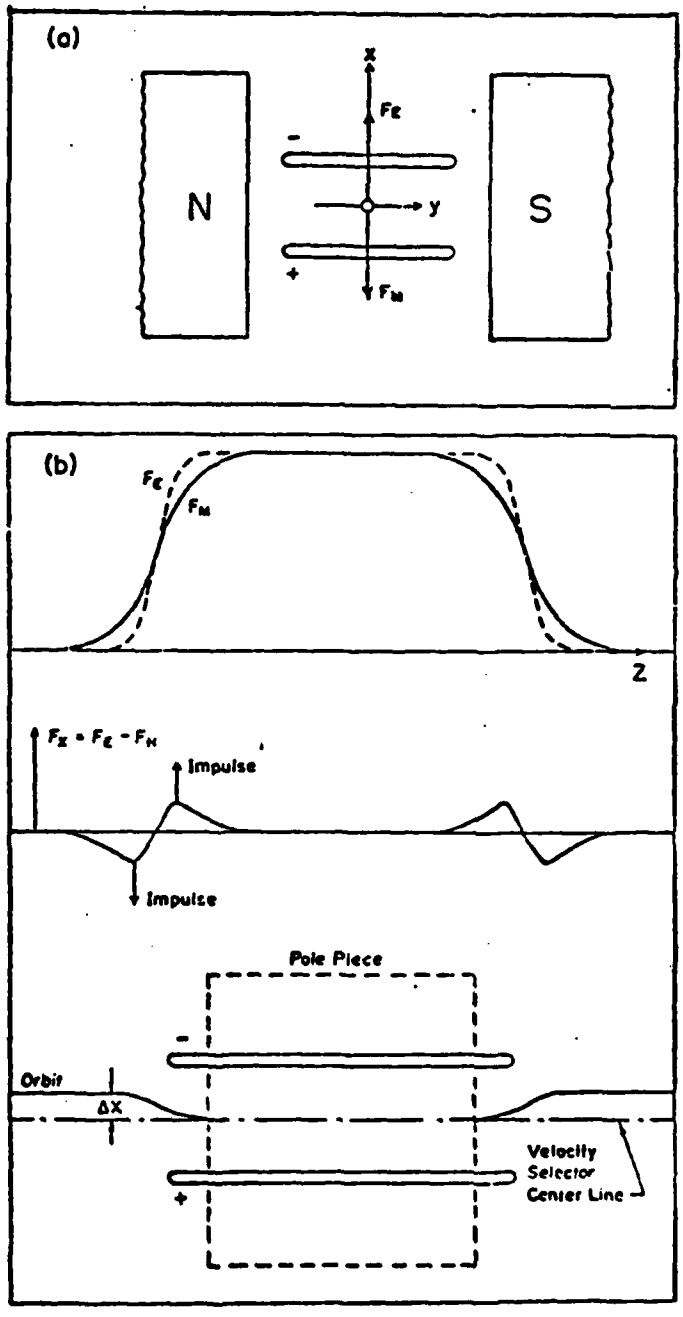

FIGURE 10

resulting in a vertical offset of 0.47 cm from the target spot.

There are two sets of plates in the velocity selector. First encountered by the beam is an electrostatic field which deflects the charged particles as a function of their charge to energy ratio

$$\Delta x_E \propto \frac{1}{p_\varepsilon} \propto \frac{1}{\frac{mv^2}{q}} \frac{1}{\varepsilon} \propto \frac{q}{E}$$

The particles are allowed to drift with the barely deflected beam particles impinging on a Faraday cup and the slower, more deflected evaporation residues entering the magnetic field. This pure magnetic field has the same effective field length and produces the same radius of curvature as the electrostatic field. The magnetic field bends particles downward (back parallel to but offset from, the beam line) according to the charge to momentum ratio,

$$\Delta x_B \propto \frac{1}{p_B} \propto \frac{1}{\frac{p}{q} \frac{1}{B}} \propto \frac{q}{p}$$

The third portion of the velocity selector is the $\vec{E} \times \vec{B}$ region which selects velocities such that $v_0 = E/B$ is undeflected.

The separation of pure $\vec{E}$ and $\vec{B}$ fields by the drift space results in a net upward displacement of 4.13 cm. As stated, the more energetic beam has been stopped by the Faraday cup. Those particles in the beam tail with velocity v_0 that allow it to pass through the filter have a much smaller mass and are deflected into

an adjustable upper baffle. A smaller velocity bite will result with higher fields. Figure 11 shows the acceptance solid angle versus the percentage of velocity deviation from v_0 for ρ = 169 cm as determined by RAYTRACE.

The electrostatic plates are supplied by Spellman HVE Corporation model RHR 69P30/RVL and RHR 60N30/RVL (± 60 KV). The voltage difference is remotely monitored using a digital voltmeter. The magnetic fields are supplied by an Alpha (Donner Systron) 440 volt supply. A digital Hall effect gaussmeter enables remote readings of the fields.

Upon leaving the velocity selector at 4.17 cm above the beam line, the evaporation residues are focused onto an E-ΔE telescope by means of another pair of quadrupoles. The pole pieces in these quadrupoles are 8 in. long and the aperture diameter is 4.125 in. These are also water cooled and flow switch protected. The ratio of their field strengths is 1.063 (downstream to upstream) using resistors in a current dividing circuit. The fields are monitored by two digital voltmeters.

The Recoil Mass Selector, to recapitulate, consists of a beam collimator, a thin target, a quadrupole pair to focus particles into the E field of the velocity selector, the B field and $\vec{E} \times \vec{B}$ region of the velocity selector followed by another quadrupole pair that focuses the separated particles onto the E-ΔE detector. The program RAYTRACE is designed to show the path of a specific ray of

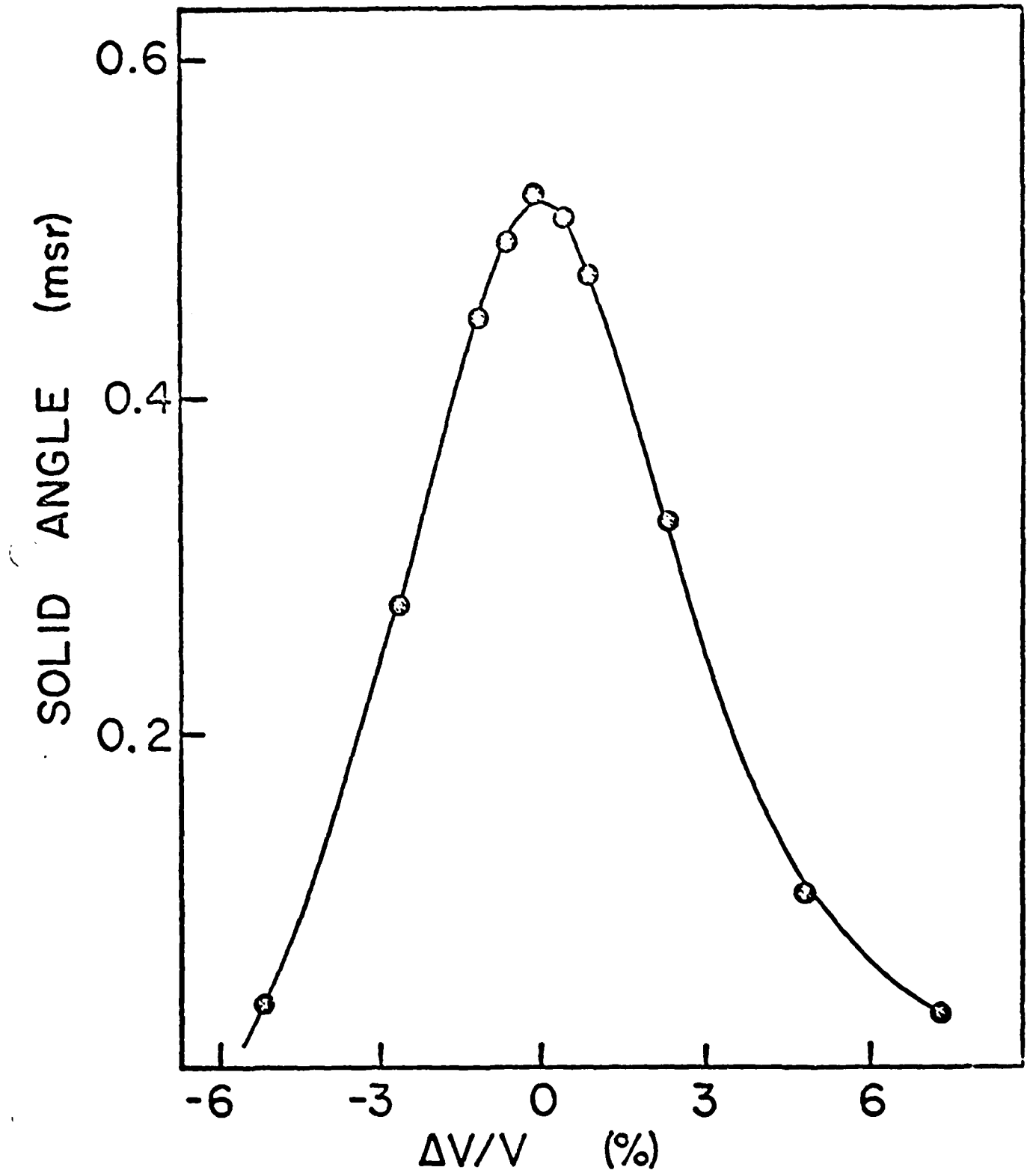

FIGURE 11

charged particles with specific charge and energy that is emitted at a specific angle from the target. RAYTRACE takes into account the abnormalities of the fringing field areas and can be tailored to any configuration of multipole magnets. The program, then, will give a velocity bite and a charge bite that is acceptable to a specific configuration of multipoles and electromagnetic fields. Figure 12 shows a contour plot $\Delta q/q$ vs. $\Delta v/v$ for a 230 amu particle with mean charge state $\bar{q}$ = 17 and energy $\bar{E}$ = 27 MeV. Contour lines are plotted from 10% to 90% acceptance for a ±50 mr ray passing through the system and reaching the detector. The 50% acceptance is shown to be $\bar{q}$ - 18% to $\bar{q}$ + 9% and $\bar{v}$ - 5% to $\bar{v}$ + 3.5%. Figure 13 shows plots of several ±50 mr rays of a 27 MeV particle to show the action of various charge states and velocities in the RMS.

To determine the evaporation residue cross section, an angular distribution was obtained from 0° to 6° and a velocity profile measured at each step. The velocity distribution is measured by varying the ratio of the electric to magnetic field. All of the fields are varied in a predetermined fashioned assuming constant mass but a mean charge state that varies with velocity. Included into the velocity distribution is the velocity acceptance function of the instrument.

For momenta and charge states other than the mean charge and momentum, the effective solid angle of acceptance of the RMS rapidly diminishes because of chromatic focusing errors (see

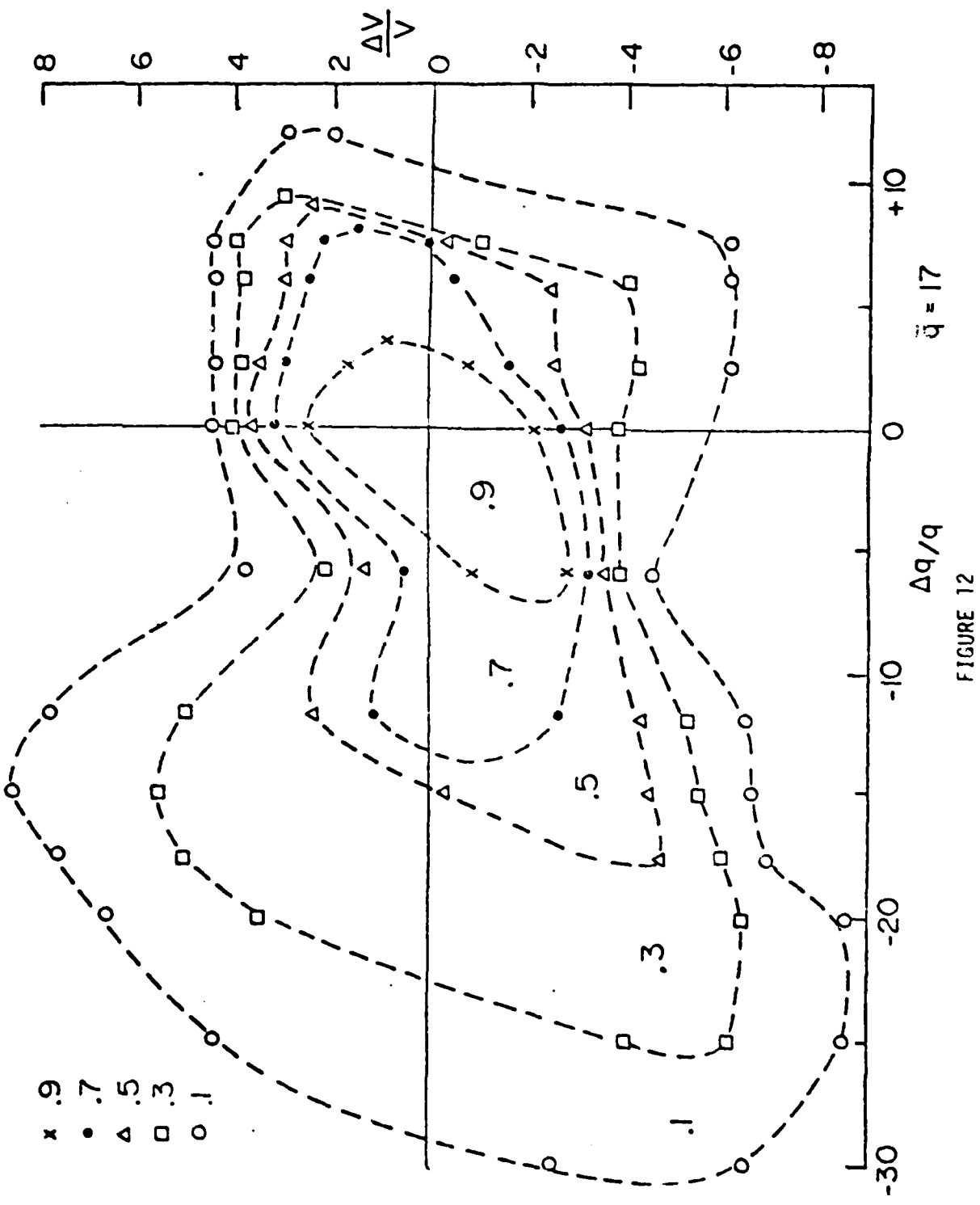

FIGURE 12

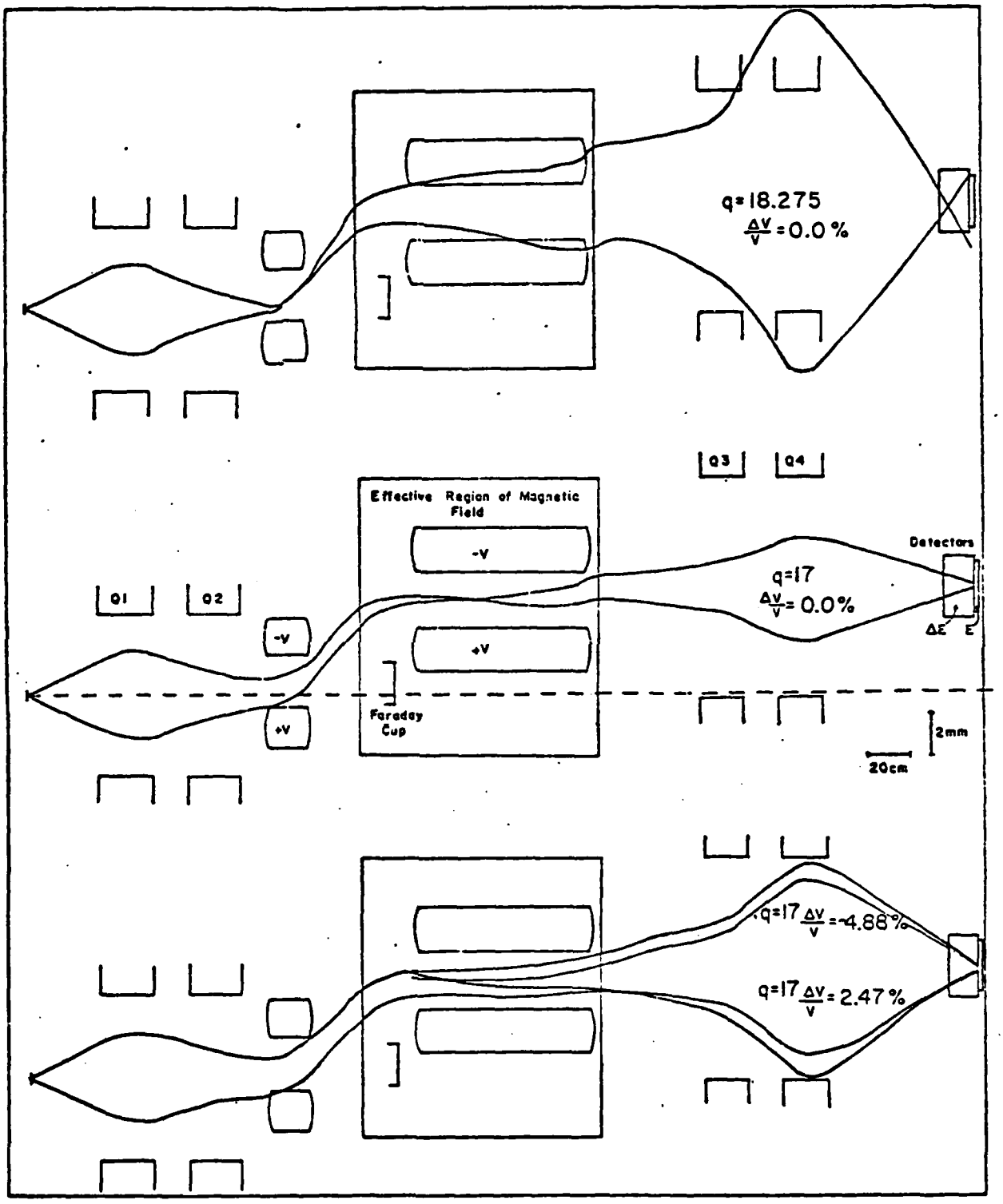
q=18.275
ΔV/V=0.0%
Q3
Q4
Effective Region of Magnetic Field
-V
+V
Detectors
q=17
ΔV/V=0.0%
ΔE
E
Q1
Q2
-V
+V
Faraday Cup
2mm
20cm
q=17 ΔV/V=-4.88%
q=17 ΔV/V=2.47%

FIGURE 13

Figure 11). The effective solid angle was determined by elastically scattering a 33 MeV gold beam from a thin gold target and setting the RMS at an angle equal to the monitor detectors (28.8°). The ratio of counting rates then directly gives the effective solid angle of the device relative to the solid angle of the monitors. The elastically scattered gold particles have a sharp velocity spectrum but the charge state distribution is similar to that of the evaporation residues. Each point of the velocity profile represents the solid angle integrated over the charge state distribution.

B. The Detector

The fusion products embed themselves in a solid state detector and decay there primarily by alpha emission. If the alpha particles are stopped in the depletion layer they give rise to full energy peaks. The range of the alpha particle is, on the average, 5.6 times greater than that of the heavier evaporation residue, and, as such, 43 percent of the backward emitted alphas escape through the surface of the detector. These escaped alphas are registered as background events with the majority of the energies far below the lowest energy alpha peak. Therefore a correction of 1/.57 was applied to cross section calculations.

The beam rejection capability of the RMS has been tested at 1 part in 10^{15} particles rejected at energies above 30 MeV. In the 6-30 MeV range a few background events, possibly due to beam

particles, were recorded.[37] Low energy scattered beam particles (approximately 200 sec^{-1}) with a velocity comparable to that of the fusion products (energy equal to 5 MeV), however, do pass through the system.

Since the low energy beam tail interferes with the low energy portion of the alpha spectrum, a ΔE gas ionization chamber is placed in front of the E detector. The ΔE detector is used to create an anticoincidence signal that eliminates the background since only an E signal resulting from a decay within the detector rather than an E signal due to an entering particle is desired. Figure 14 shows two spectra, the top without and the bottom with, the use of the ΔE chamber in anticoincidence with the E counter.

The ΔE-E detector[38] is a machined aluminum gas chamber with a detector holder. The surface barrier detector is held in place by a rear mounted Microdot connector. The front face of the detector serves as the rear cathode of the proportional counter whose anode wire is mounted just outside the active volume. The 10 micron nichrome wire is glued to the contact posts under 5.2g tension and the glue points painted with a silver conductor to insure proper contact. The window consists of 60-100 $\mu g/cm^2$ polypropylene on a removable frame that fits onto a special cover plate for the counter (see Figure 15). The Markham counter, here used only to generate a ΔE pulse, can also be utilized as a two dimensional position sensitive detector as outlined in the referenced article.

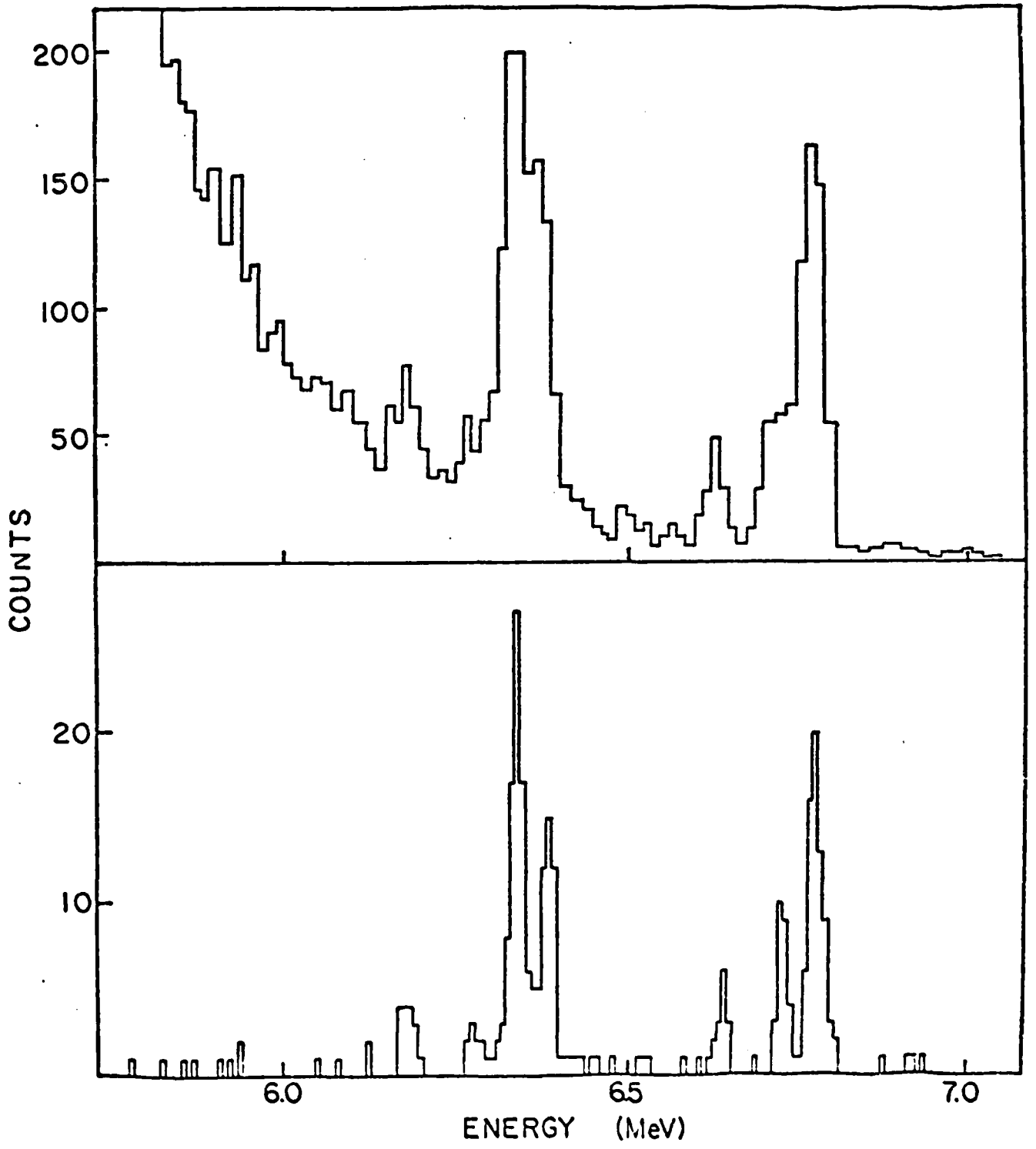

FIGURE 14

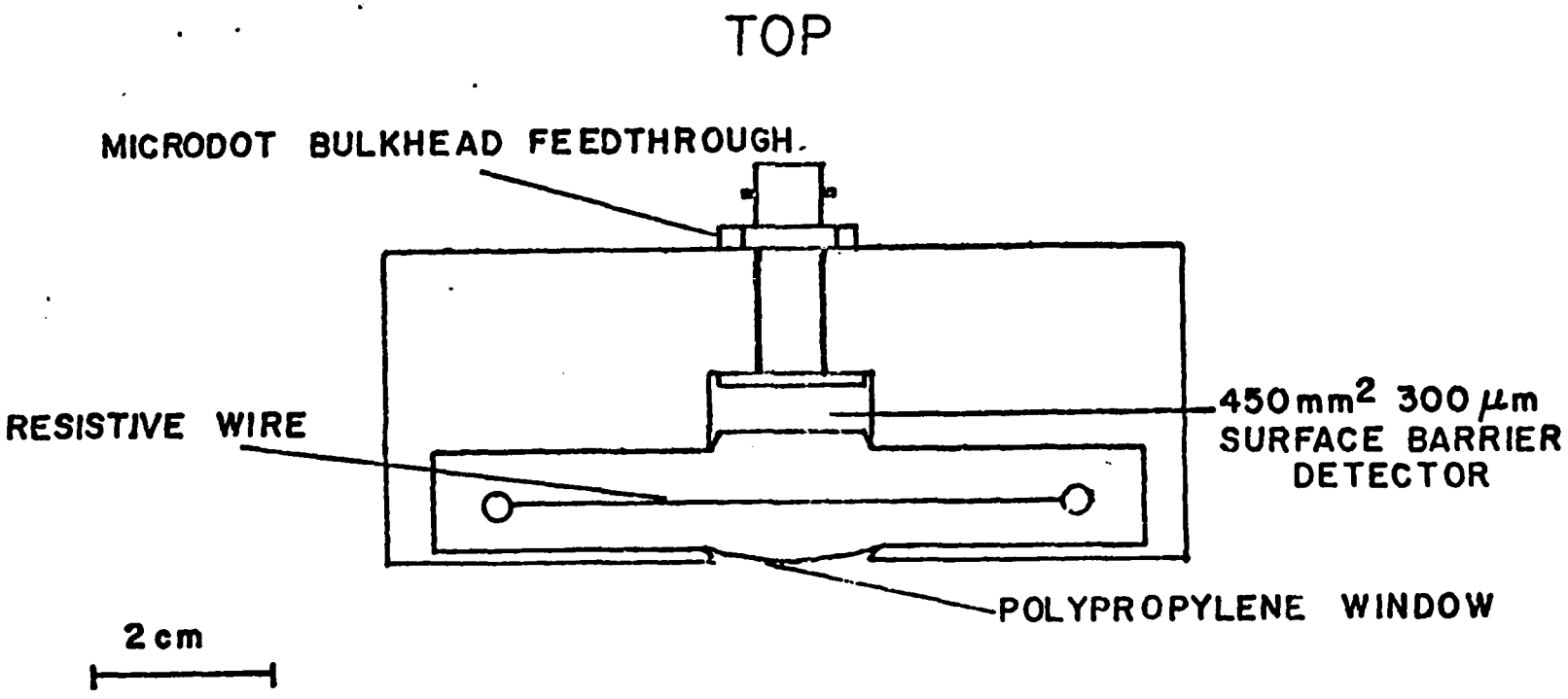

E-ΔE COUNTER

FIGURE 15

The E detector was calibrated by an Americium-241 alpha source. Energy shifts due to dead layers on the detector and source surface were studied by orienting each separately at 60° to the normal of the other. This produced a 30 keV shift in the peak energy. The system electronics were tested for linearity with a pulser to determine slope and zero point energy. Since the alpha decay occurs in the depletion layer, the recoil of the heavy nucleus that decays also contributes to the pulse height. Approximately 12% of the recoil energy (~130 keV) is registered however.

C. The Electronics

The input into the BNL Σ7 computer consists of the ΔE-E system and a timing system. Figure 16 shows the ΔE-E system. An "E" signal and an "All" signal are displayed as well as the anticoincidenced alpha gate in order to be able to see an overview of the total spectrum as well as to see where the alpha spectrum falls between the beam tail and the knockouts. The delay amplifier on the E signal is used to adjust the relative timing between the E pulse and the gate pulse. The Gate and Delay Generator (GDG) along the ΔE signal is used to broaden the square peak put out by the Timing Single Channel Analyzer (TSCA) to 4.5 μsec, so that any system fluctuations are not allowed to disrupt a coincident signal. The final GDG reduces the pulse, after passing through the universal coincidence box, to 0.5 μs.

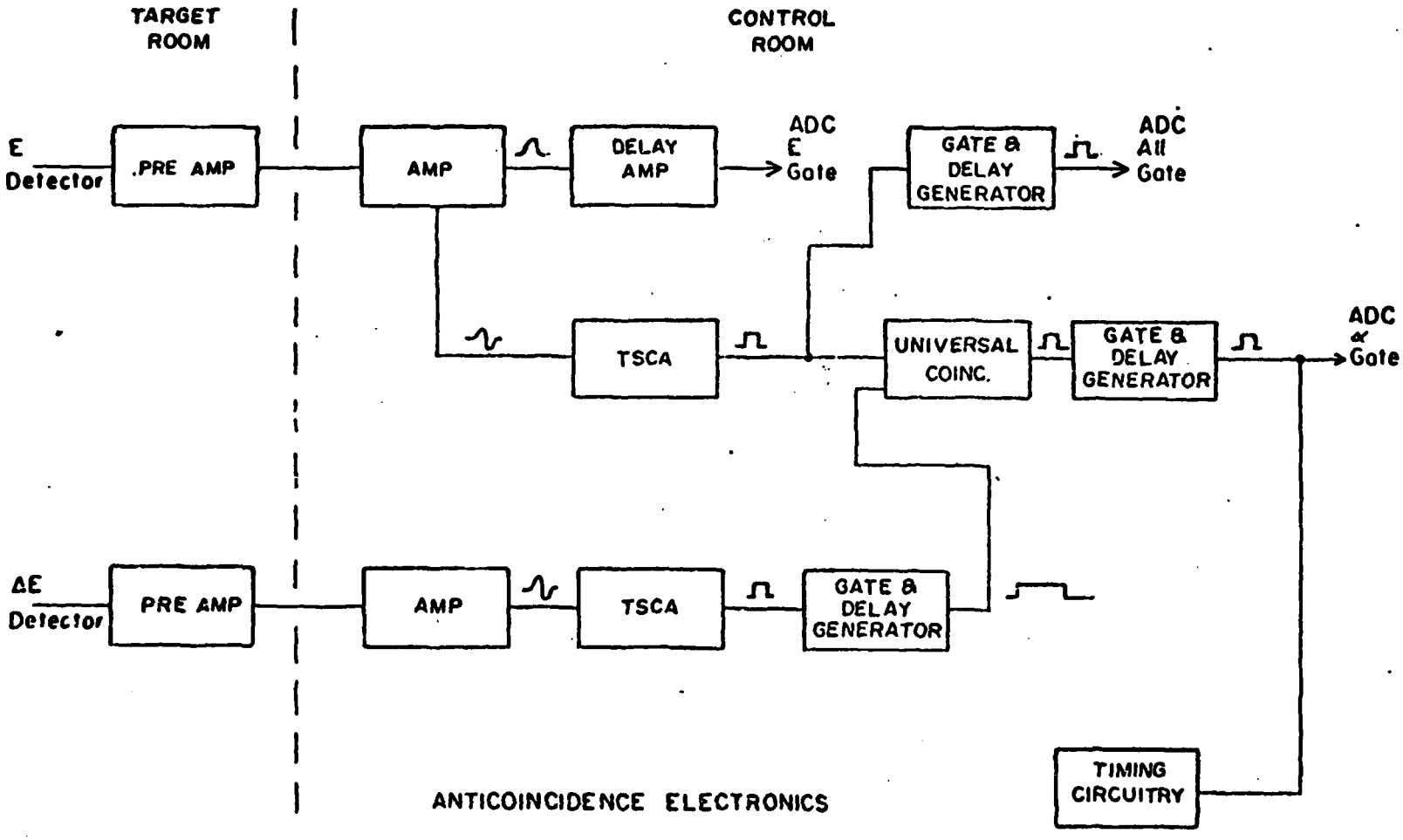
TARGET ROOM
CONTROL ROOM
E Detector
.PRE AMP
AMP
DELAY AMP
ADC E Gate
GATE & DELAY GENERATOR
ADC All Gate
TSCA
UNIVERSAL COINC.
GATE & DELAY GENERATOR
ADC ∝ Gate
ΔE Detector
PRE AMP
AMP
TSCA
GATE & DELAY GENERATOR
TIMING CIRCUITRY
ANTICOINCIDENCE ELECTRONICS

FIGURE 16

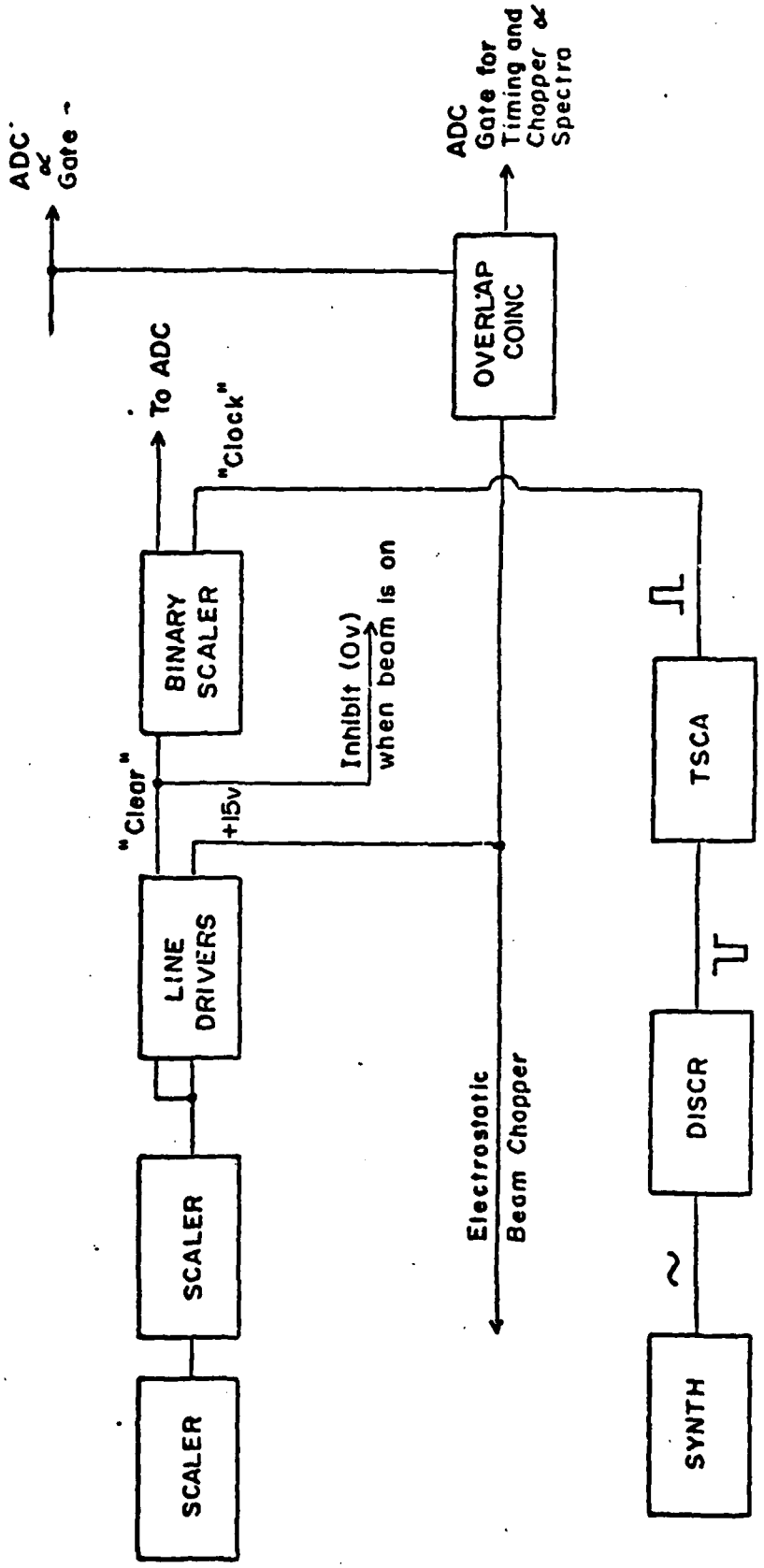

FIGURE 17

TIMING ELECTRONICS

The other portion of the electronics is the timing mechanism (Fig. 17). Here, the evaporation residue pulse was used to simultaneously start a multiscalar and trigger an electrostatic deflector that cut off the beam. Data is recorded in a 2-D time vs. energy mode. The beam is held off for a duration equal to several half lives of the parent nuclei. The 2-D timing spectrum can be gated to up to 16 separate energy peaks by the Σ-7 computer. This allows for the simultaneous timing of 16 separate alpha spectra which are very useful in determining the decaying nuclide when similar alpha energies are present. An accurate half life is also necessary in determining isomerism.

CHAPTER IV

EXPERIMENTAL RESULTS

A. $^{37}Cl + ^{169}Tm$

This experiment, utilizing the very plentiful ^{37}Cl beam (at the BNL Tandem), is included in this work as a point of departure. The author joined the research group after much of the experimental work had been accomplished and participated only in obtaining velocity distributions and lifetime data and performing the various ALICE calculations. It is included in this work since all system improvements were made after the primary data was obtained and because all calculations in this work (to obtain absolute cross sections) are based on method conceived for the Thulium experiment. The soon to be published paper[39] detailing this experiment contains both the results and the methodology of the experiment and will only be partially reproduced here.

To determine an absolute cross section for the production of a compound nucleus that survives fission, an integration must be accomplished over both an angular and a velocity distribution. It was shown in figure 11 that the total velocity accpetance of the RMS ran from +6% to -6% of the expected velocity. This was obtained by the elastic scattering of a gold beam matched in energy to the fusion products at an angle equal to that of the 50 mm^2 monitor

detectors used for normalization. This established an effective solid angle of acceptance of the RMS. It was also necessary to determine the average detector to monitor counts. This was accomplished by superimposing figure 11 over the several intervals of the velocity profiles and obtaining an average value. This is shown in figure 18 for a 3 point velocity profile. The integration is then accomplished by approximating the integral

$$\sigma = 2\pi \int \frac{d\sigma}{d\Omega} \sin\theta d\theta = 2\pi\Delta\theta \sum_{\theta=0°}^{8°} f(\theta) \sin\theta$$

where f is the scaling factor obtained from the normalized count to the solid angle of acceptance ratio and $\Delta\theta = 2°$.

In the conduct of an experiment to study the various evaporation residues of a particular compound system, a separate velocity spectrum is needed for each particular species of evaporation. It is impractical, however, in a study of several reactions, each at several lab energies, to obtain a detailed velocity and angular distribution at every energy. In the conduct of these experiments, one velocity distribution and one angular distribution was obtained for each evaporation residue at a lab energy near the peak in the total cross section. For the $^{37}Cl + ^{169}Tm$ reaction a detailed velocity profile of 12 points was taken ranging from -14.7% to +20.7% of v_o. In all other reactions a modified 3 point velocity profile of +10%, 0, -10% of v_o was taken. All angular distributions

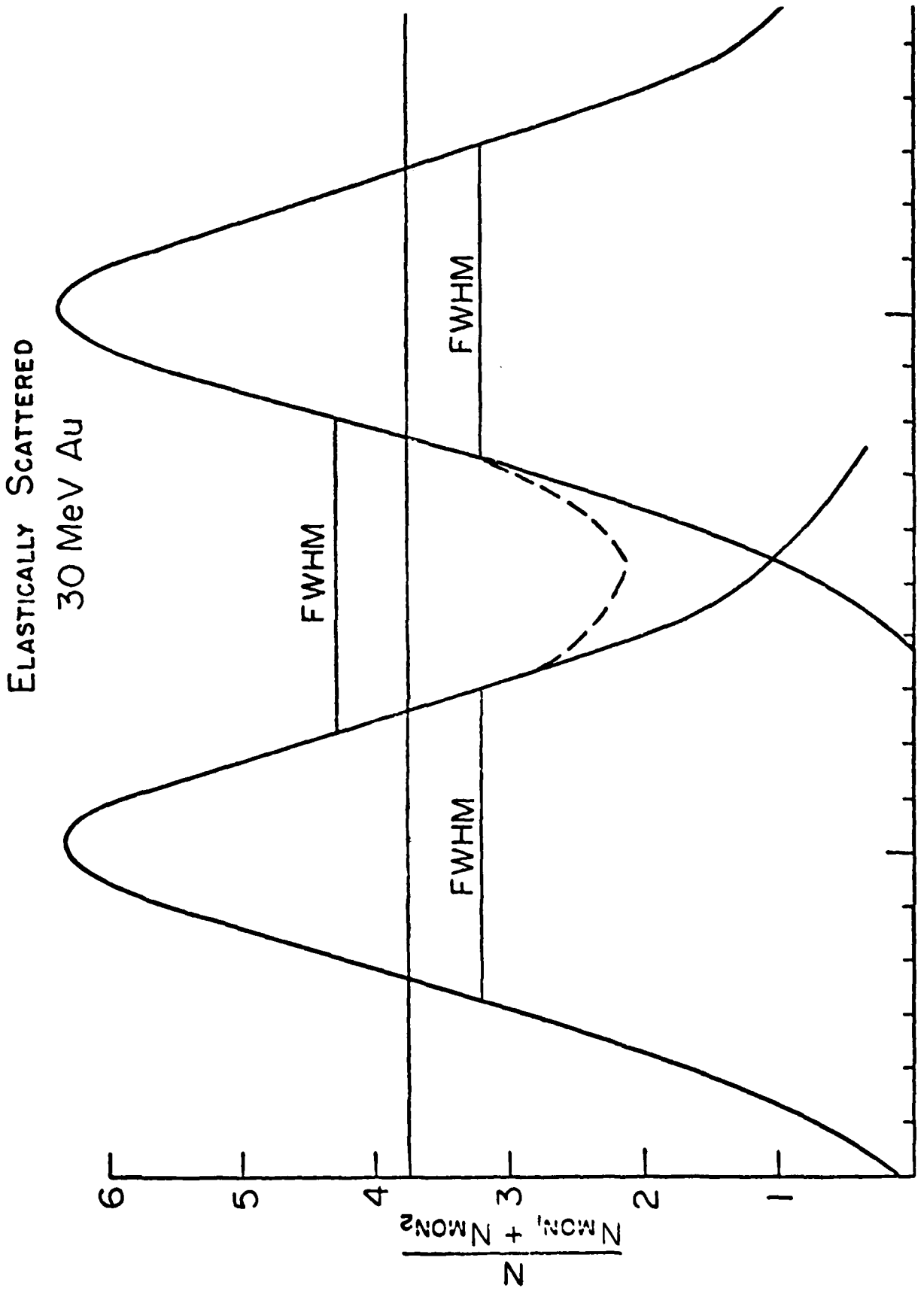
ELASTICALLY SCATTERED
30 MeV Au
FWHM
FWHM
FWHM
$\frac{N_{MON_1} + N_{MON_2}}{N}$
6
5
4
3
2
1
-6
0
10
ΔV/V %

FIGURE 18

were taken in 2 degree steps from 0 to 8 degrees. The absolute cross sections for each evaporation residue were then obtained by integrating the velocity bite taken at each angle over the 8 degrees of the angular distribution. This resulted in an absolute cross section for each evaporation residue at one particular lab energy. Then, based on the ratio of normalized counts to cross section at that energy, absolute cross section values could be scaled to other lab energies. Statistically this method is satisfactory when the angular and velocity distributions are taken at the peak of a particular evaporation residue excitation function; however when the cross section must be scaled from the tail of a distribution, a correspondingly large statistical error is carried forward. This is displayed in the large errors in some of the low cross section reactions.

Figure 19 shows the velocity distributions for a variety of evaporation residues. The compound nucleus with a forward velocity in the CM frame, will change velocity with each evaporation. A pure neutron cascade (i.e. 4n) will produce little deviation in velocity since there is no coulombic barrier to overcome. The charged protons and alphas impart a much greater change in velocity and their respective distributions are therefore not center peaked.

A difficulty arises in determining whether a particular evaporation residue is a daughter (alpha decay in the detector) or the result of a prompt alpha emission. The evidence for the prompt

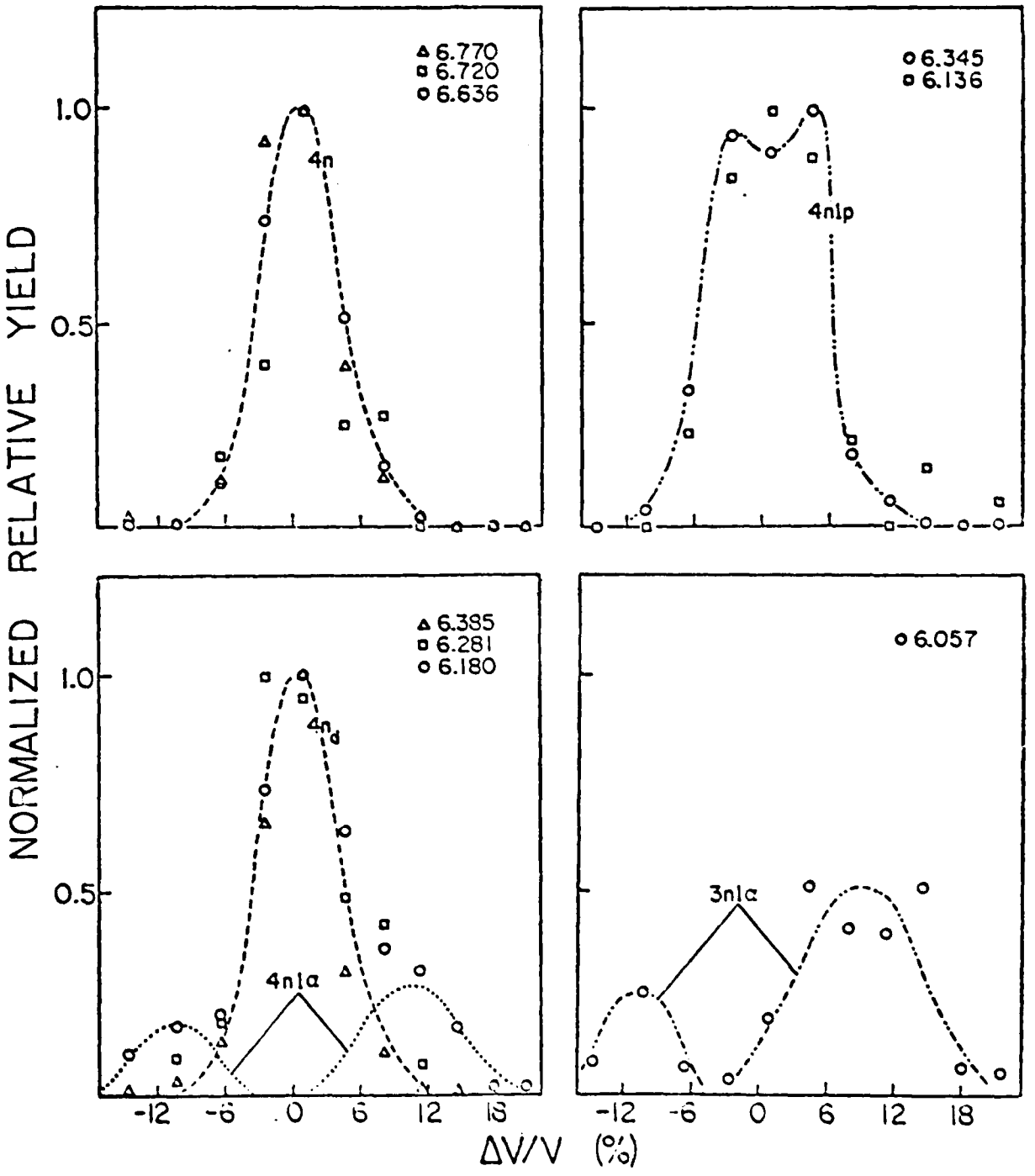
NORMALIZED RELATIVE YIELD
1.0
0.5
6.770
6.720
6.636
4n
6.345
6.136
4n1p
6.385
6.281
6.180
4nd
4n1α
6.057
3n1α
-12
-6
0
6
12
18
ΔV/V (%)

FIGURE 19

alpha is obtained by subtracting the parent distribution (i.e. 4n) from the daughter (i.e. 4nα); the resultant distribution (not center peaked) is that of the prompt alpha emission. This is shown in figure 19 where the 6.636 MeV (upper left) parent is subtracted from the 6.180 MeV daughter (lower left) resulting in the 4nlα parent evaporation residue (dotted line). All prompt alpha evaporation residues in this study were obtained in this manner.

Figure 20 shows the angular distributions for several evaporation residues. Here also the prompt alpha angular distributions were determined in the same manner as the velocity profiles. Figure 21 shows the BETH program analysis for comparison. It should be noted that the BETH results are an integration over a wider than normal velocity profile. This results, especially, in the alpha case, in a broadening of the angular distribution and an increase in the zero degree values. BETH calculates the distribution only on a kinematic basis with no regard for nuclear or RMS effects. Measured results are less distinct due to energy loss, straggling and multiple scattering in the target.

Figure 22 shows the excitation functions for the parent and daughter evaporation residues plotted versus lab energy. Note the "tracking" of each daughter under its respective parent. The predominant peak at ^{202}Rn (4n) is the major contributor to the total cross section plotted in figure 23 with a peak evaporation cross section at 1600 μb ± 300 at 165 MeV.

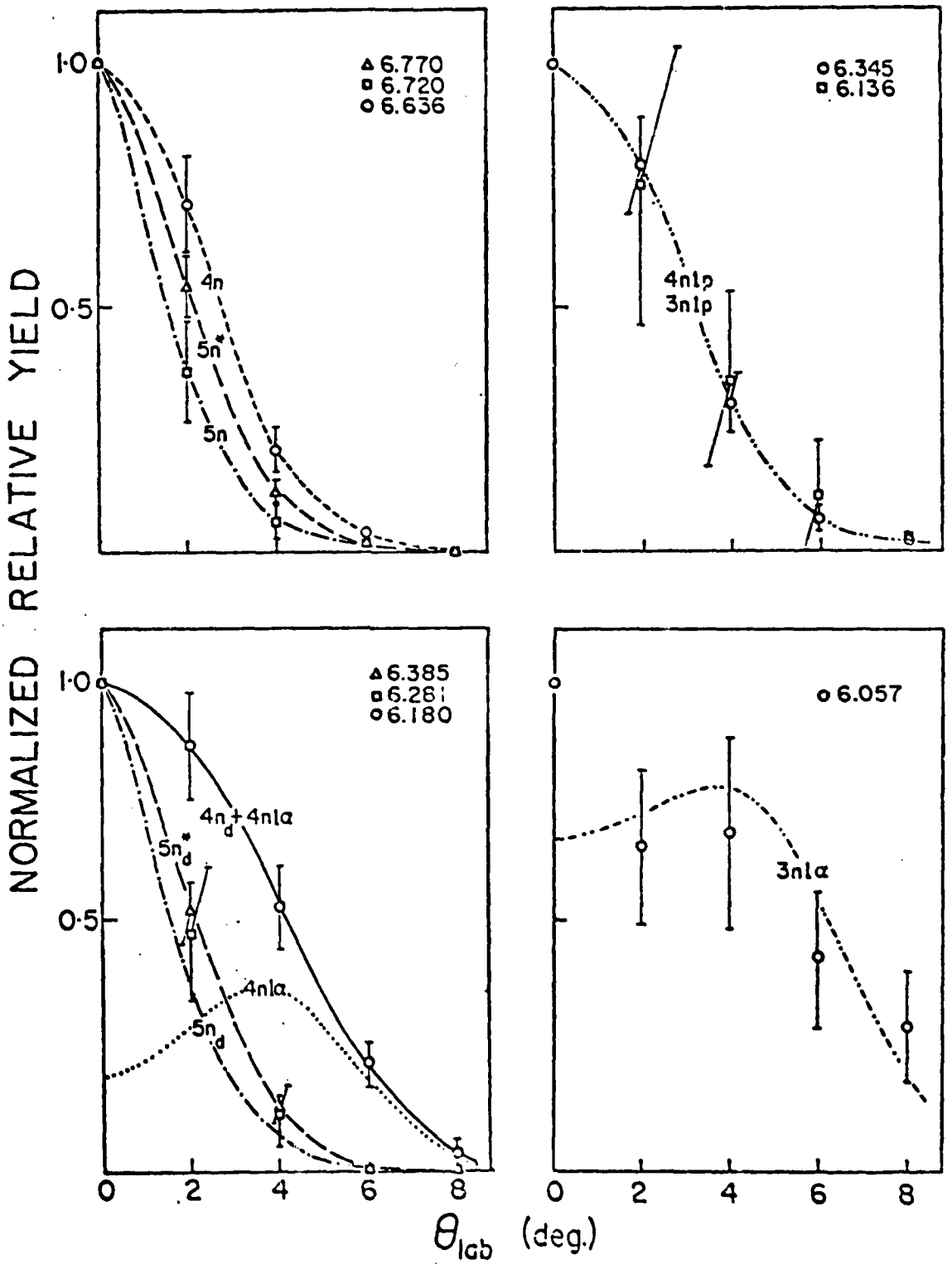
NORMALIZED RELATIVE YIELD
1·0
0·5
△ 6.770
□ 6.720
○ 6.636
4n
5n*
5n
○ 6.345
□ 6.136
4n1p
3n1p
△ 6.385
□ 6.281
○ 6.180
4n_d + 4n1α
5n*_d
4n1α
5n_d
○ 6.057
3n1α
0
2
4
6
8
θ_lab (deg.)

FIGURE 20

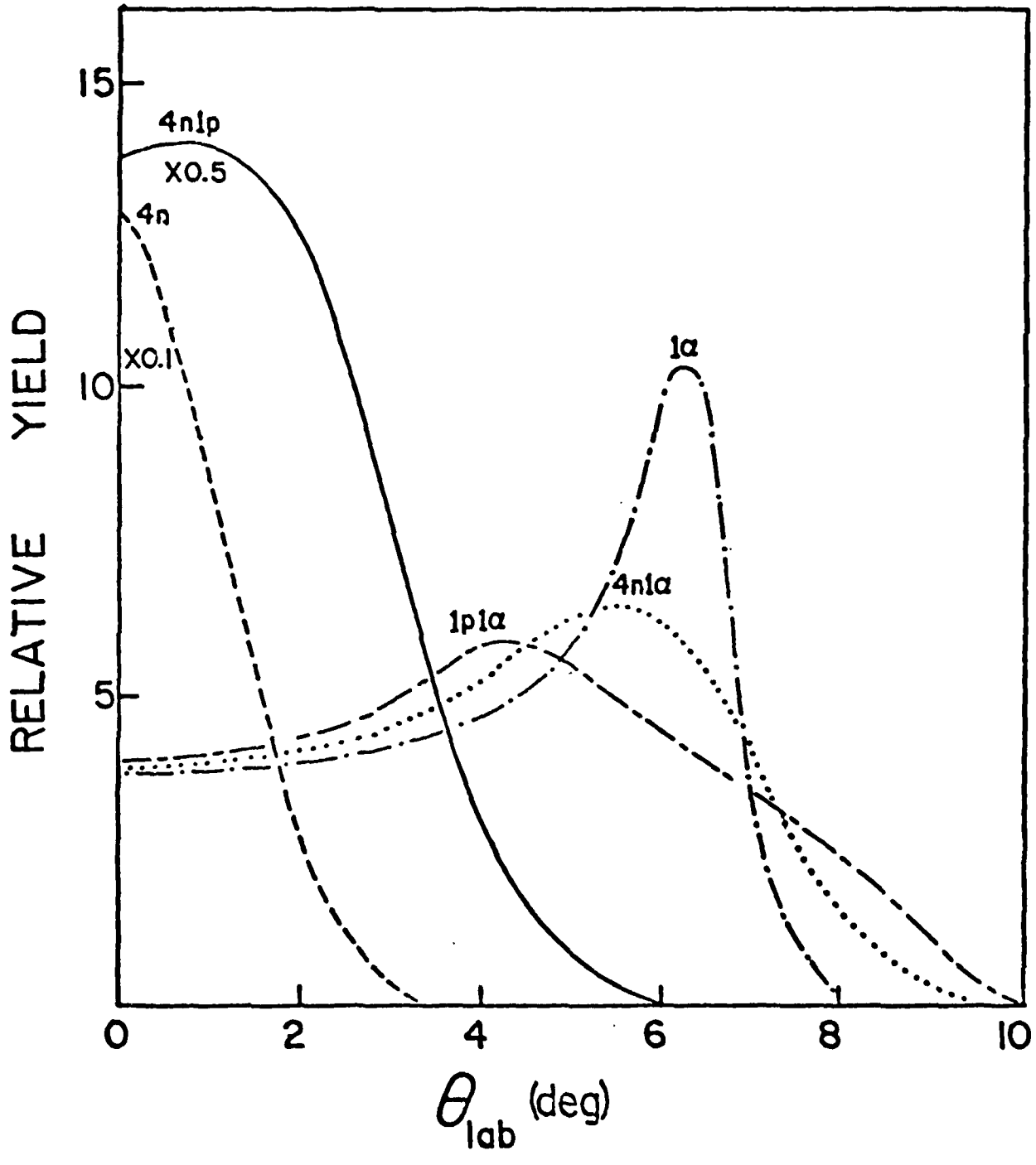
RELATIVE YIELD
15
10
5
0
2
4
6
8
10
4n1p
X0.5
4n
X0.1
1α
4n1α
1p1α
θlab (deg)

FIGURE 21

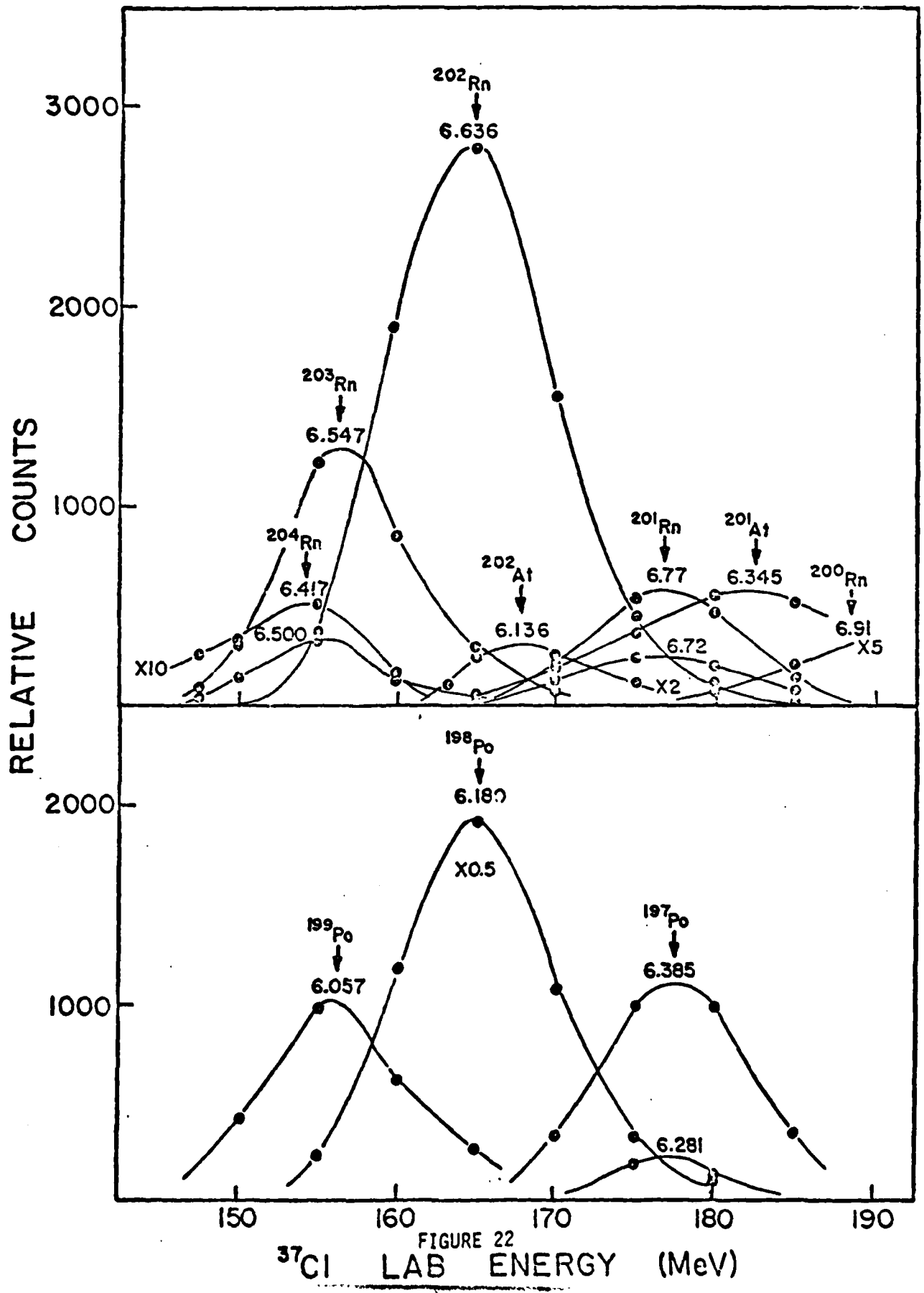
RELATIVE COUNTS
3000
2000
1000
2000
1000
202Rn
6.636
203Rn
6.547
204Rn
6.417
6.500
X10
202At
6.136
201Rn
6.77
201At
6.345
200Rn
6.91
X5
6.72
X2
198Po
6.180
X0.5
199Po
6.057
197Po
6.385
6.281
150
160
170
180
190
37Cl LAB ENERGY (MeV)

FIGURE 22

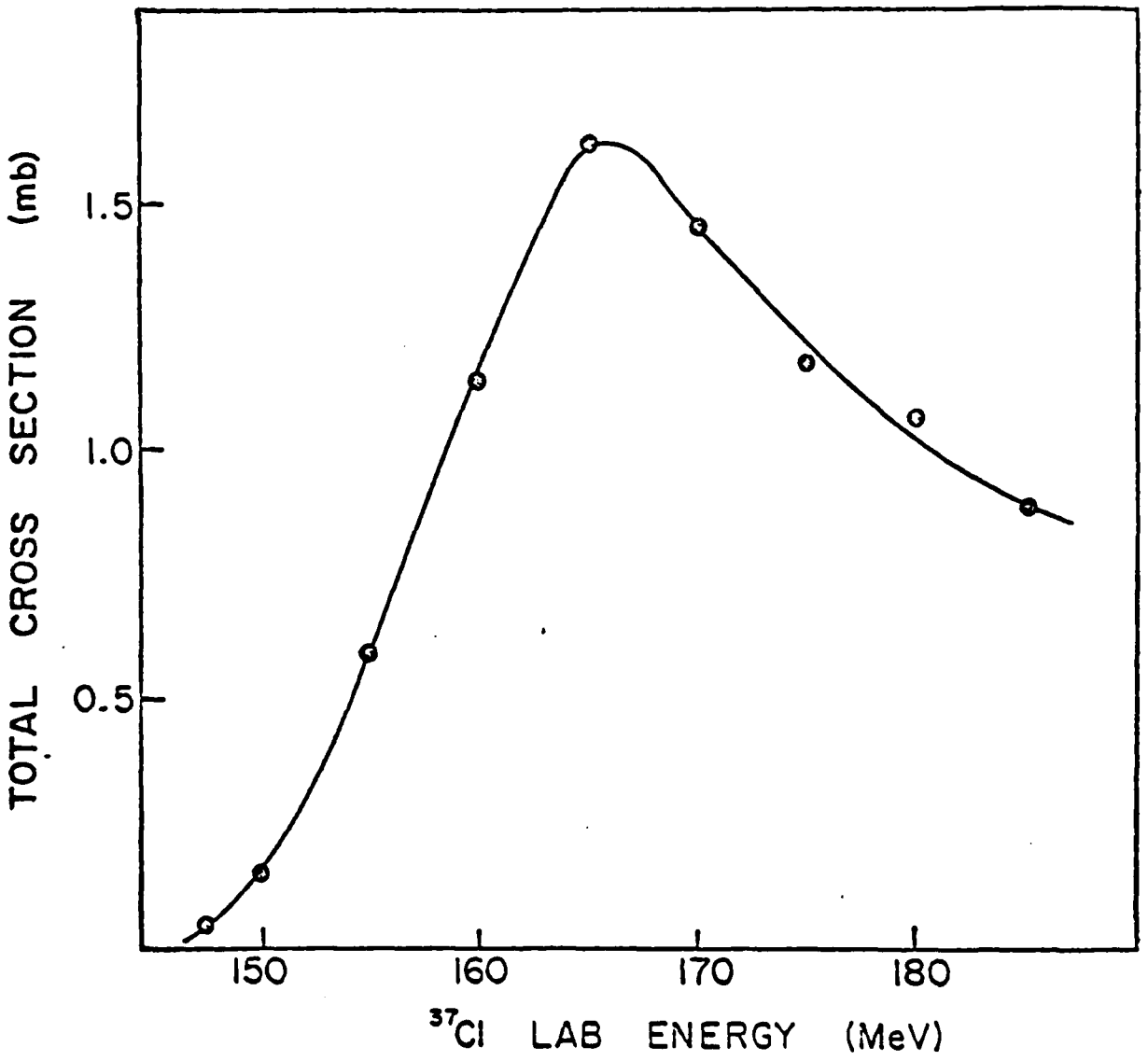
TOTAL CROSS SECTION (mb)
1.5
1.0
0.5
150
160
170
180
^{37}Cl LAB ENERGY (MeV)

FIGURE 23

B. $^{35}Cl + {}^{169}Tm$

This reaction was selected as a midpoint reaction in the Z^2/A distribution and to show the effects of a small decrease in the neutron number (and hence an increase in the value of Z^2/A). This reaction was also included in an analysis of the effects of excitation energy and angular momentum on evaporation residue formation. In that study the same compound nucleus (^{204}Rn) was formed through the reactions of $^{65}Cu + {}^{139}La$ and $^{35}Cl + {}^{169}Tm$. The copper reaction is not included in this study since the data is incomplete. A much more complete set of excitation functions was obtained for the chlorine reaction.

Figures 25 to 27 show the angular distributions for several of the parent evaporation residues. Figure 25 shows the contrast between the pure neutron and the neutron and alpha evaporation angular distributions. The large values at angles 4 and 6 degrees are the major contributors to the high cross section values for the alpha evaporation residues since the multiplication of the differential cross section by sin θ near zero degree results in a near zero contribution to the absolute cross section. (See Table III.) The velocity distribution for this reaction was obtained using the three point method. The value of ±10% of v_o was chosen since the peak of alpha evaporations should occur in that region.

Figures 28 to 31 show the excitation functions of the several evaporation residues of this reaction. Figure 28 is significant in that it is very similar to the $^{37}Cl + {}^{169}Tm$ reaction

in both the position of the excitation functions and their relative peak heights. Of further interest are the sets of other excitation functions involving alphas and protons mixed with neutrons in evaporation. Here, as in several other reactions, the 4np and the 3nα reactions are the strongest. Also of note is the presence of the 2n2p and 3n2p evaporation modes. These are purposely listed as shown rather in an alpha designation since they occur at high excitation energies and in regions where 4 or 5 particle evaporations occur. (See Figures 29 to 31.) The total evaporation residue cross section in shown in Figure 32. The large errors associated with the 160-165 MeV lab energy range are due primarily to the 4n excitation function since, as previously mentioned, the cross section scaling was based on a low 4n value at a lab energy of 175 MeV and the error was correspondingly scaled. In Table III is shown the individual cross sections that contribute to the total evaporation residue cross section function.

This reaction produced the new isotope ^{199}Rn and its metastable state ^{199n}Rn.[40] It was possible to predict the expected alpha decay energy by charting the decay ssystematics of the neighboring Radan, Astatine, Polonium and Francium isotopes. Figure 24 shows the decay systematics and the position of the ^{199}Rn and ^{199m}Rn isotopes (open circles). Also shown are the alpha decay energies of the Polonium daughters. New alpha decay energies are:

^{199}Rn 6.99 MeV

^{199m}Rn 7.06 MeV

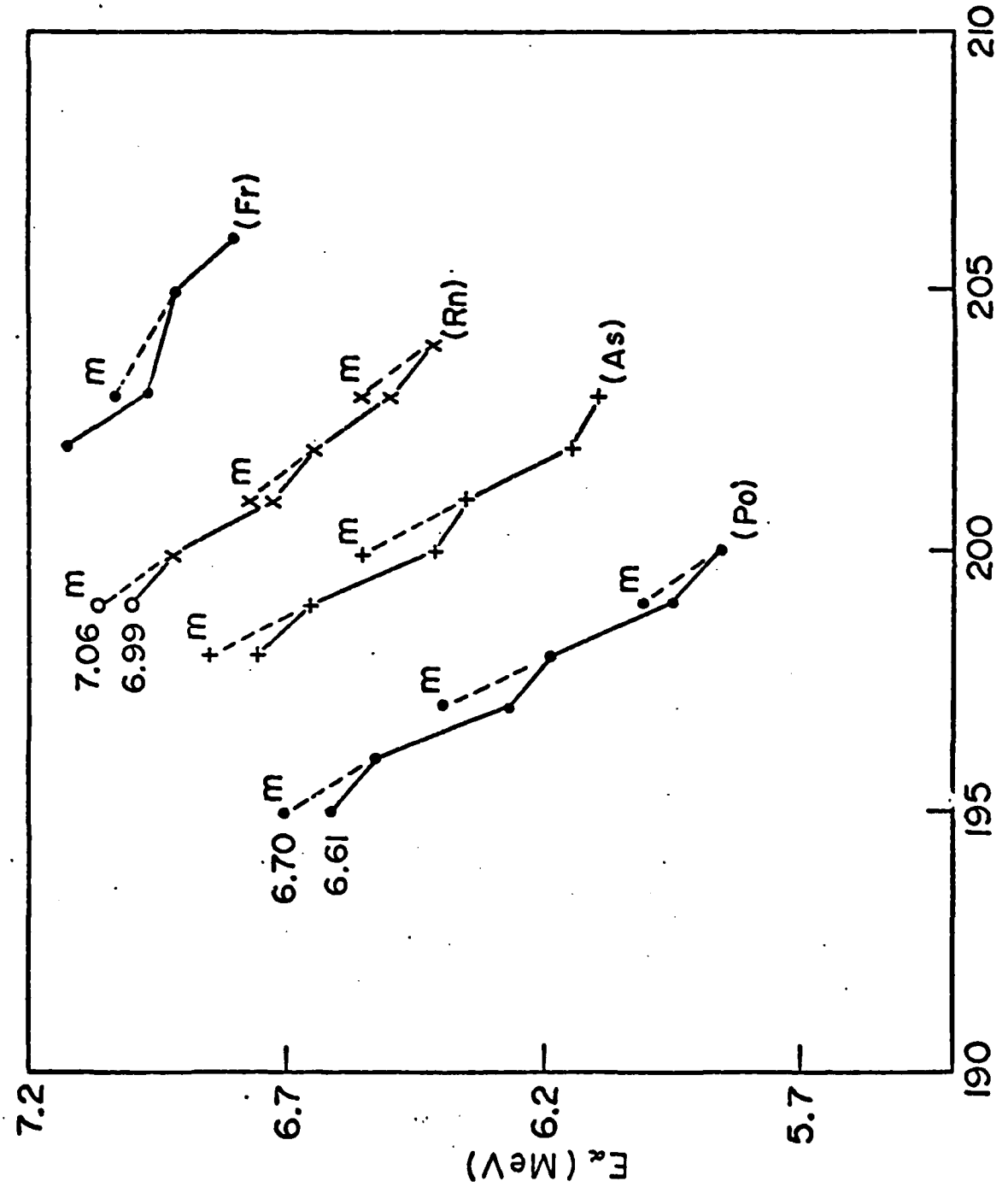
(Fr)
(Rn)
(As)
(Po)
m
7.06
6.99
6.70
6.61
7.2
6.7
6.2
5.7
E_α (MeV)
190
195
200
205
210
Atomic Mass

FIGURE 24

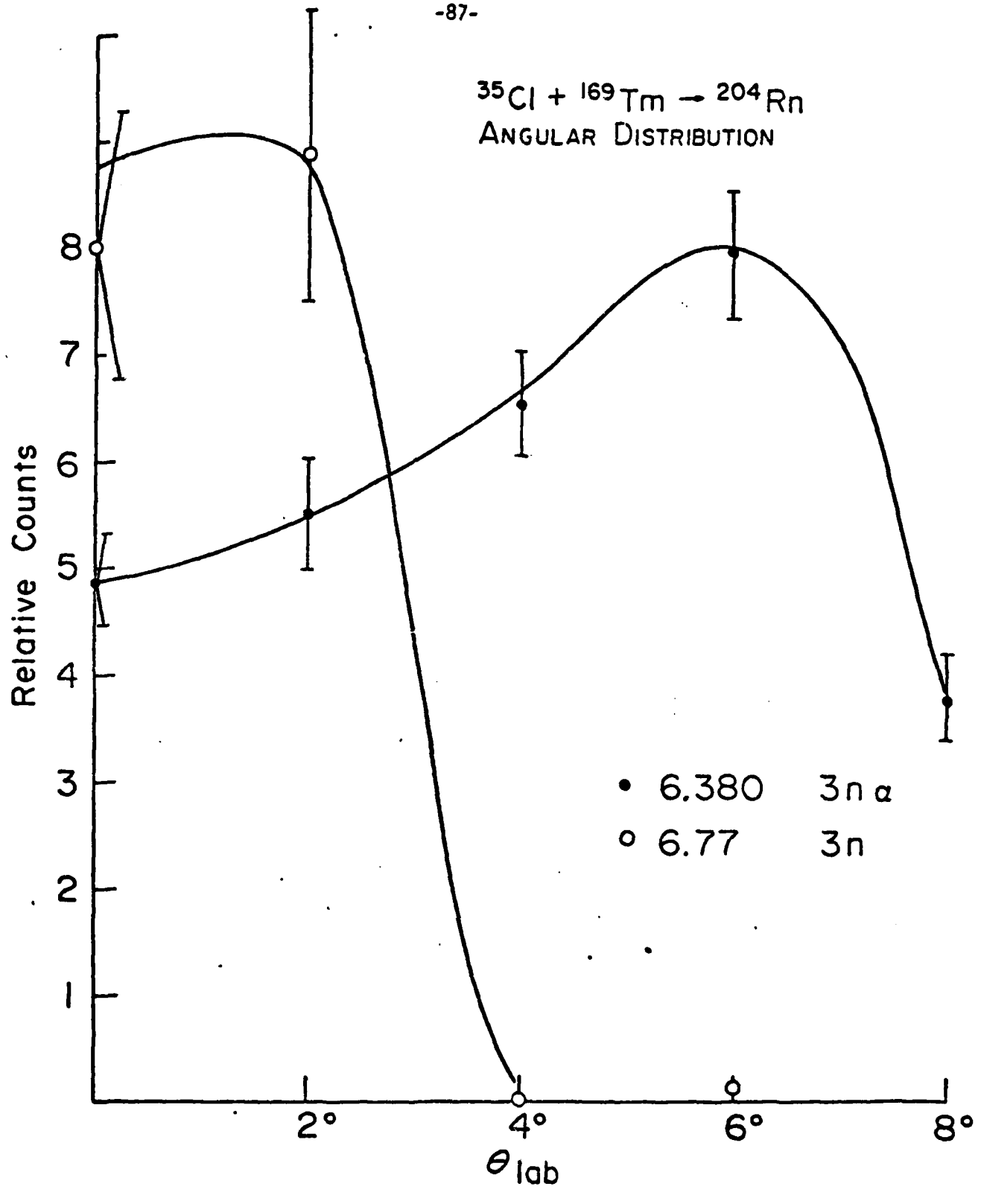
$^{35}Cl + ^{169}Tm \rightarrow ^{204}Rn$
ANGULAR DISTRIBUTION
Relative Counts
1
2
3
4
5
6
7
8
2°
4°
6°
8°
θ_{lab}
• 6.380 3n α
° 6.77 3n

FIGURE 25

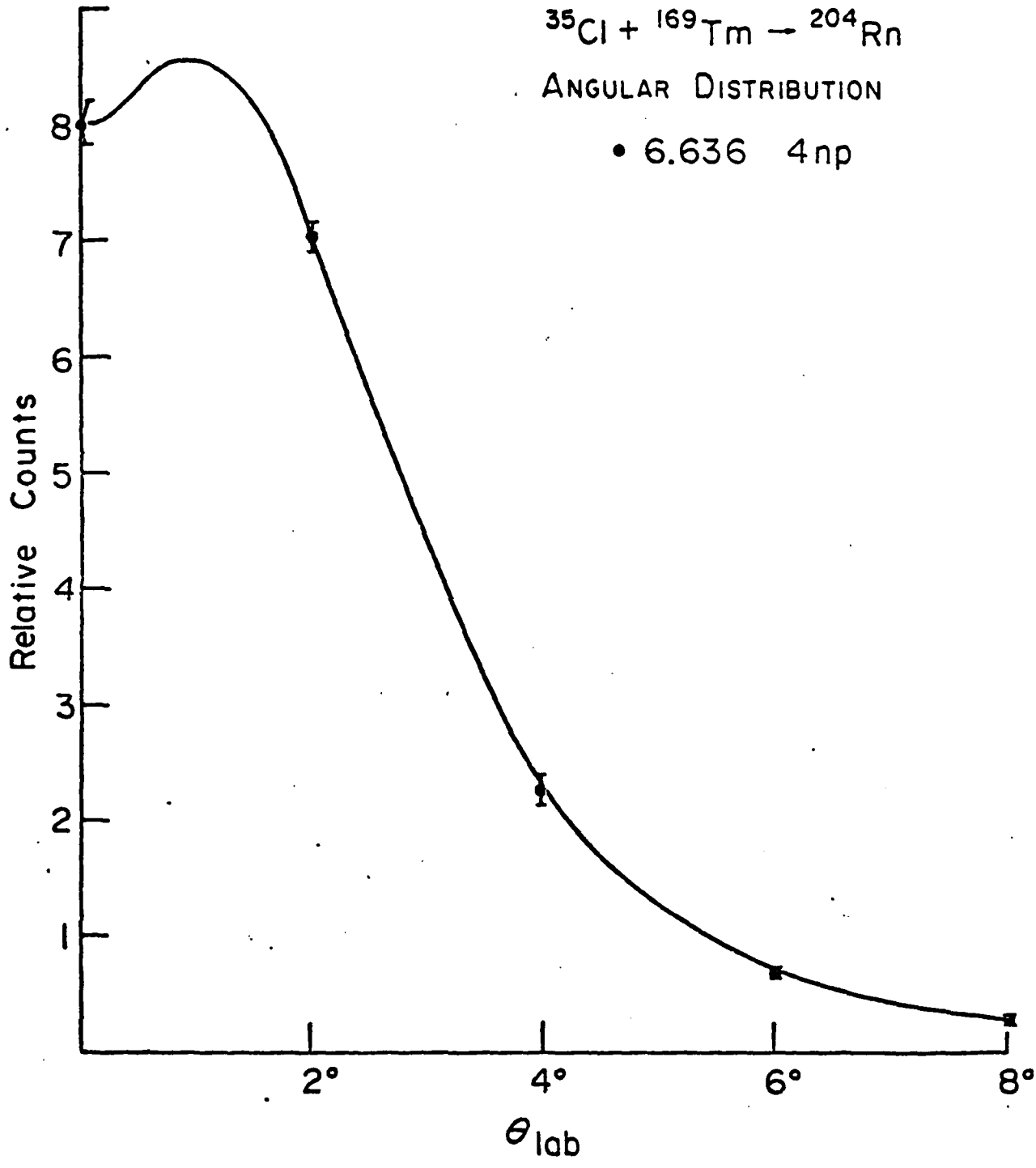
$^{35}Cl + {}^{169}Tm \rightarrow {}^{204}Rn$
ANGULAR DISTRIBUTION
• 6.636 4np
Relative Counts
1
2
3
4
5
6
7
8
2°
4°
6°
8°
θ_{lab}

FIGURE 26

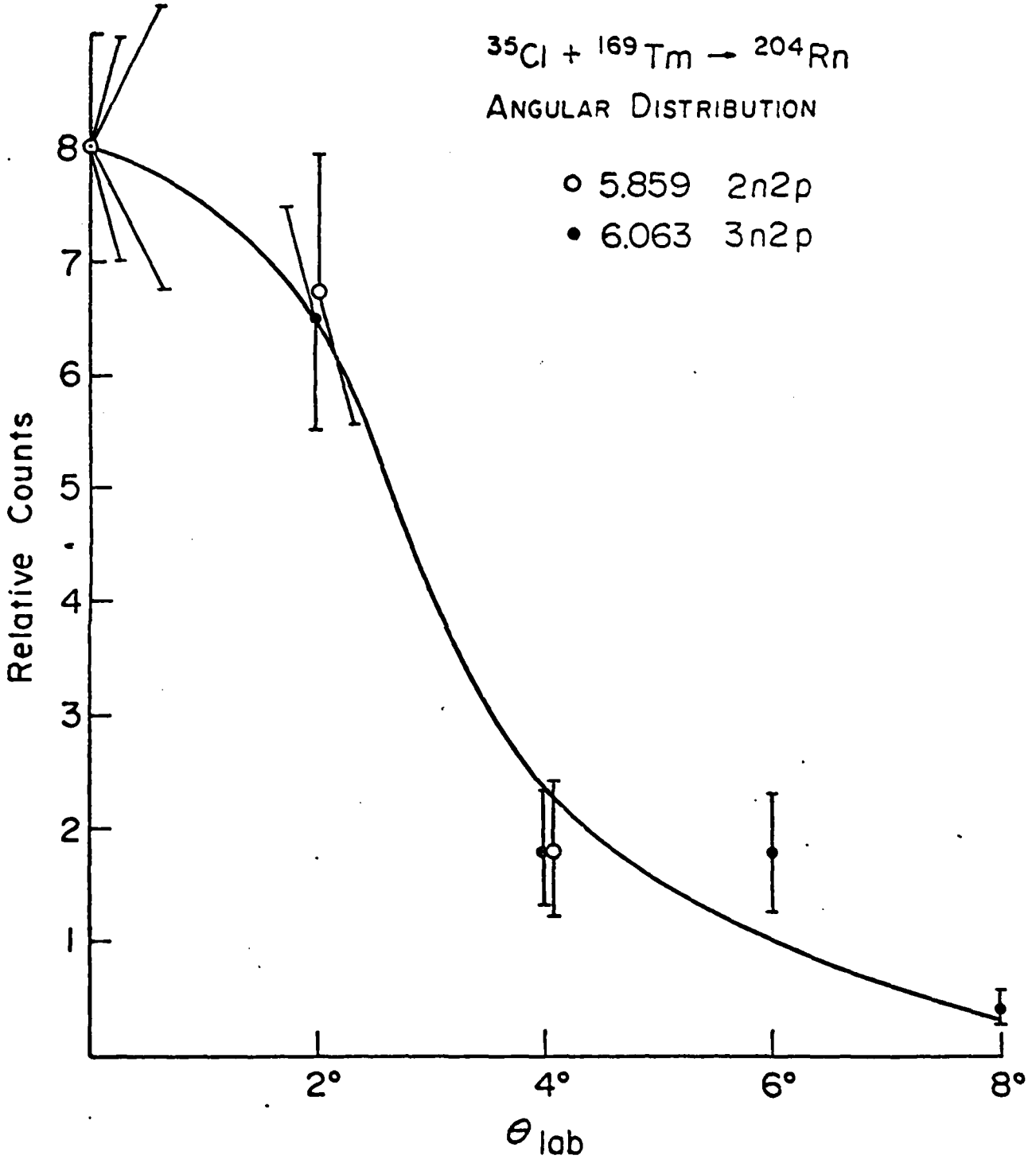
$^{35}Cl + {}^{169}Tm \rightarrow {}^{204}Rn$
ANGULAR DISTRIBUTION
o 5.859 2n2p
• 6.063 3n2p
Relative Counts
8
7
6
5
4
3
2
1
2°
4°
6°
8°
θ_{lab}

FIGURE 27

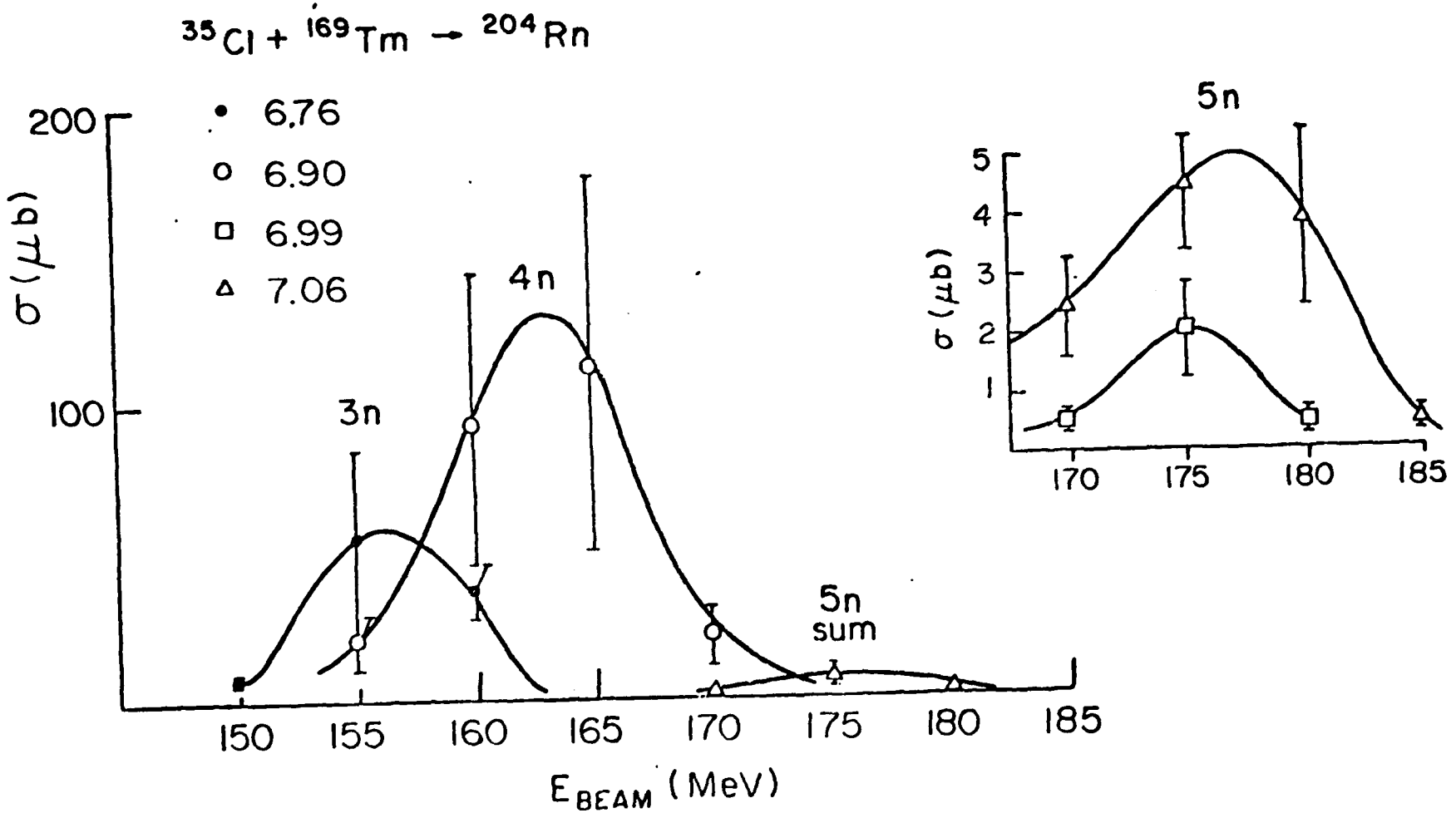
$^{35}Cl + ^{169}Tm \rightarrow ^{204}Rn$
• 6.76
o 6.90
□ 6.99
△ 7.06
σ (μb)
200
100
3n
4n
5n
sum
150
155
160
165
170
175
180
185
E_{BEAM} (MeV)
5n
σ (μb)
5
4
3
2
1
170
175
180
185

FIGURE 28

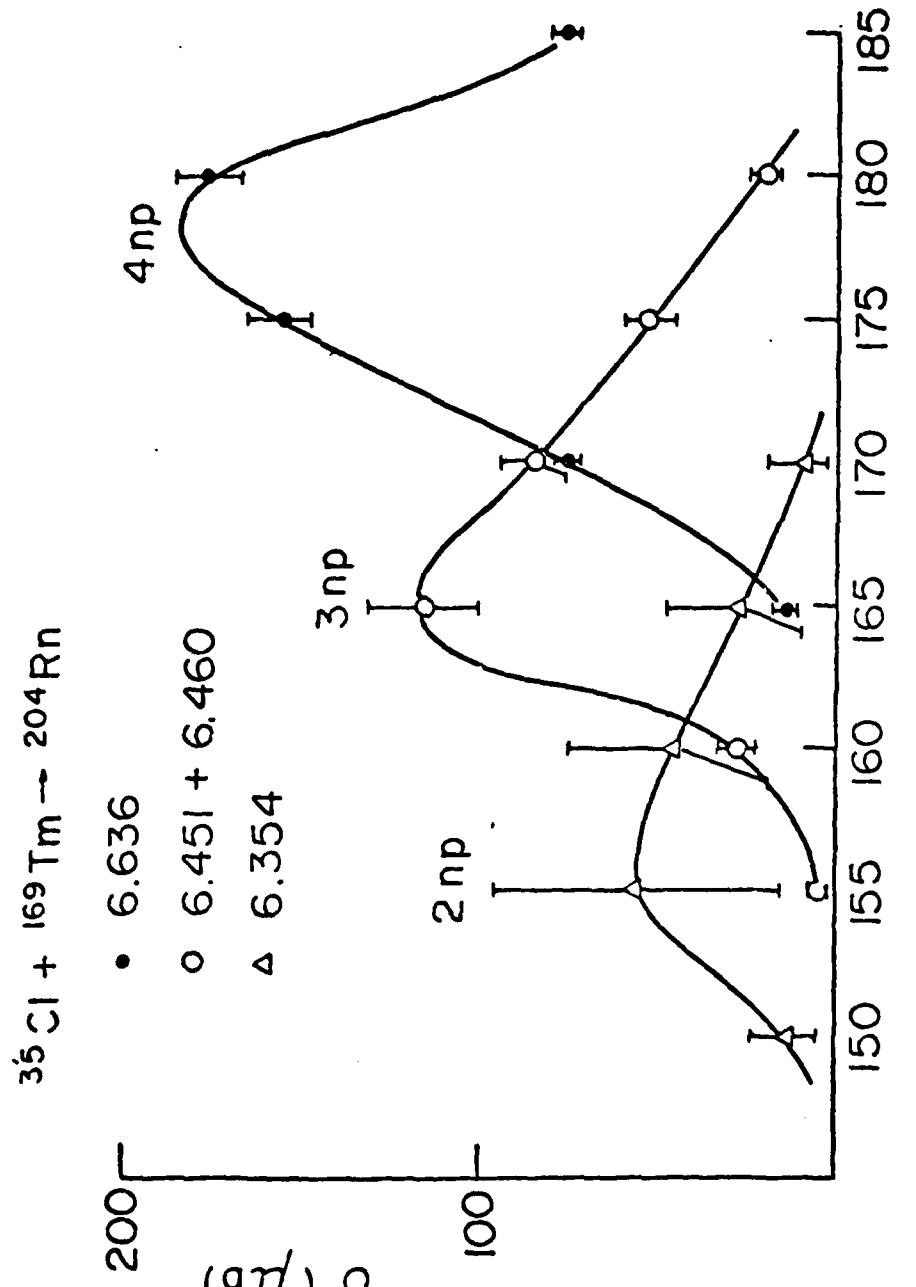
$^{35}Cl + ^{169}Tm \rightarrow ^{204}Rn$
• 6.636
○ 6.451 + 6.460
△ 6.354
4np
3np
2np
σ (μb)
200
100
150
155
160
165
170
175
180
185
E_{BEAM} (MeV)

FIGURE 29

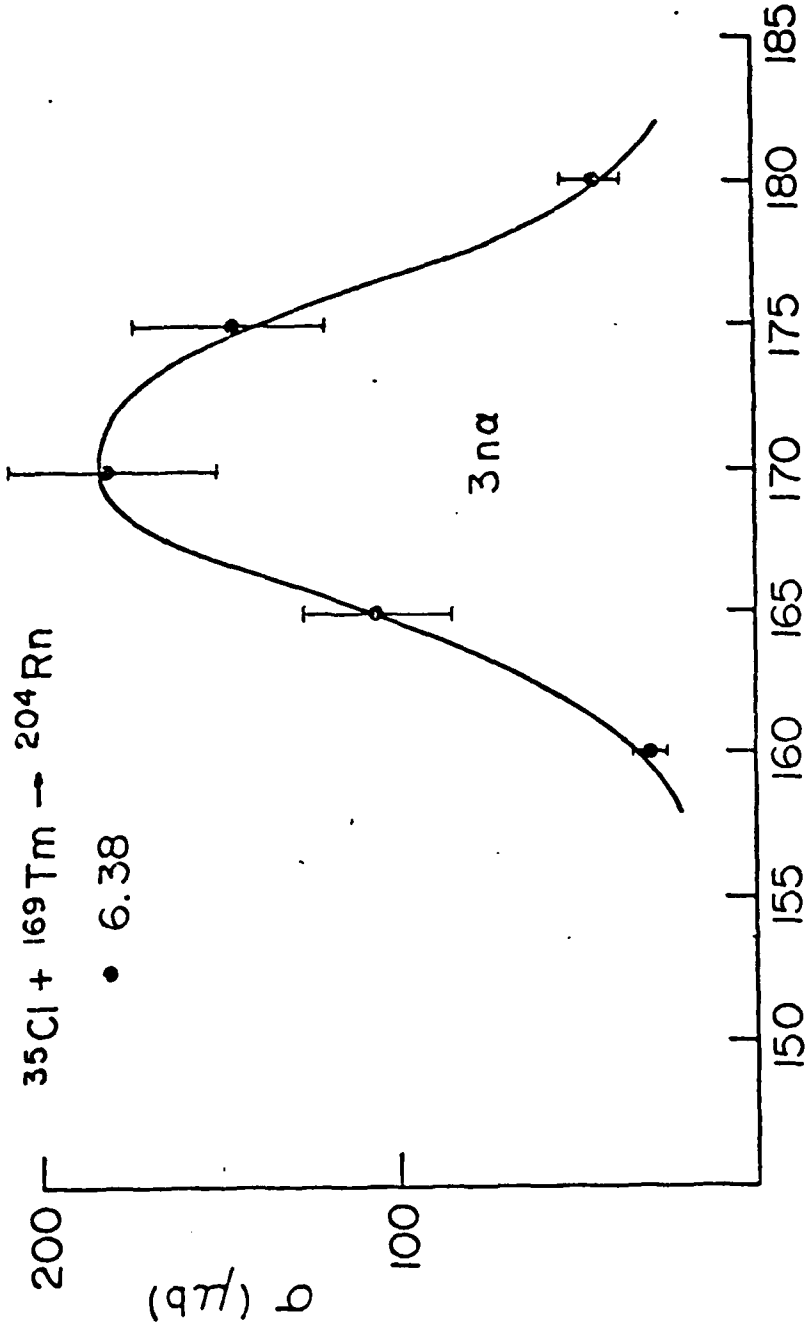
35Cl + 169Tm → 204Rn
• 6.38
3nα
σ (μb)
200
100
150
155
160
165
170
175
180
185
E BEAM (MeV)

FIGURE 30

AD-A084 863 ARMY MILITARY PERSONNEL CENTER ALEXANDRIA VA F/G 20/8
THE Z2/A DEPENDENCE IN HEAVY-ION FUSION FOR THE REACTIONS OF CH--ETC(U)
JUN 80 A C DIRIENZO

UNCLASSIFIED NL

2 OF 2
AD
A084863

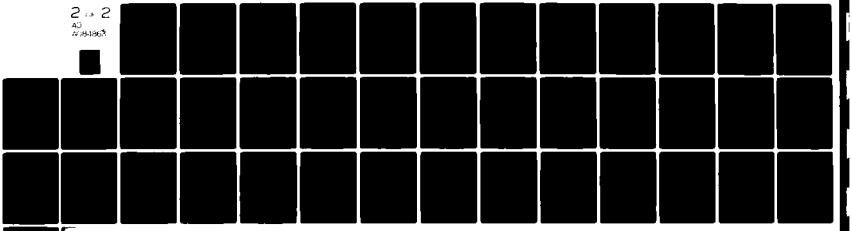

END
DATE FILMED
7 80
DTIC

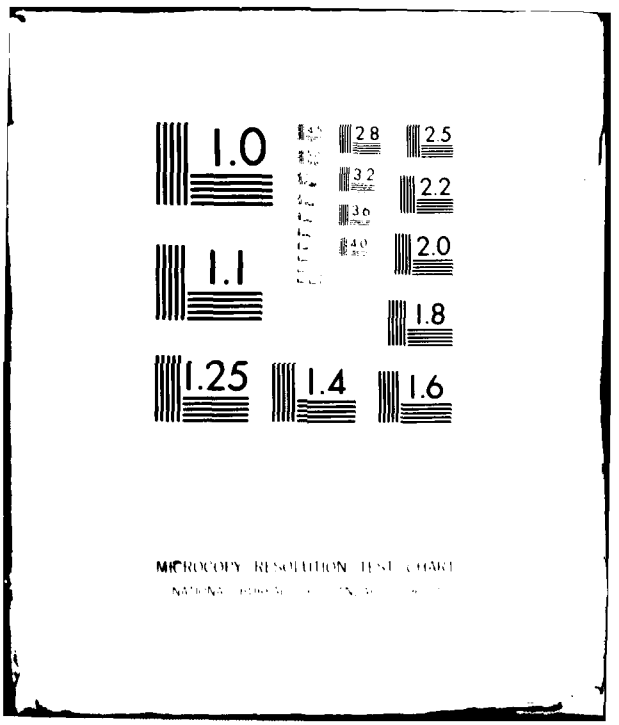
1.0
1.1
1.25
1.4
1.6
1.8
2.0
2.2
2.5
2.8
3.2
3.6
4.0
MICROCOPY RESOLUTION TEST CHART

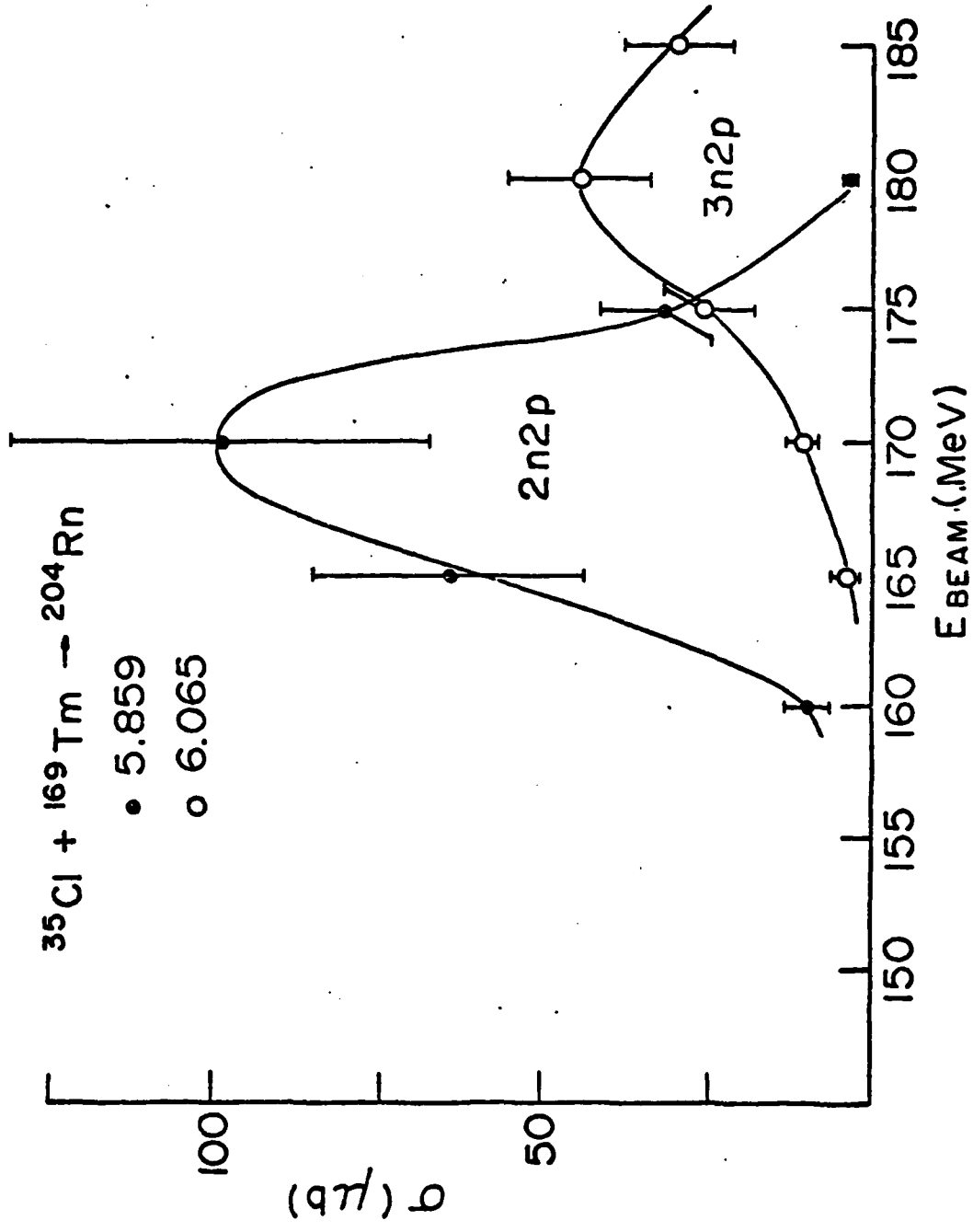
$^{35}Cl + ^{169}Tm \rightarrow ^{204}Rn$
• 5.859
o 6.065
2n2p
3n2p
σ (μb)
100
50
150
155
160
165
170
175
180
185
E BEAM (MeV)

FIGURE 31

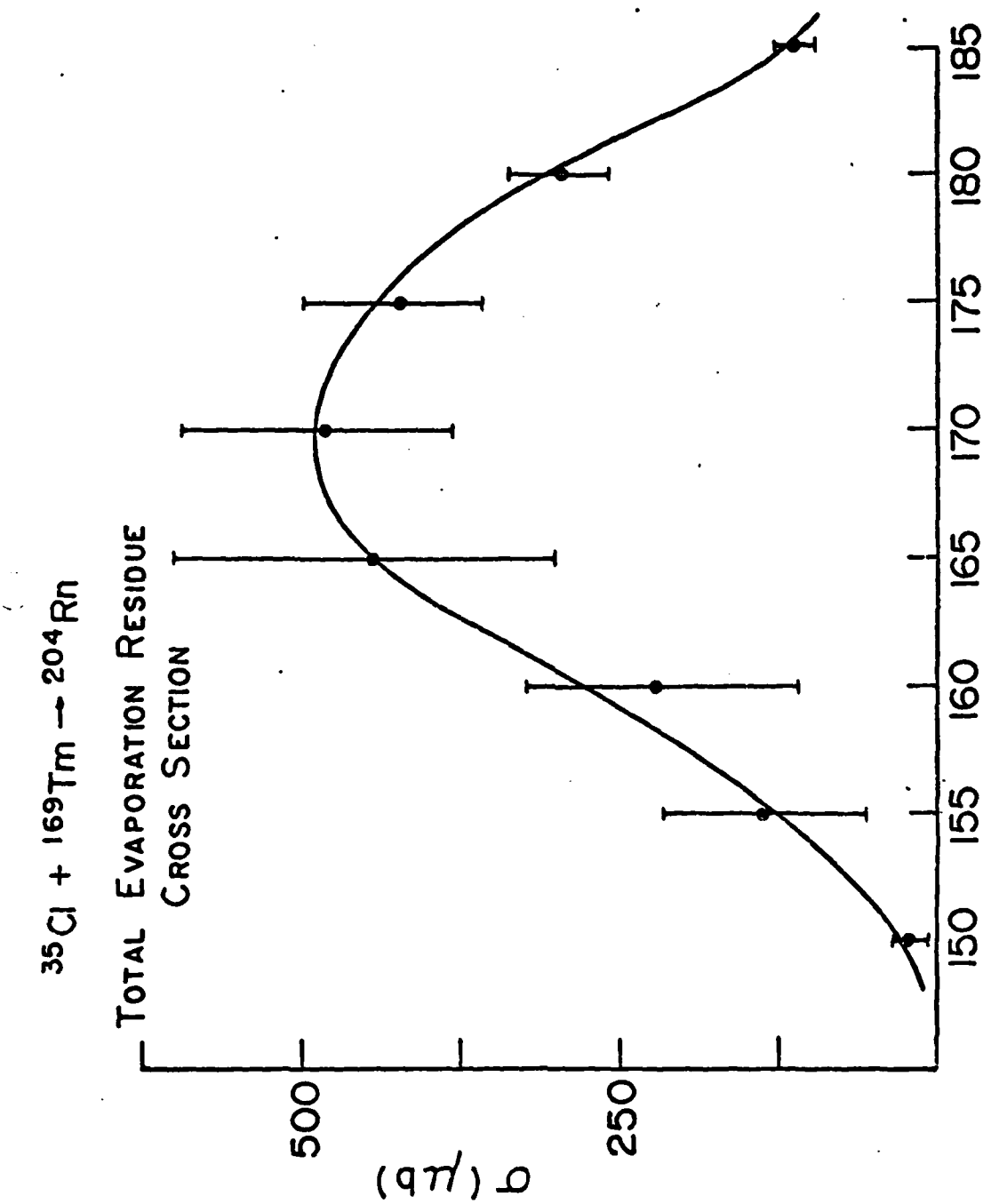
$^{35}Cl + ^{169}Tm \rightarrow ^{204}Rn$
Total Evaporation Residue
Cross Section
σ (μb)
500
250
150
155
160
165
170
175
180
185
E_{BEAM} (MeV)

FIGURE 32

TABLE III

Absolute Cross Sections (in μb) for $^{35}Cl + ^{169}Tm$

E_{Lab}(MeV) / E_α(MeV)	150	155	160	165	170	175	180	185
2n2p 5.859			9.4 ±3.1	64.3 ±21.4	98.1 ±32.7	31.1 ±10.4	3.1 ±1.0	
3n2p 6.063				4.4 ±1.2	10.4 ±2.9	25.6 ±7.1	44.0 ±12.2	29.2 ±8.2
2np 6.354	13.9 ±9.8	58.8 ±41.5	45.0 ±31.8	28.9 ±20.4	10.9 ±7.7	2.9 ±2.1	1.3 ±.9	
3np 6.415		5.7 ±.7	23.2 ±3.0	100.0 ±12.9	74.4 ±9.6	47.1 ±6.1	17.2 ±2.2	4.2 ±1.8
3np 6.460			6.2 ±2.5	16.9 ±6.9	11.2 ±4.6	7.1 ±2.9	4.2 ±1.7	
4np 6.636				15.6 ±.9	77.5 ±4.4	155.5 ±8.7	175.9 ±9.9	77.8 ±4.4
3n 6.77	7.3 ±4.2	53.8 ±31.1	17.2 ±9.9					
4n 6.900		20.0 ±11.5	93.1 ±53.8	111.9 ±64.6	20.3 ±11.7	3.2 ±1.8	1.8 ±1.0	
5n 6.990					.5 ±.1	2.0 ±.7	.5 ±.1	
5n 7.060				.5 ±.2	2.4 ±.8	4.4 ±1.0	3.9 ±1.4	.5 ±.2
3nα 6.380			28.4 ±5.5	105.9 ±20.4	181.1 ±34.9	145.1 ±27.9	44.0 ±8.5	
σ_{TOT}	21.1 ±14	138.3 ±84.8	222.5 ±109.8	448.5 ±148.9	486.8 ±109.4	424.0 ±68.8	295.9 ±38.9	111.9 ±14.6

c. $\underline{^{37}Cl + ^{175}Lu}$

This reaction begins the series of reactions with very low cross sections. The very plentiful ^{37}Cl beam was used in order to obtain beam currents of 200 na. The high beam current was chosen to optimize the fusion count rate even though it resulted in a nucleus with a high excitation. One study[41] of the program ALICE showed that high excitation energy resulted in a decreased evaporation residue production. The recommended projectile nucleus to minimize excitation energy was in the range of $\frac{A_{CN}}{3}$ or $\frac{2A_{CN}}{3}$, however the intensity factor of 100 gained by using the 200 na beam greatly offset the better production efficiency (larger cross section σ_{ER}) of the heavier beam.

Figures 33 to 35 show the angular distributions of the various evaporation residue modes. In the regime of this reaction, pairs of the evaporation residues by accident, exhibit identical alpha decay energies. Separate evaporation modes (i.e. 4n from 5n) could not be distinguished by using velocity or angular distributions as in the prompt alpha case, but through the energy (lab) distribution of their excitation functions. This is shown by the dashed lines in figures 36 to 39. Angular distributions again exhibit the characteristic shapes of their respective species. This constancy of distribution assists in the identification of individual evaporation residues and in the certification of prompt alpha evaporation modes. Figure 40 shows the total evaporation residue cross section for the $^{37}Cl + ^{175}Lu$ reaction. Individual cross sections are shown in Table IV for each mode of evaporation.

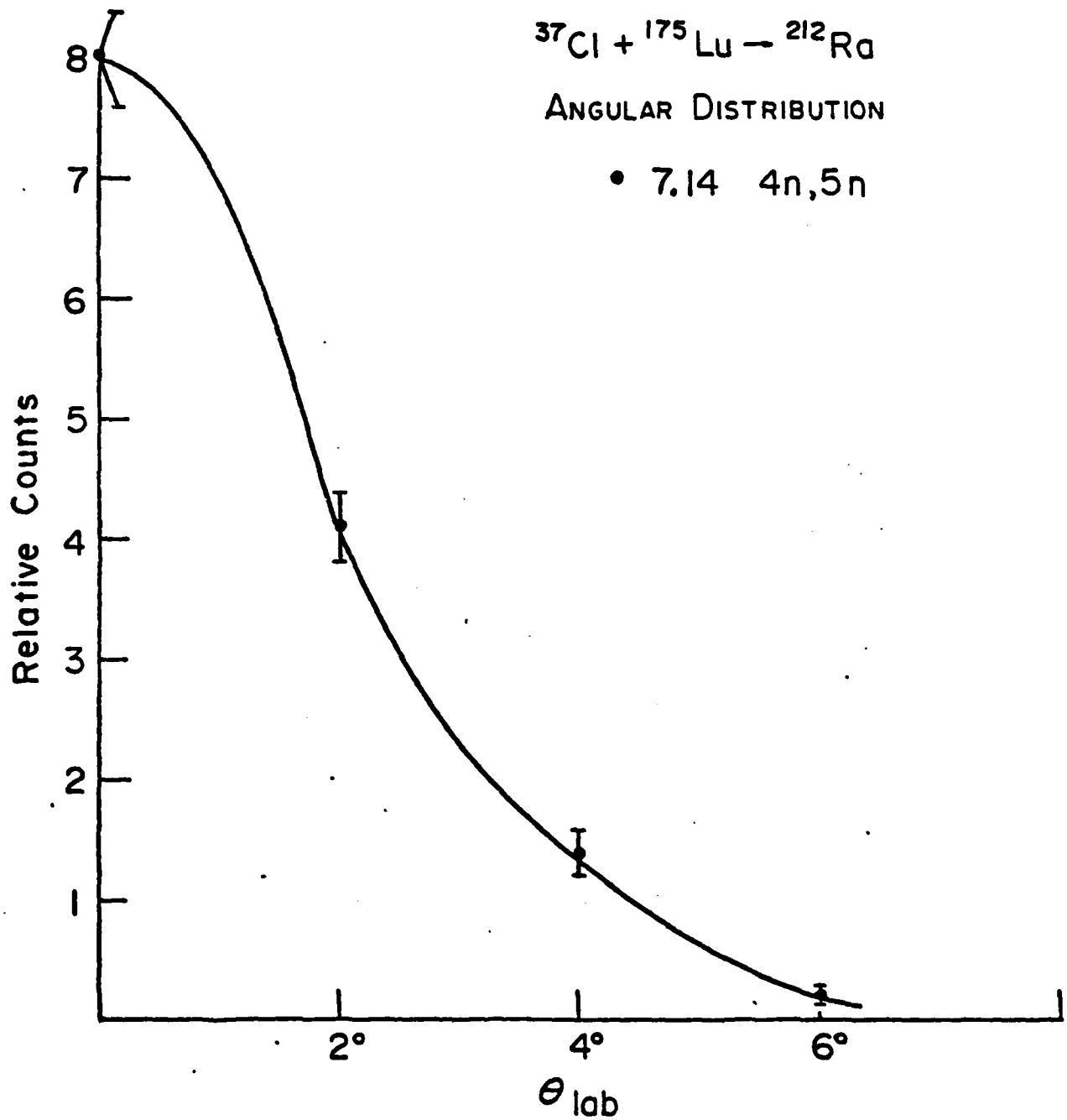
$^{37}Cl + ^{175}Lu \rightarrow ^{212}Ra$
ANGULAR DISTRIBUTION
• 7.14 4n,5n
Relative Counts
8
7
6
5
4
3
2
1
2°
4°
6°
θ lab

FIGURE 33

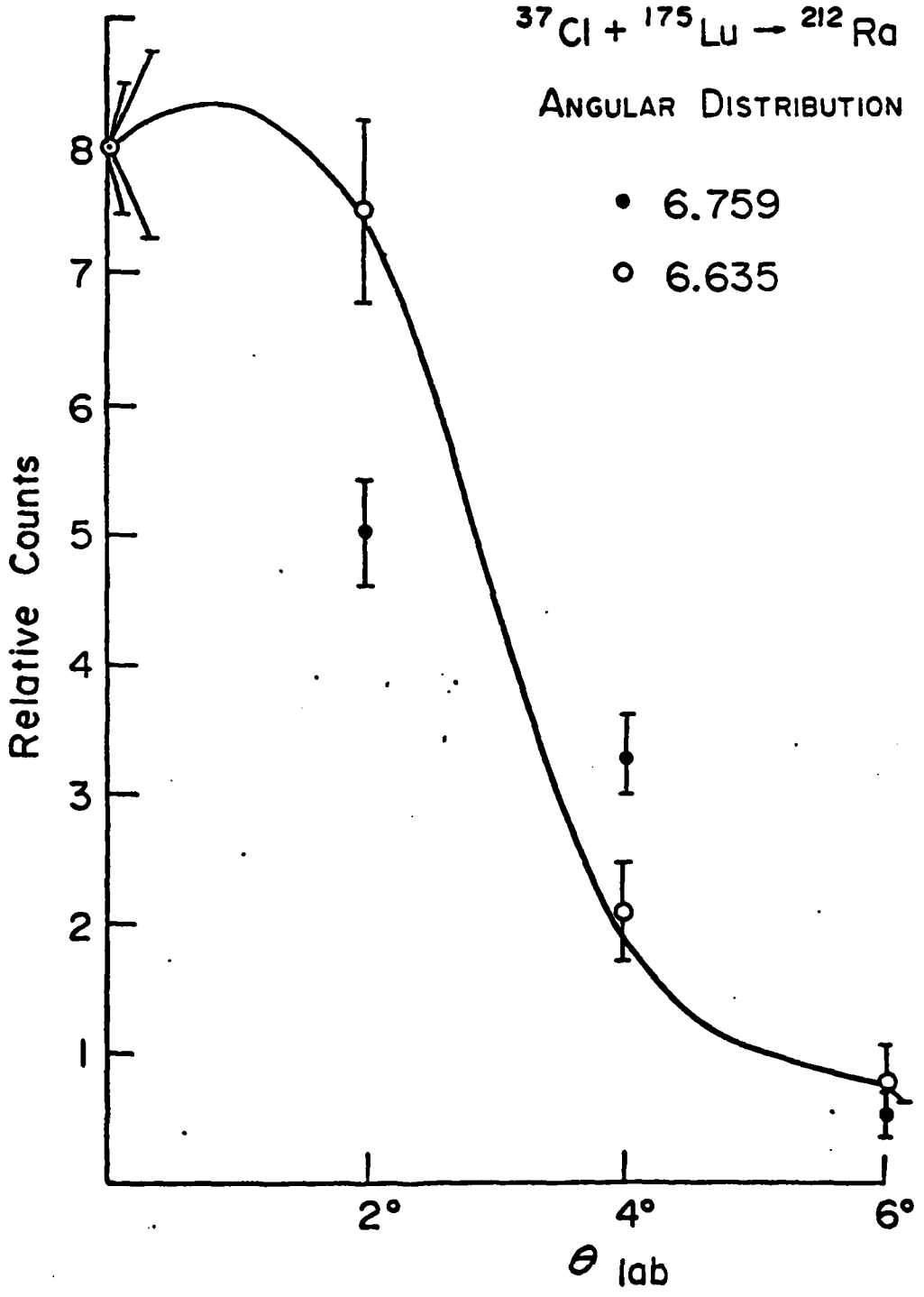
$^{37}Cl + ^{175}Lu \rightarrow ^{212}Ra$
Angular Distribution
• 6.759
○ 6.635
Relative Counts
8
7
6
5
4
3
2
1
2°
4°
6°
θ lab

FIGURE 34

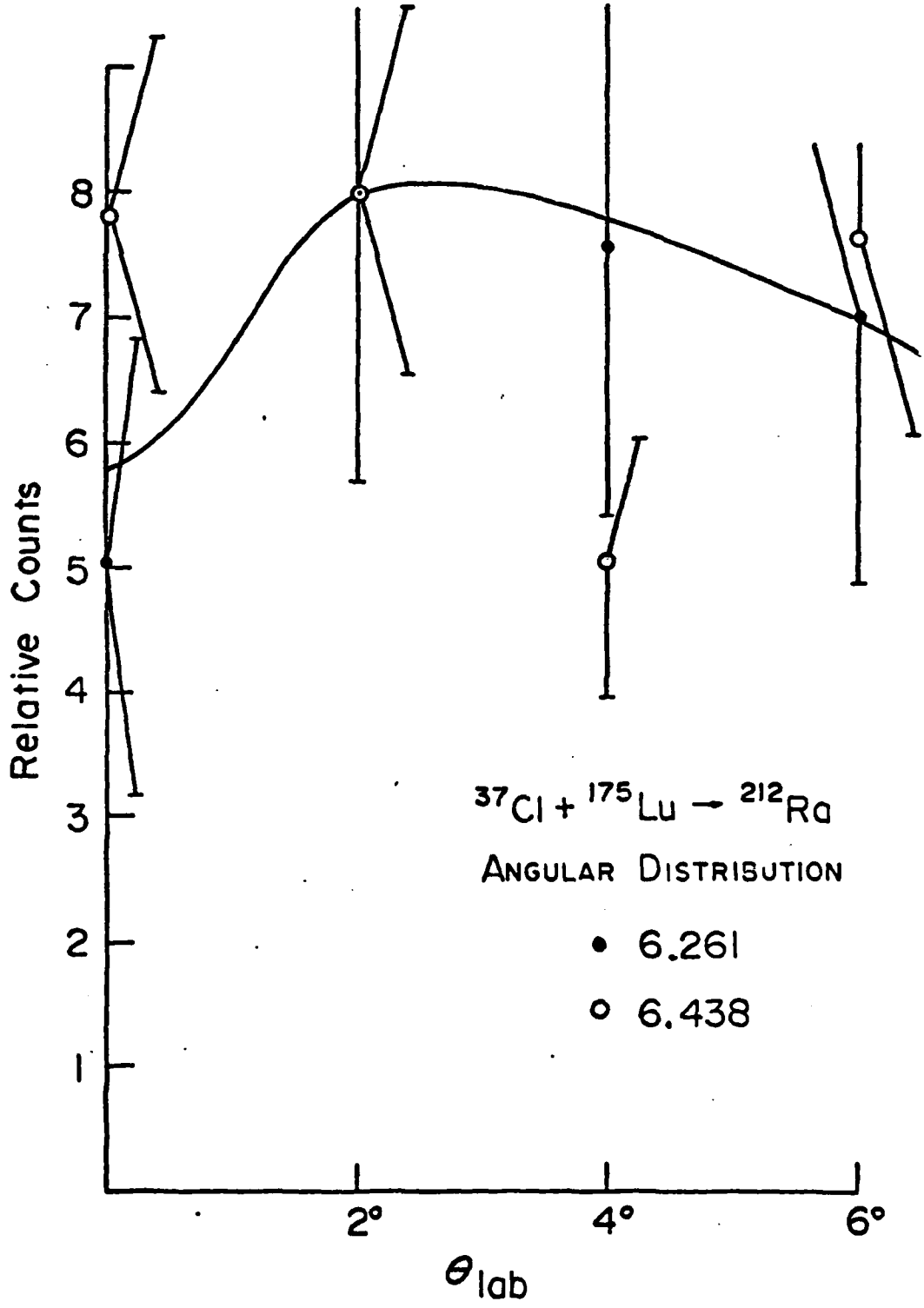
Relative Counts
8
7
6
5
4
3
2
1
2°
4°
6°
θlab
37Cl + 175Lu → 212Ra
Angular Distribution
• 6.261
o 6.438

FIGURE 35

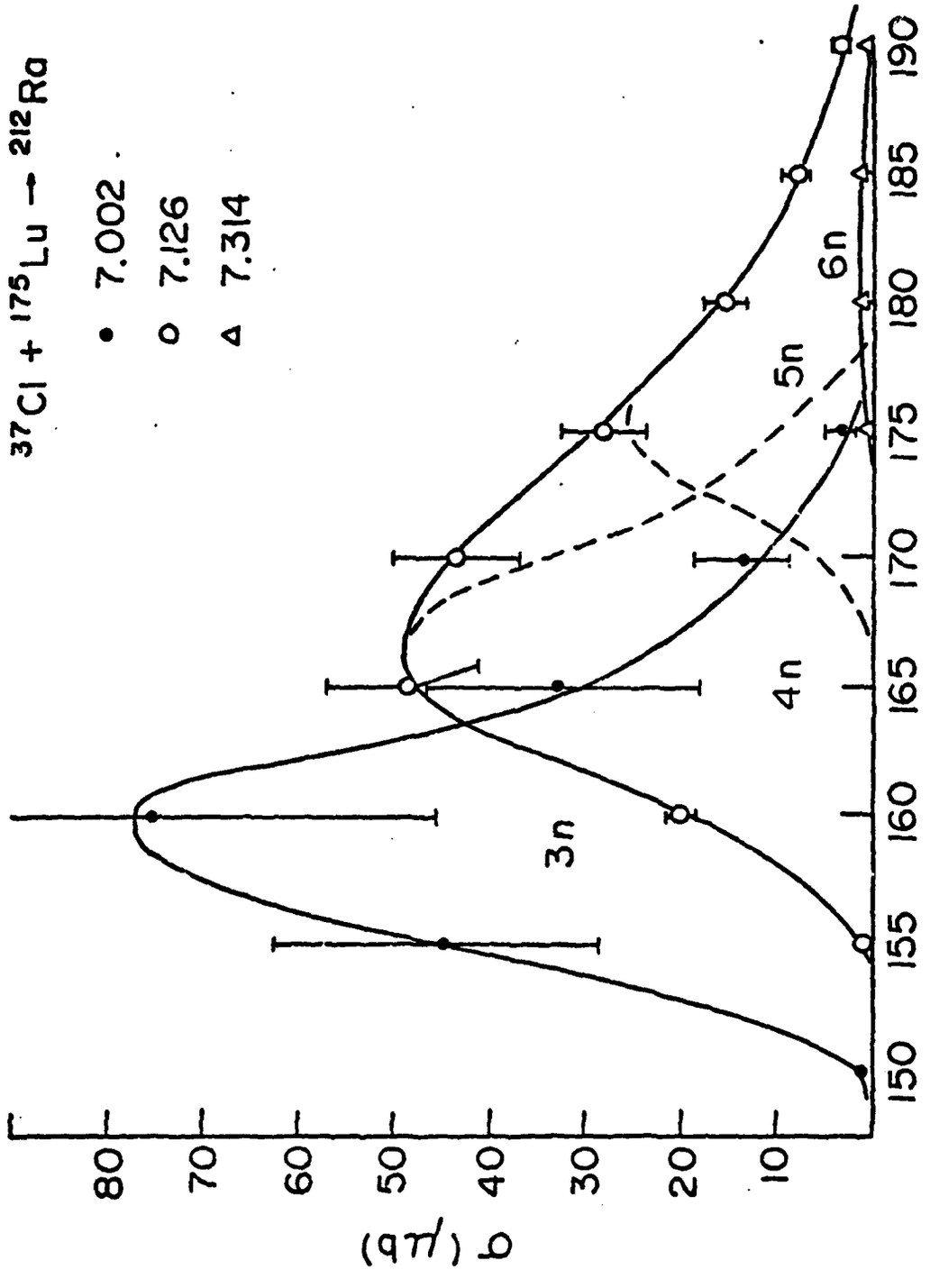
$^{37}Cl + ^{175}Lu \rightarrow ^{212}Ra$
• 7.002
o 7.126
Δ 7.314
3n
4n
5n
6n
σ (μb)
E BEAM (MeV)
80
70
60
50
40
30
20
10
150
155
160
165
170
175
180
185
190

FIGURE 36

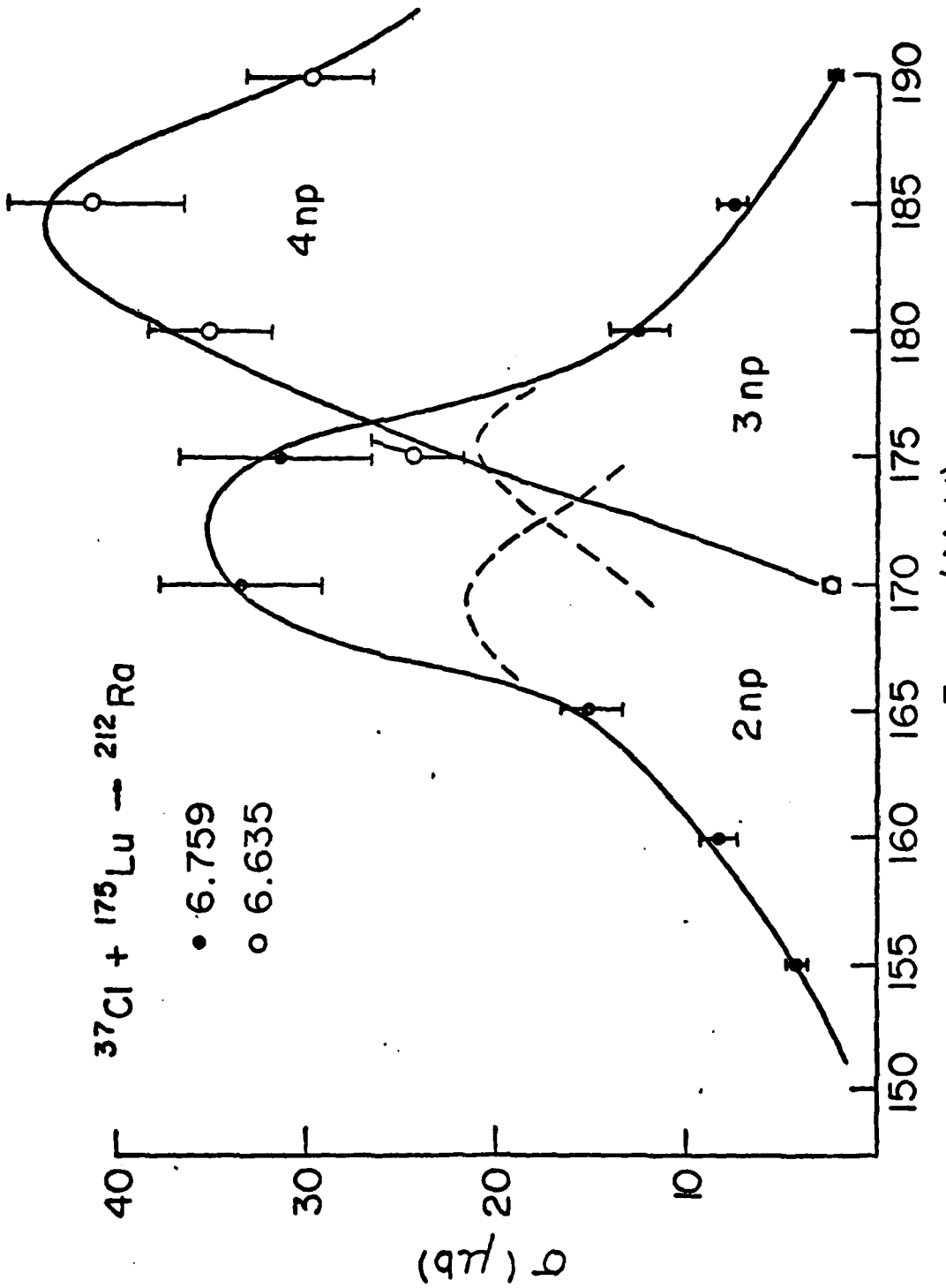
$^{37}Cl + ^{175}Lu \rightarrow ^{212}Ra$
• 6.759
o 6.635
4np
3np
2np
σ (μb)
40
30
20
10
150
155
160
165
170
175
180
185
190
E BEAM (MeV)

FIGURE 37

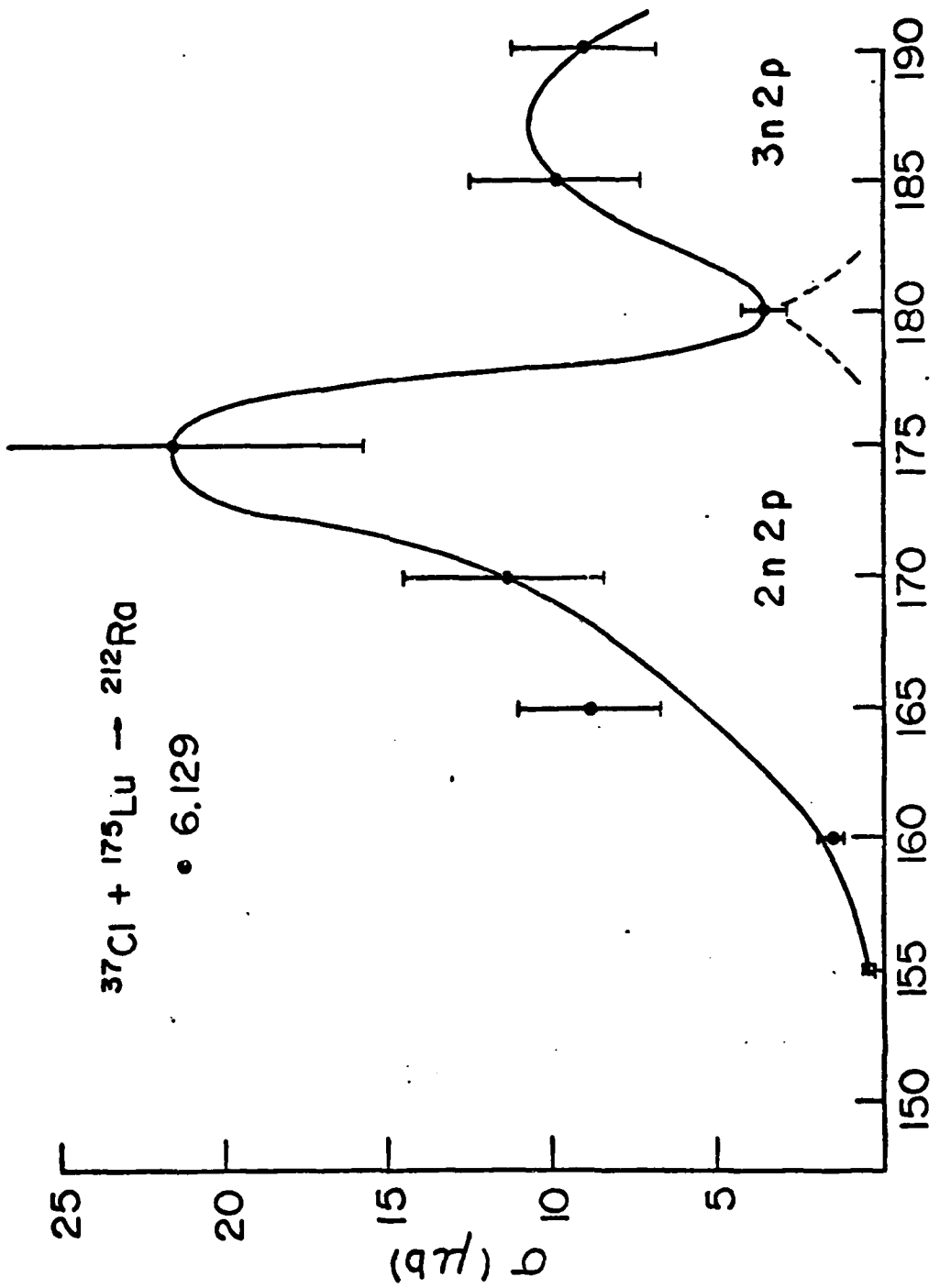
$^{37}Cl + ^{175}Lu \rightarrow ^{212}Ra$
• 6.129
2n 2p
3n 2p
σ (μb)
25
20
15
10
5
150
155
160
165
170
175
180
185
190
E_{BEAM} (MeV)

FIGURE 3A

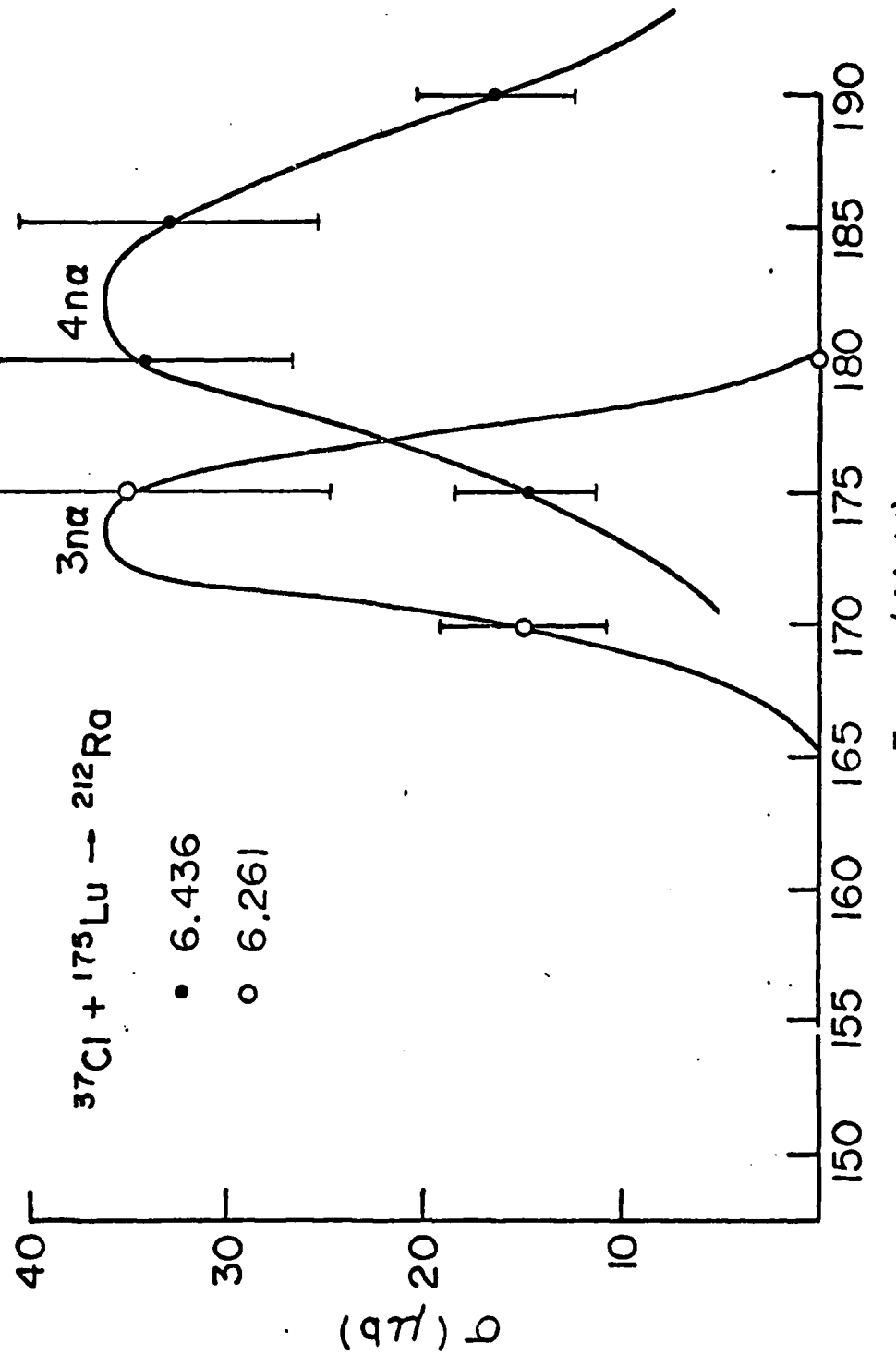
$^{37}Cl + ^{175}Lu \rightarrow ^{212}Ra$
• 6.436
o 6.261
3nα
4nα
σ (μb)
40
30
20
10
150
155
160
165
170
175
180
185
190
E_{BEAM} (MeV)

FIGURE 39

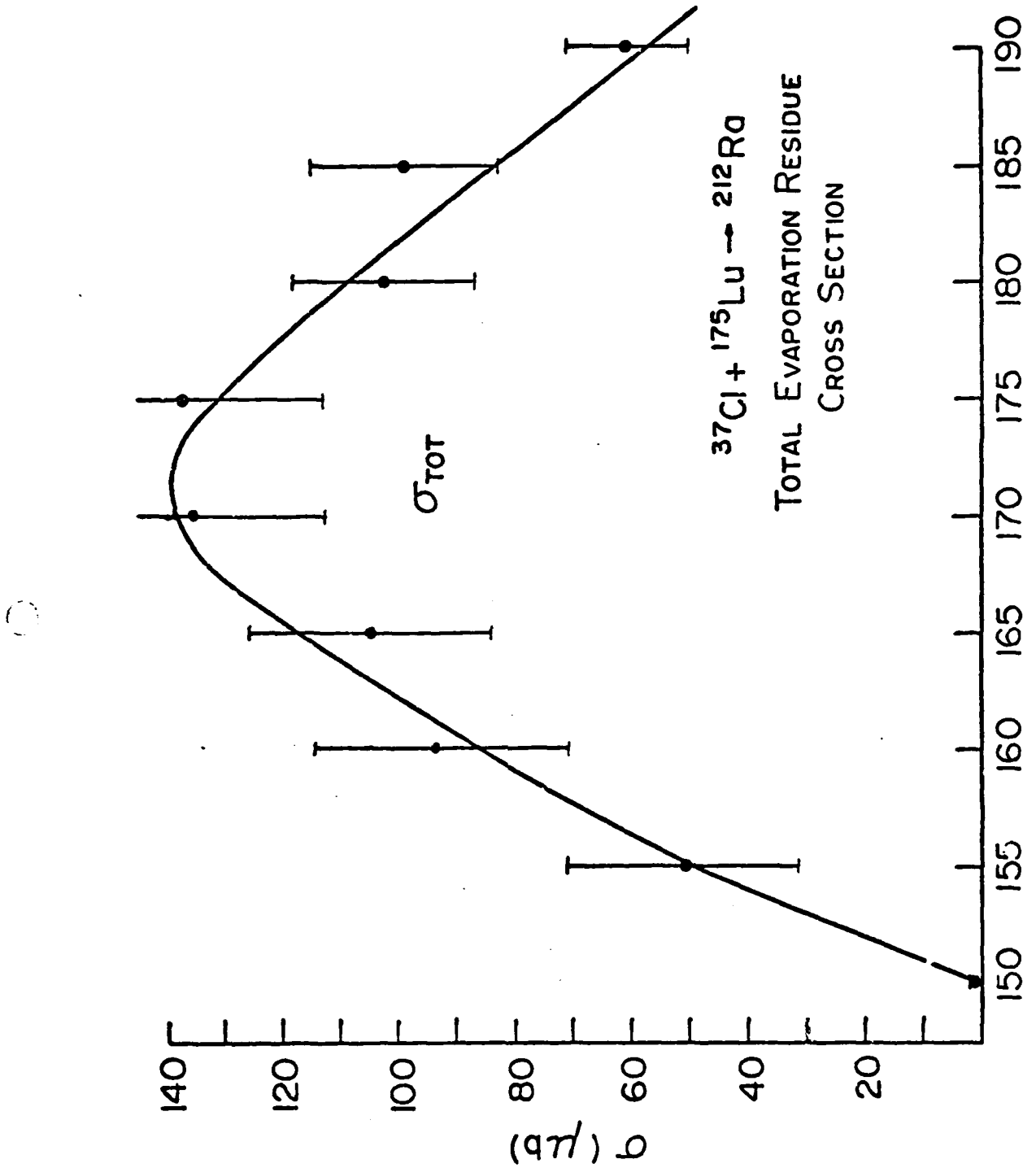
$^{37}Cl + ^{175}Lu \rightarrow ^{212}Ra$
Total Evaporation Residue
Cross Section
σ_{TOT}
σ (μb)
140
120
100
80
60
40
20
150
155
160
165
170
175
180
185
190
E_{BEAM} (MeV)

FIGURE 40

TABLE IV

Absolute Cross Sections (in μb) for $^{37}Cl + ^{175}Lu$

E_{Lab}(MeV) / E_α(MeV)	150	155	160	165	170	175	180	185	190
3n2p/2n2p 6.129		.5 ±.1	1.8 ±.3	8.5 ±2.3	11.5 ±3.0	21.5 ±5.7	3.5 ±.8	9.8 ±2.5	9.0 ±2.3
2np/3np 6.635		4.3 ±.5	8.5 ±1.1	15.2 ±1.9	33.1 ±4.2	31.4 ±4.1	12.4 ±1.6	8.1 ±1.1	2.2 ±.3
4np 6.159					2.2 ±.2	24.4 ±2.5	35.3 ±3.5	41.1 ±4.1	29.7 ±3.0
3n 7.002	.72 ±.6	37.7 ±16.4	62.2 ±27.0	27.1 ±11.8	11.5 ±5.0	2.4 ±1.0	.9 ±.4		
4n/5n 7.126		1.0 ±.1	20.3 ±1.6	48.0 ±3.9	43.7 ±3.6	27.8 ±2.3	15.8 ±1.3	7.8 ±.6	.3 ±.2
6n 7.314						.6 ±.2	.8 ±.3	.8 ±.3	.2 ±.1
3nα* 6.261					34.9 ±10.3	14.8 ±4.4			
4nα 6.436						14.7 ±3.6	34.2 ±8.4	32.8 ±8.1	16.4 ±4.0
σ_{TOT}	.72 ±.6	43.5 ±17.1	92.5 ±30.0	99.1 ±19.9	136.9 ±26.3	137.0 ±23.6	102.2 ±16.0	99.6 ±16.4	60.3 ±9.8

*The reported cross section is 10% of the calculated midpoint. This was done due to the large error introduced in integrating over the angular distribution.

D. $^{37}Cl + ^{181}Ta$ and $^{37}Cl + ^{186}W$

These two reactions are considered together since their Z^2/A values are very similar and since the tungsten data is less than complete. Once again in this region several of the evaporation residues had similar alpha decay energies. These are noted by dashed lines in figures 44 to 46. Tungsten excitation functions appear in figures 50 and 51. Angular distributions for the tantalum appear in figures 41 to 43. Angular distributions for the tungsten data scaled to the $^{37}Cl + ^{169}Tm$ shape, appear in figures 48 and 49. Tables V and VI show the individual cross sections for the two reactions and total evaporation residue functions appear in figures 47 and 52.

Both the tantalum and the tungsten reactions were of such low cross section that the detection system was severely tested. Only through the use of the anticoincidence counter could evaporation residues with such low cross sections be observed (in some cases as low as 12 nanobarns). Alpha evaporations begin to dominate in this region. The increased excitation of the nucleus is more easily dissipated through the evaporation of an alpha particle rather than a neutron. The tungsten reaction displayed many problems that will surely be present in future experiments at higher Z. In many instances the half lives for alpha decay of the evaporation residues were of the order of one microsecond. This allowed the compound nucleus to evaporate and then for the evaporation residue to decay before striking the detector. Due to the time constraints and a low count rate, no angular distribution was obtained in the tungsten reaction. To

facilitate the determination of an absolute cross section, the angular distributions of similar evaporation residues in the $^{37}Cl + ^{169}Tm$ reaction were used. Excitation functions of the short lived (less than 1.5 microsecond) evaporation residues are those of their respective daughter functions (4n and 5n), since as shown in the $^{37}Cl + ^{169}Tm$ reaction, parent and daughter functions exhibit identical excitation functions (after correction for alpha branching ratios less then 1.0).

The tungsten reaction exhibits many anomalies compared to the four other reactions studied. In all other reactions the odd-even chlorine beams fused with odd-even targets. In the tungsten case the target is even-even, however. Utilizing these shell effects, the ALICE code has predicted higher cross sections for the tungsten reaction in all parameter sets. (See Figure 54.) Experimentally, there is no reason to believe that the peak cross section was obtained, since the total evaporation residue cross section function is just beginning its steep climb. (See Figure 52.) There is also doubt as to the identification of the individual residues. This has a drastic effect on cross section determination if a misjudgement is made between a neutron and an alpha evaporation. As mentioned previously, only a detailed velocity and/or angular distribution can differentiate the two. Due to time constraints, this was not accomplished. The oddities presented, the l value dependence, the large 3nα evaporation, the peak cross section occurring at a much higher lab energy as well as the problems of short half life for the parent residues and the paucity of data on the Protactinium line, make this a good candidate

to pursue further in heavy ion reaction studies. The use of ^{183}W as a target, although difficult to obtain, would assist in determining the extent of the shell effects in the stability of the heavy compound nuclei. While the data is insufficient at this time, the increased cross section at equal Z^2/A for odd-even compound nuclei versus even-even compound systems may prove significant in the search for heavier systems.

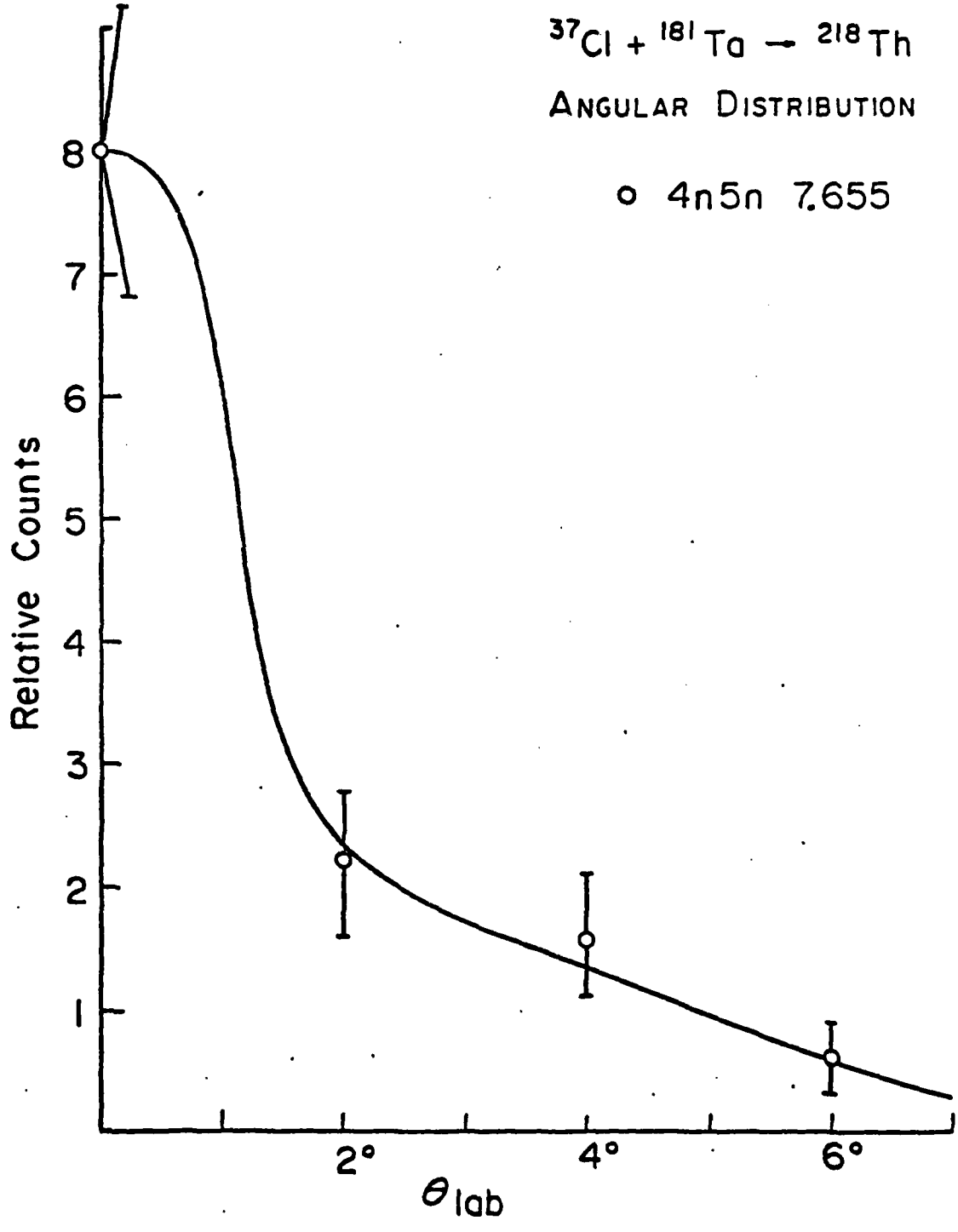
$^{37}Cl + ^{181}Ta \rightarrow ^{218}Th$
ANGULAR DISTRIBUTION
o 4n5n 7.655
Relative Counts
8
7
6
5
4
3
2
1
2°
4°
6°
θ_{lab}

FIGURE 41

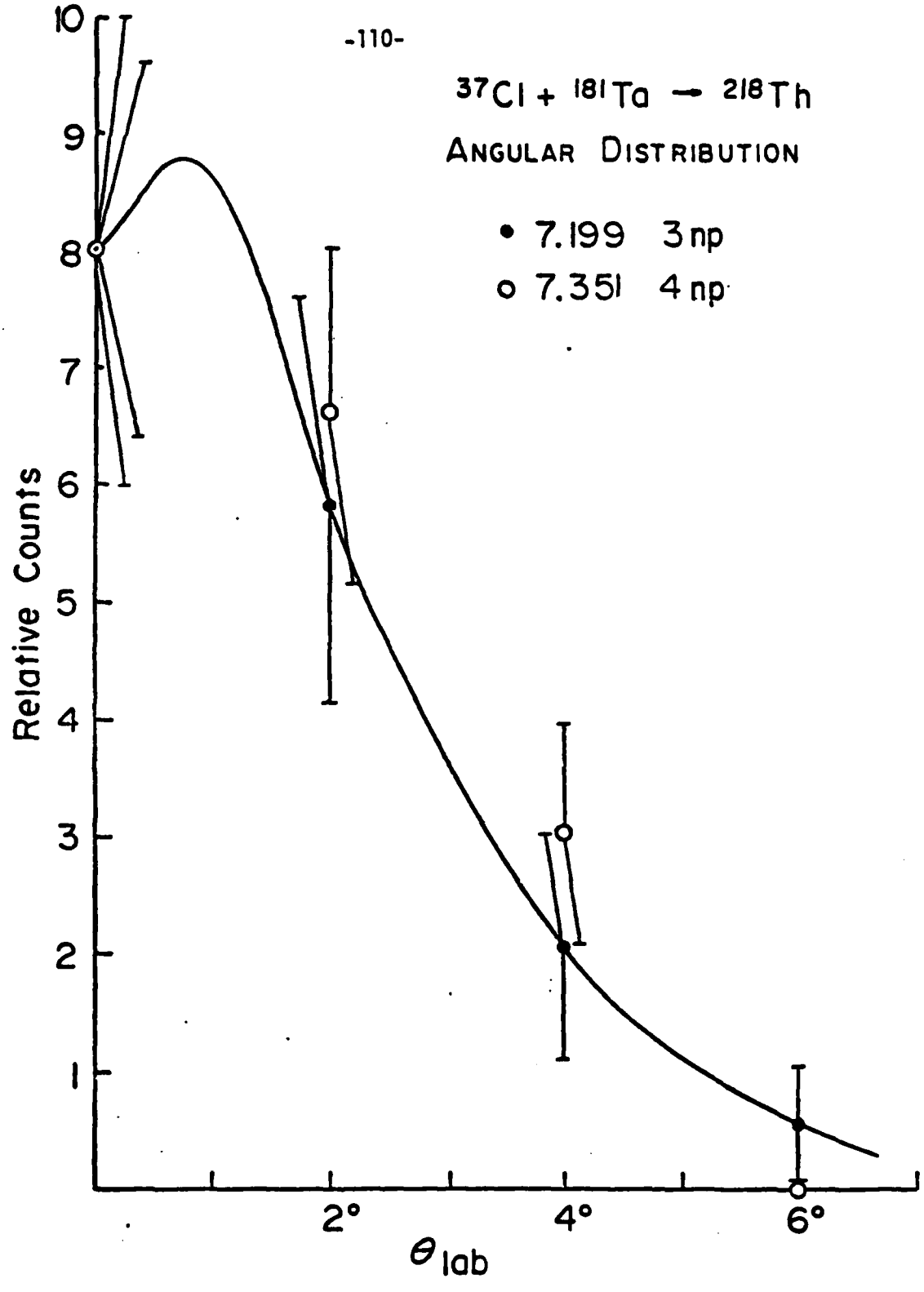
$^{37}Cl + ^{181}Ta \rightarrow ^{218}Th$
ANGULAR DISTRIBUTION
• 7.199 3np
o 7.351 4np
Relative Counts
10
9
8
7
6
5
4
3
2
1
2°
4°
6°
θ_{lab}

FIGURE 42

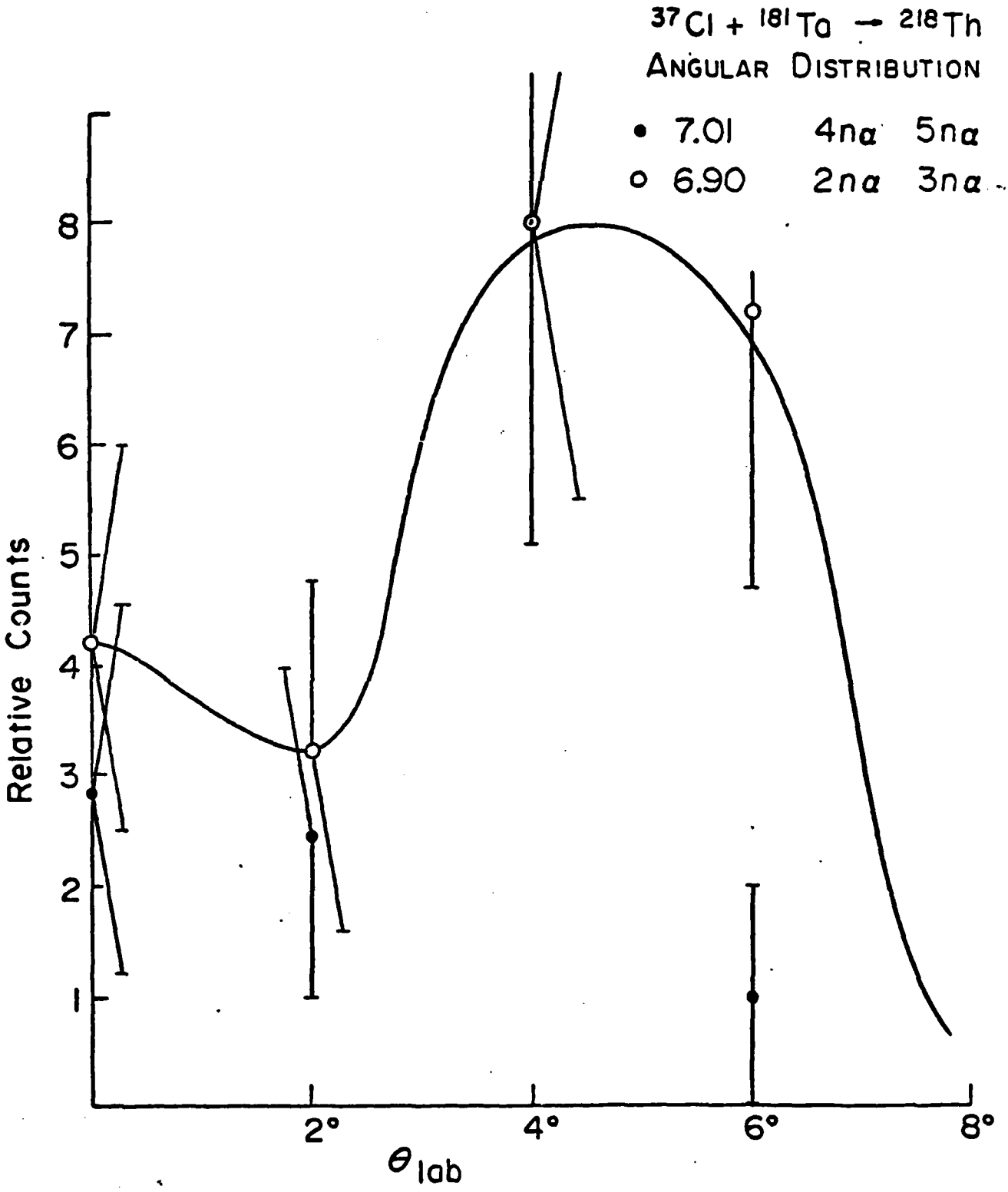
$^{37}Cl + ^{181}Ta \rightarrow ^{218}Th$
Angular Distribution
• 7.01 4nα 5nα
○ 6.90 2nα 3nα
Relative Counts
1
2
3
4
5
6
7
8
2°
4°
6°
8°
θlab

FIGURE 43

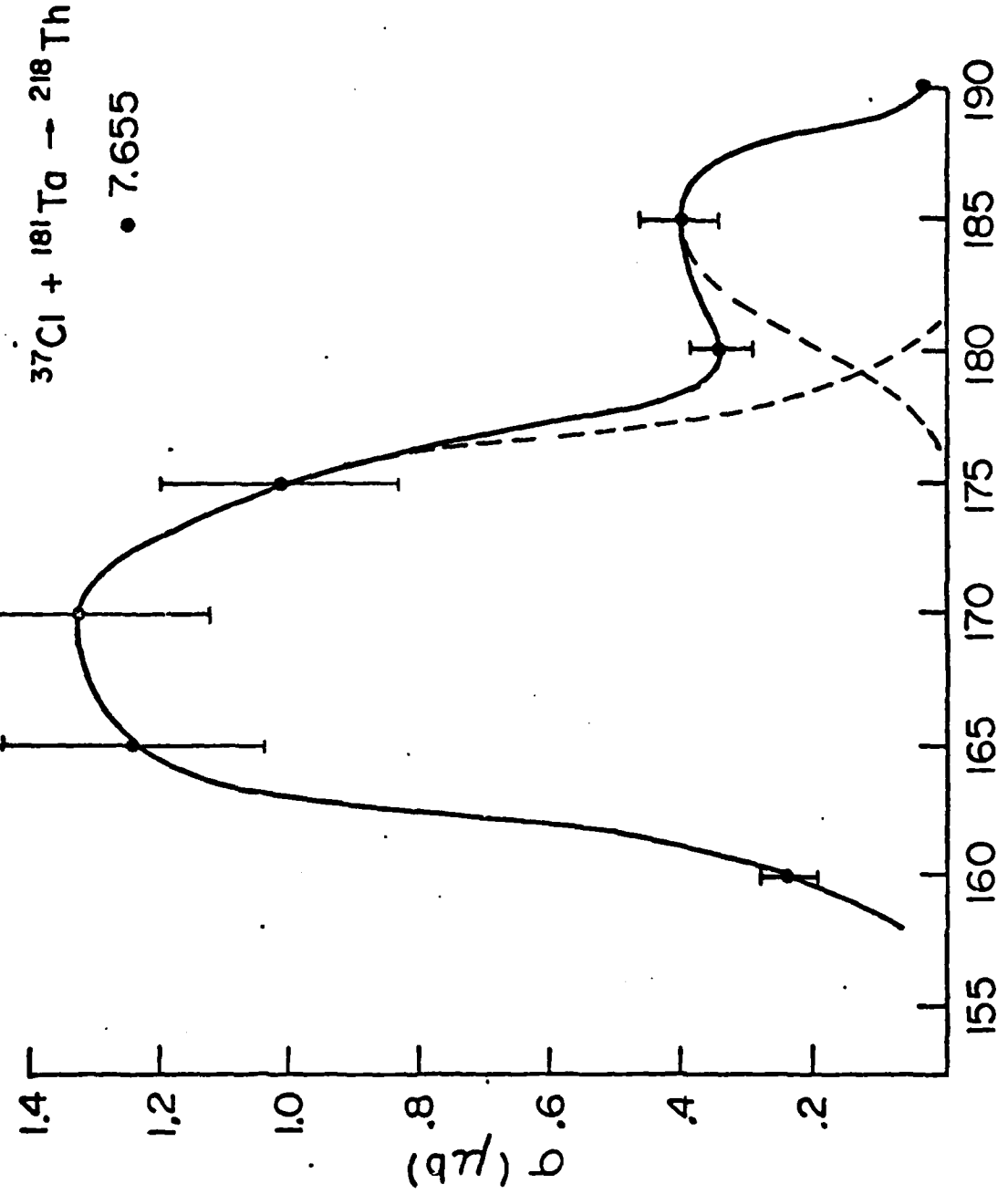
$^{37}Cl + ^{181}Ta \rightarrow ^{218}Th$
• 7.655
σ (μb)
1.4
1.2
1.0
.8
.6
.4
.2
155
160
165
170
175
180
185
190
E_{BEAM} (MeV)

FIGURE 44

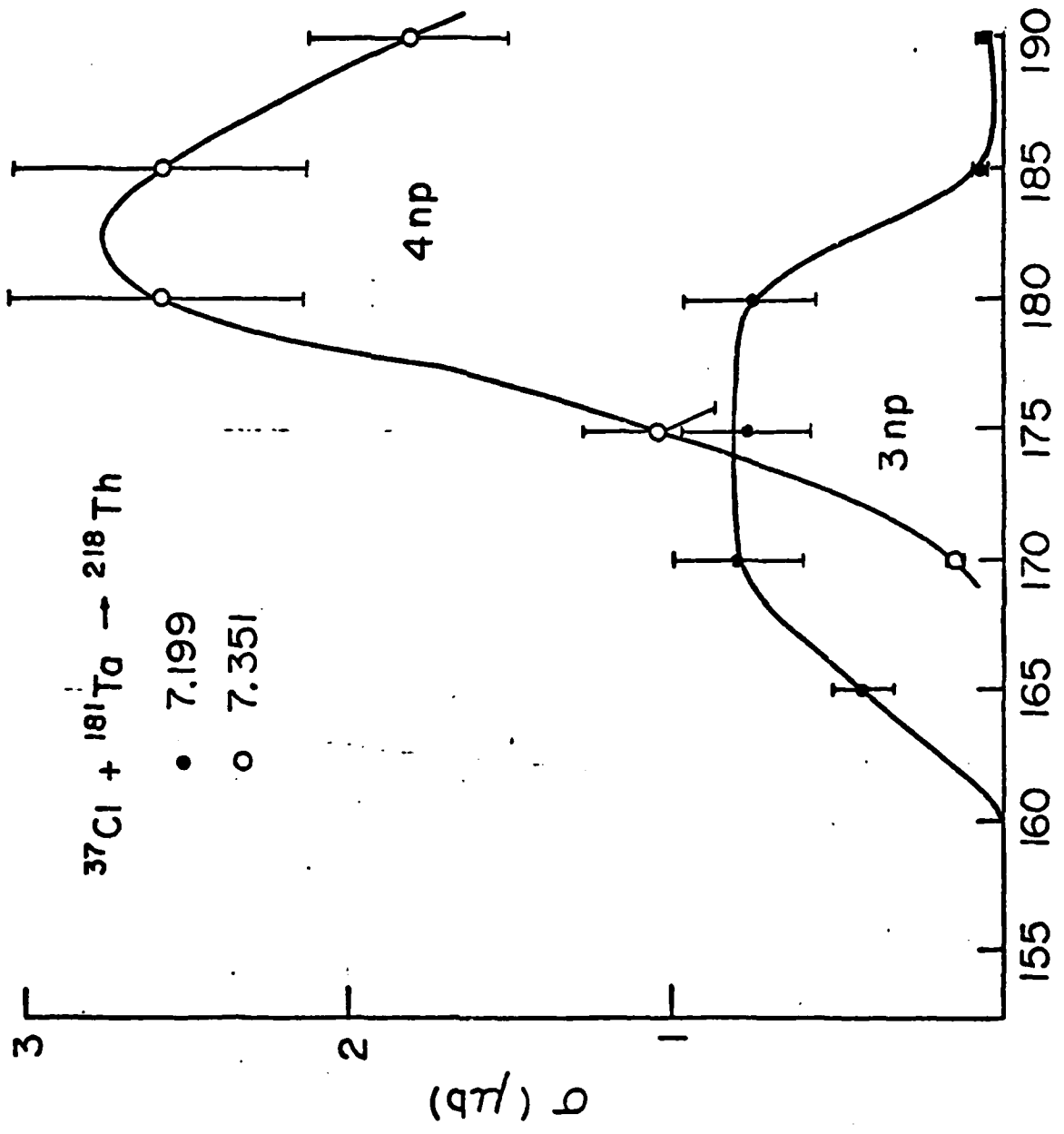
$^{37}Cl + ^{181}Ta \rightarrow ^{218}Th$
• 7.199
o 7.351
4np
3np
σ (μb)
3
2
1
155
160
165
170
175
180
185
190
E_{BEAM} (MeV)

FIGURE 45

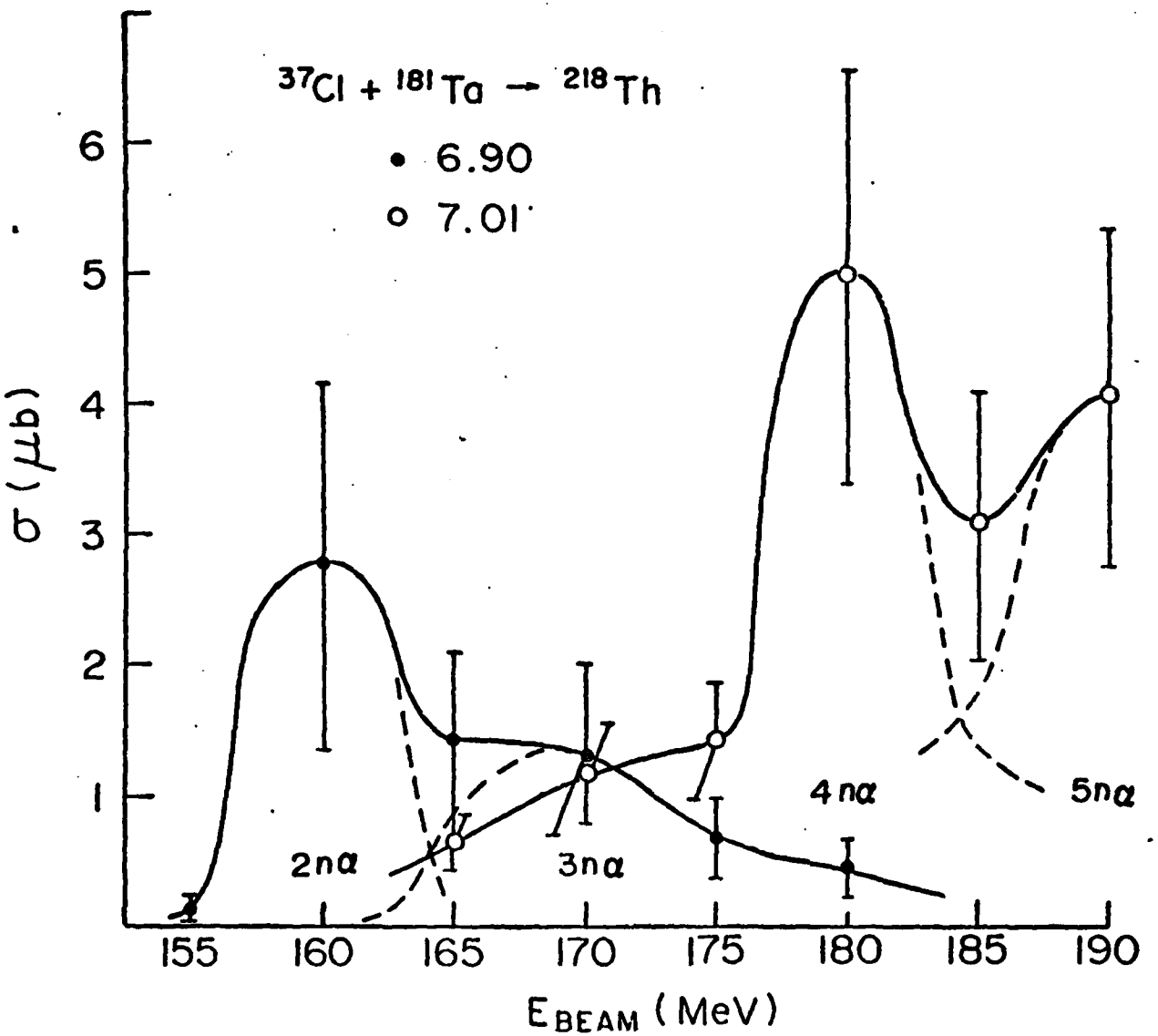
$^{37}Cl + ^{181}Ta \rightarrow ^{218}Th$
• 6.90
o 7.01
σ (μb)
6
5
4
3
2
1
2nα
3nα
4nα
5nα
155
160
165
170
175
180
185
190
E BEAM (MeV)

FIGURE 46

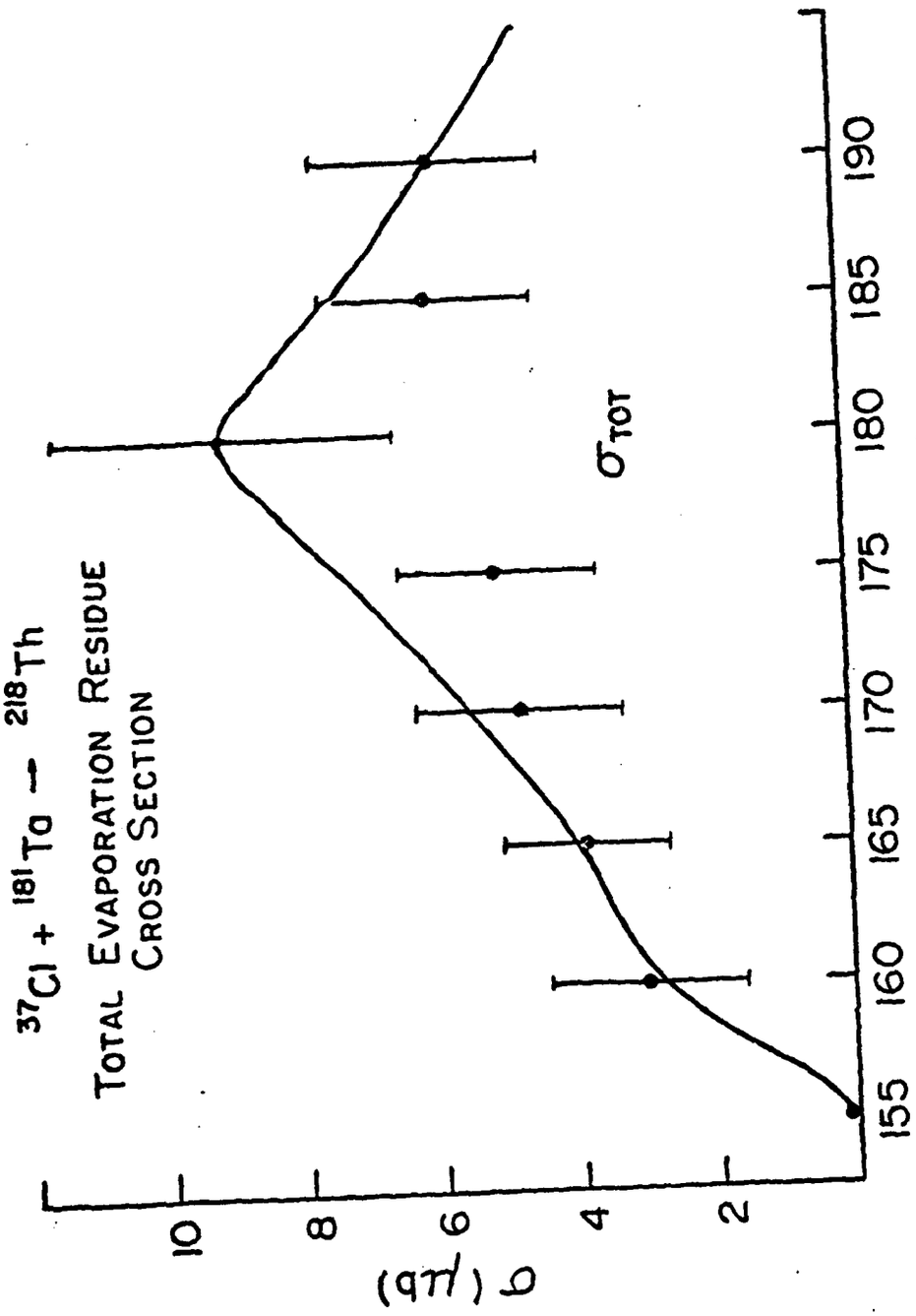
$^{37}Cl + ^{181}Ta \rightarrow ^{218}Th$
Total Evaporation Residue
Cross Section
σ_{TOT}
σ (μb)
10
8
6
4
2
155
160
165
170
175
180
185
190
E_{BEAM} (MeV)

FIGURE 47

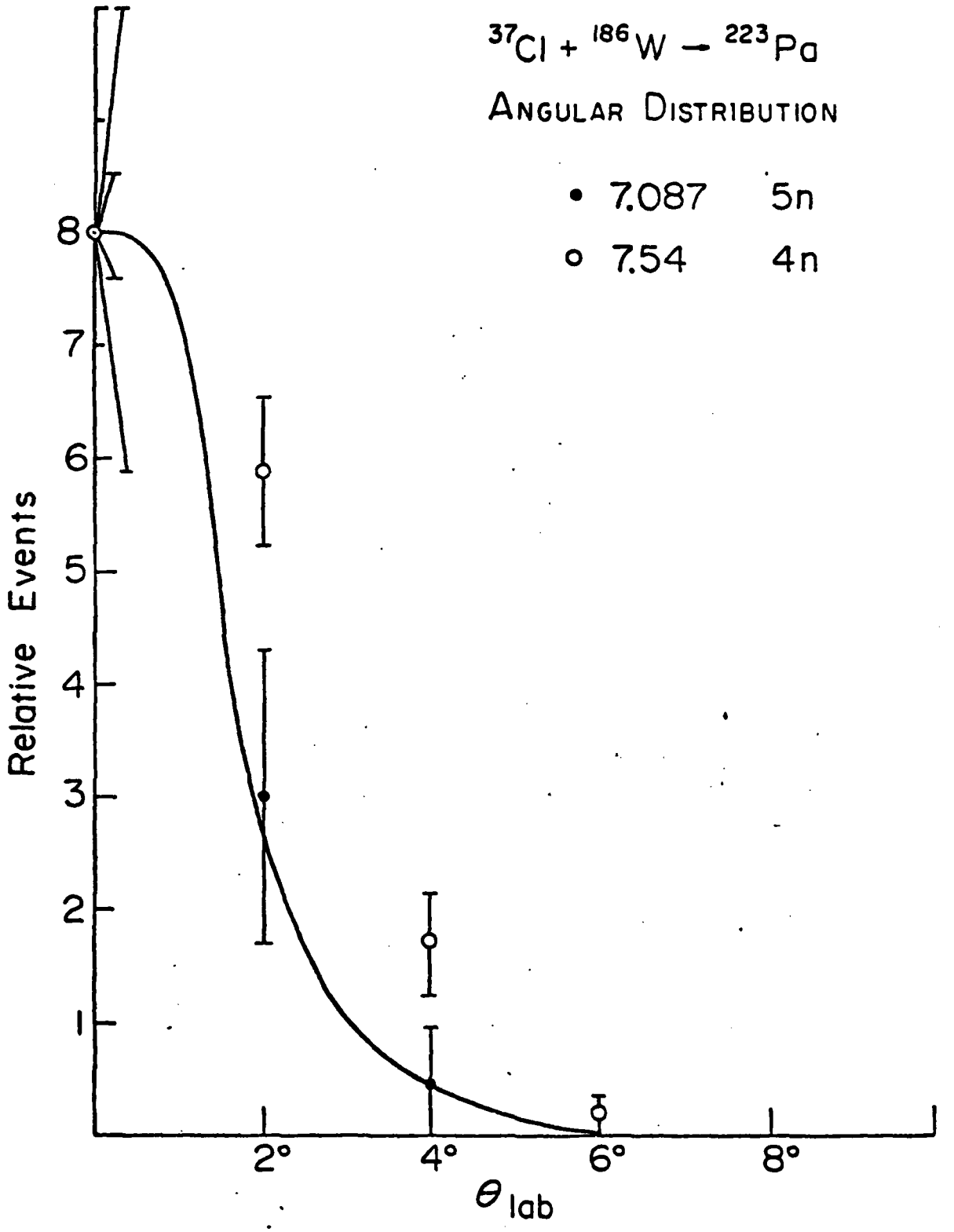
$^{37}Cl + ^{186}W \rightarrow ^{223}Pa$
Angular Distribution
• 7.087 5n
o 7.54 4n
Relative Events
1
2
3
4
5
6
7
8
2°
4°
6°
8°
θ lab

FIGURE 48

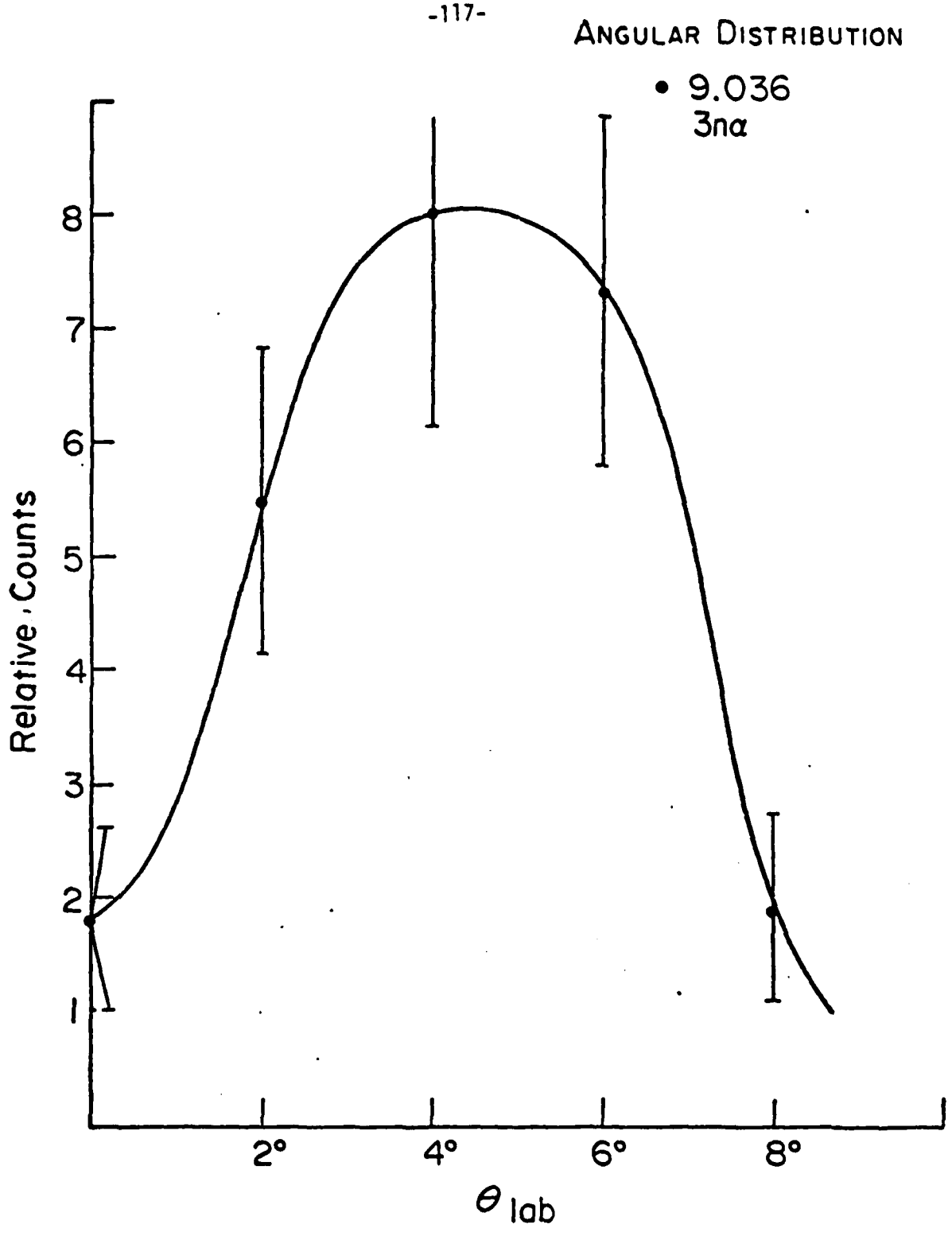
ANGULAR DISTRIBUTION
• 9.036
3nα
Relative Counts
1
2
3
4
5
6
7
8
2°
4°
6°
8°
θ lab

FIGURE 49

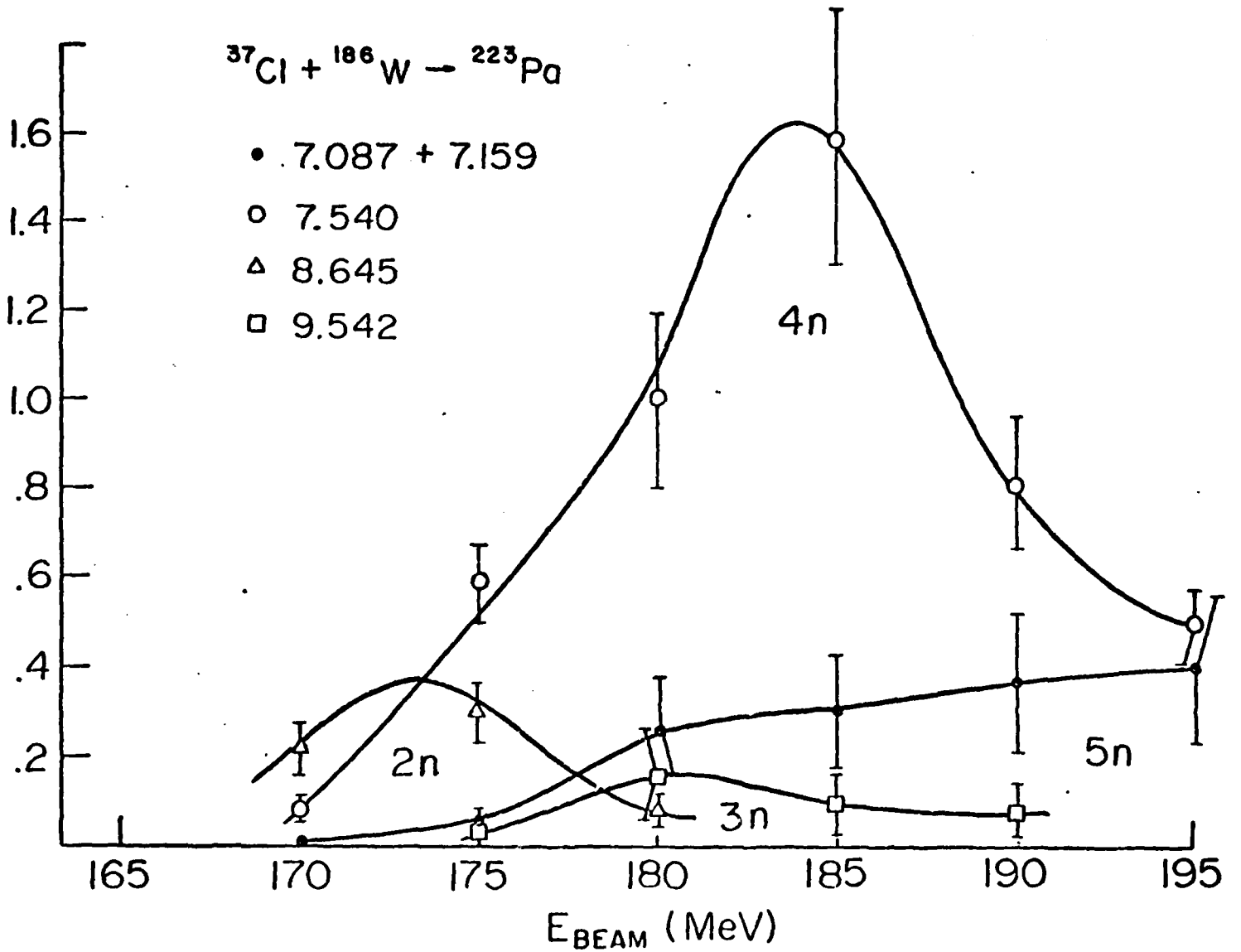
$^{37}Cl + ^{186}W \rightarrow ^{223}Pa$
• 7.087 + 7.159
o 7.540
Δ 8.645
□ 9.542
4n
2n
3n
5n
1.6
1.4
1.2
1.0
.8
.6
.4
.2
165
170
175
180
185
190
195
E_{BEAM} (MeV)

FIGURE 50

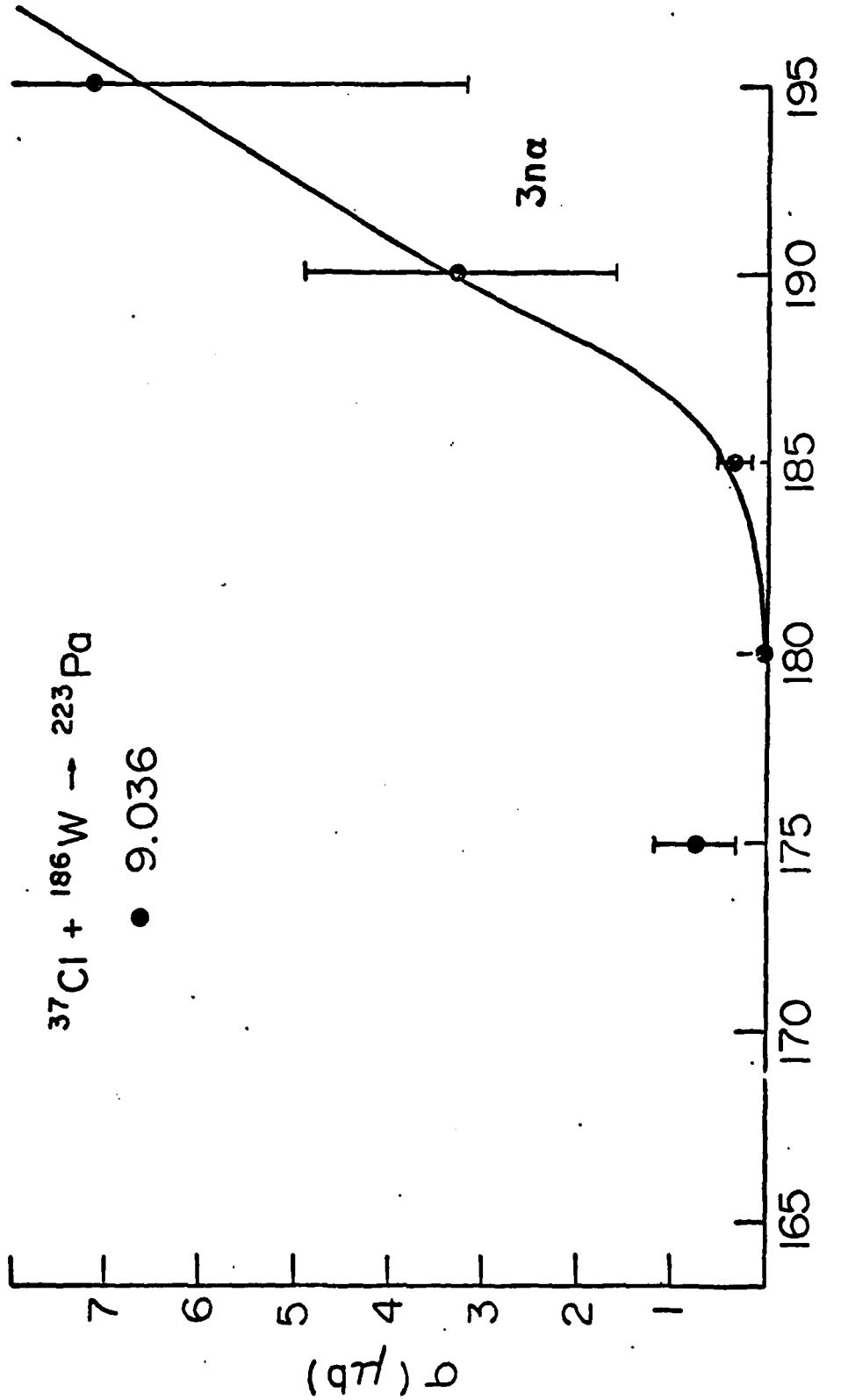
$^{37}Cl + ^{186}W \rightarrow ^{223}Pa$
● 9.036
3nα
σ (μb)
1
2
3
4
5
6
7
165
170
175
180
185
190
195

FIGURE 51

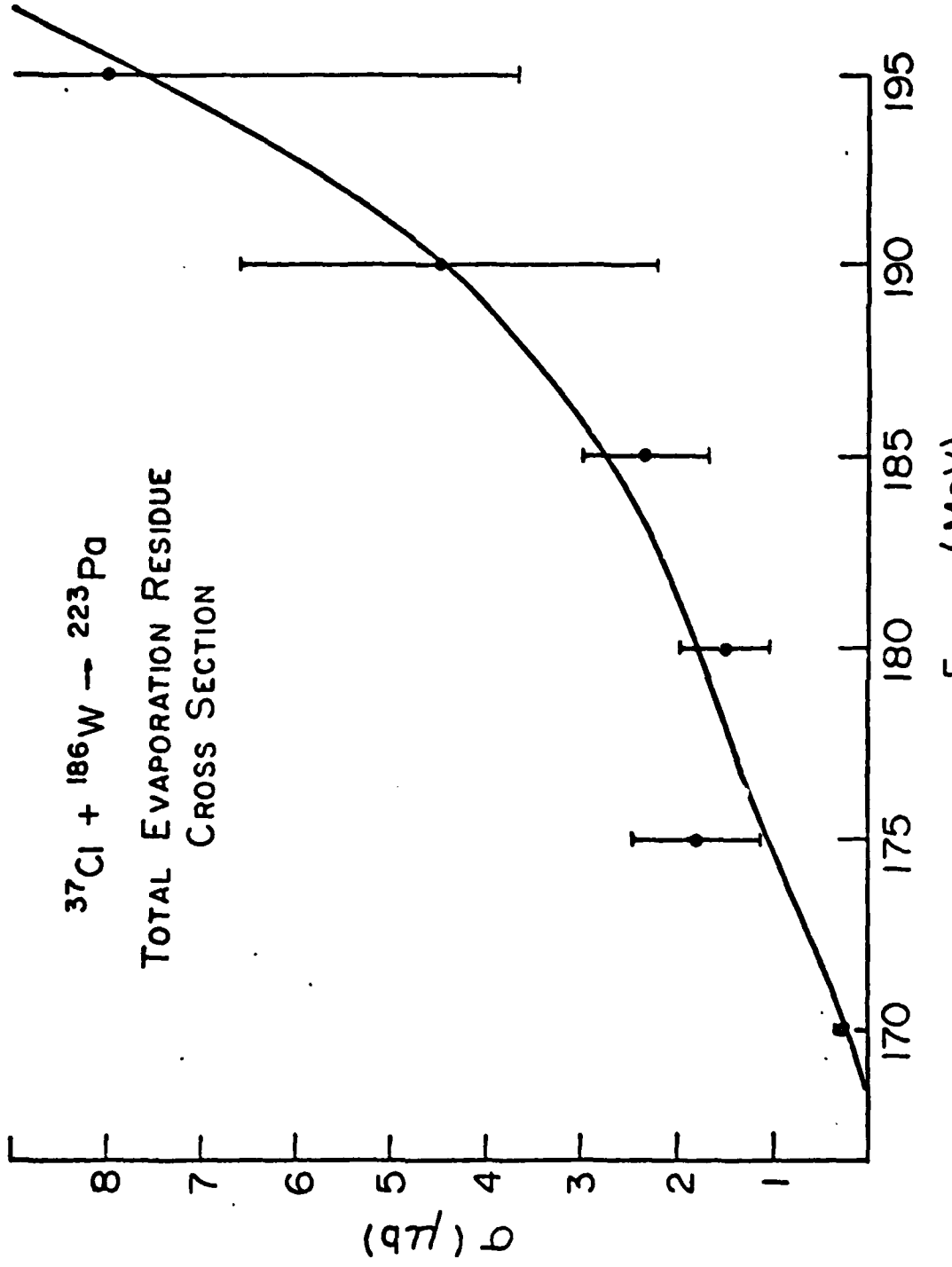
$^{37}Cl + ^{186}W \rightarrow ^{223}Pa$
Total Evaporation Residue
Cross Section
σ (μb)
1
2
3
4
5
6
7
8
170
175
180
185
190
195
E BEAM (MeV)

FIGURE 52

TABLE V

Absolute Cross Sections (in μb) for $^{37}Cl + ^{181}Ta$

E_{Lab}(MeV) / E_α(MeV)	155	160	165	170	175	180	185	190
4n/5n 7.655		.23 ±.04	1.24 ±.20	1.32 ±.21	1.11 ±.18	.34 ±.05	.40 ±.06	.03 ±.00
2nα/3nα 6.899	.12 ±.06	2.76 ±1.39	1.43 ±.72	1.31 ±.66	.66 ±.33	.39 ±.20		
4nα/5nα 7.01			.67 ±.22	1.16 ±.39	1.41 ±.47	4.98 ±1.66	3.05 ±1.02	4.03 ±1.34
3np 7.199			.42 ±.11	.80 ±.20	.78 ±.20	.77 ±.20	.07 ±.02	.06 ±.02
4np 7.351				.14 ±.02	1.15 ±.20	2.58 ±.45	2.57 ±.45	1.81 ±.3
σ_{TOT}	.12 ±.06	2.99 ±1.44	3.76 ±1.25	4.73 ±1.48	5.11 ±1.38	9.06 ±2.56	6.09 ±1.55	5.93 ±1.67

TABLE VI

Absolute Cross Sections (in μb) for $^{37}Cl + ^{186}W$

E_{Lab} (MeV) / E_α (MeV)	170	175	180	185	190	195
5n(α) 7.087	.010 ±.003	.050 ±.017	.034 ±.011	.094 ±.031	.125 ±.042	.177 ±.059
5n(α) 7.159	.012 ±.005	.016 ±.007	.227 ±.102	.231 ±.103	.244 ±.109	.225 ±.101
4n(α) 7.540	.071 ±.013	.590 ±.106	1.028 ±.185	1.580 ±.284	.826 ±.149	.508 ±.091
3n 9.542		.044 ±.025	.152 ±.088	.098 ±.057	.091 ±.052	
2n 8.645	.228 ±.055	.302 ±.073	.075 ±.018			
3nα 9.036		.784 ±.453		.345 ±.200	3.261 ±1.880	7.134 ±4.12
σ_{TOT}	.32 ±.08	1.78 ±.68	1.54 ±.40	2.35 ±.68	4.55 ±2.23	8.04 ±4.37

CHAPTER V

RESULTS AND CONCLUSIONS

Figure 53 shows the relationship between the Z^2/A value of the compound nucleus and the peak absolute cross sections of evaporation residue formation of the five reactions (see Table VII). The reaction cross sections fall drastically. For every .5 increase in Z^2/A there is an order of magnitude drop in the amount of compound nuclei that survive fission. Each point in the figure represents the peak reaction cross section. The peak value is used since it was found that the relationship between σ and Z^2/A is somewhat insensitive to the effect of compound nucleus excitation energy given this series of reactions with similar beams. In this series of reactions all of the peaks occurred within a small bracket of excitation energy. This drastic crop in cross section can not continue if more heavy, or superheavy, nuclei are to be studied. The use of chlorine as a projectile imparts a high excitation energy to the compound nucleus and a choice of an ion beam at the $A_{cn}/4$ level may reverse this trend. There must be a sufficient beam current however, and these are not yet available in present systems.

A regression analysis performed on the experimental σ vs. Z^2/A function resulted in the following function:

$$\ln \sigma = 161.65 - 4.293\ Z^2/A$$

whose "f" value (the measure of the reliability of the hypothetical linear relationship) is very significant (99.5% reliable).

In the conduct of the experiments of this study, several new isotopes were discovered. In the $^{35}Cl + ^{169}Tm$ reaction, the new isotopes ^{199}Rn and ^{199m}Rn were found to have alpha decay energies of 6.99 and 7.06 MeV, respectively.

In order to predict the best combination of projectile and target nucleus to use in forming a compound system that survives fission to a measurable extent, a satisfactory set of parameters must be obtained for statistical evaporation codes. The code ALICE has been applied to the five reactions in this study to determine a useable parameter set in order to predict future reactions. Several parameter sets were tried at a constant excitation of the compound nucleus and these appear in figure 54 and Table I. The parameter CLD (the ratio of single particle level densities $a_{fission}/a_{neutron}$) is by far the most sensitive of all ALICE inputs. The best fit found was with CLD set to 1.03. This continues the trend announced by Beckerman and Blann (see Table VIII) that determined the adequacy of CLD = 1.03 for lighter systems. This particular ALICE study concentrated only on the total evaporation residue cross section. Individual evaporation channels do not match experimental values well. Neutron evaporations are very supressed and alpha evaporations do not occur at appropriate lab energies. Xnp evaporation modes are accurate however. Also, the ALICE code predicts several modes that are seldom seen in heavy ion reactions (i.e. 3pln). ALICE can also be used to generate the ℓ-crit

TABLE VII

Peak Evaporation Residue Cross Sections vs. Z^2/A

REACTION	Z^2/A	CROSS SECTION (μb)
$^{37}Cl + ^{169}Tm \rightarrow ^{206}Rn$	35.90	1600 ± 300
$^{35}Cl + ^{169}Tm \rightarrow ^{204}Rn$	36.25	487 ± 109
$^{37}Cl + ^{175}Lu \rightarrow ^{212}Ra$	36.50	139 ± 27
$^{37}Cl + ^{181}Ta \rightarrow ^{218}Th$	37.16	9.06 ± 2.55
$^{37}Cl + ^{186}W \rightarrow ^{223}Pa$	37.13	8.04 ± 44

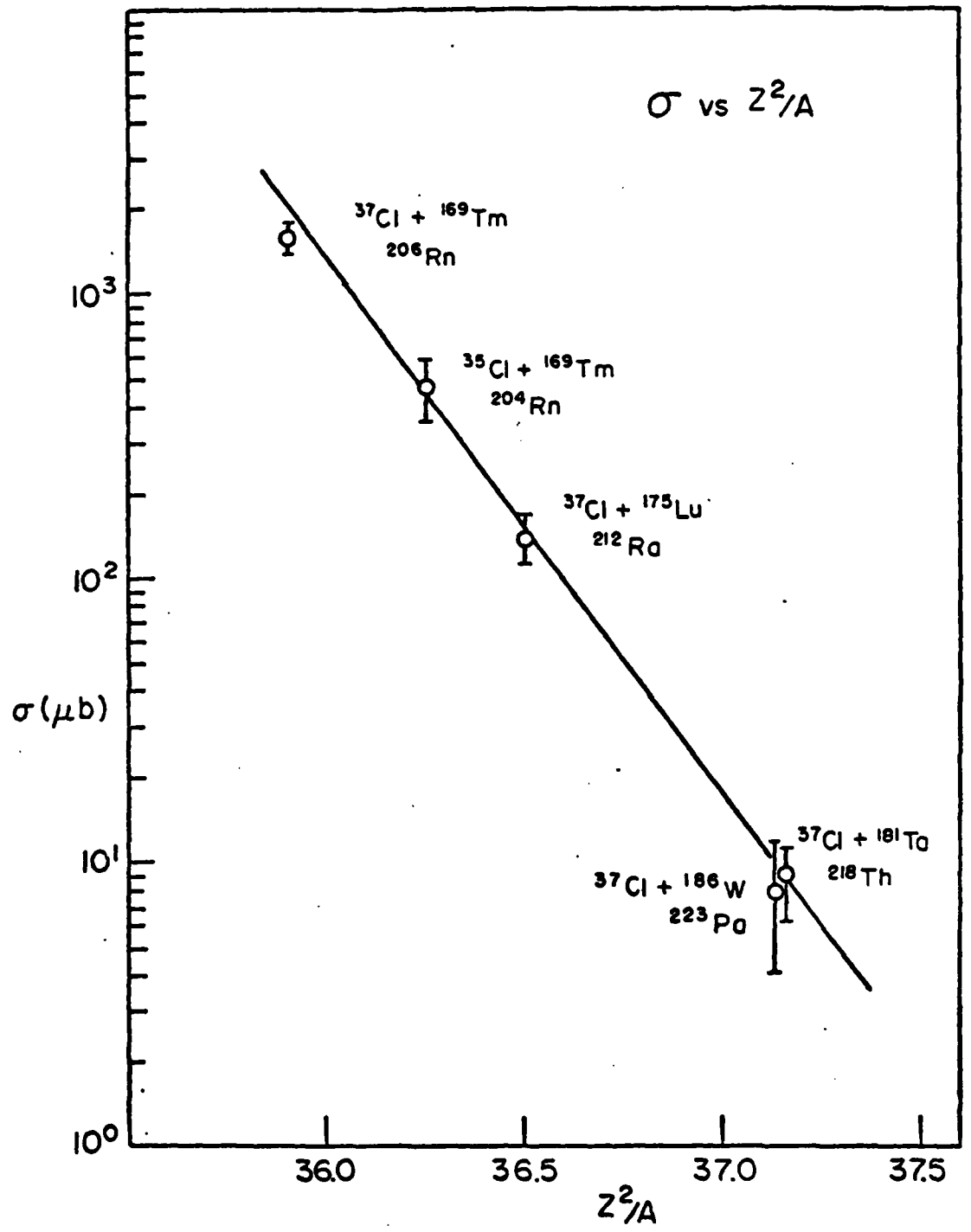
σ vs Z²/A
37Cl + 169Tm
206Rn
35Cl + 169Tm
204Rn
37Cl + 175Lu
212Ra
37Cl + 181Ta
218Th
37Cl + 186W
223Pa
10³
10²
10¹
10⁰
σ(μb)
36.0
36.5
37.0
37.5
Z²/A

FIGURE 5.3

TABLE VIII

Calculated and Measured Evaporation Residue Cross Sections

Target & Projectile	Compound Nucleus	E_{lab} (MeV)	a_f/a_ν	B_f	$\sigma_{calc}(\mu b)$	$\sigma_{exp}(\mu b)$	
$^{58}Ni + ^{40}Ar$	^{98}Pd	288	1.03	.540	6.31×10^5	$(9.00\pm1.2)\times10^5$	*
$^{56}Fe + ^{52}Cr$	^{108}Sn	264	1.03	.450	5.72×10^5	$(5.13\pm.80)\times10^5$	*
$^{58,60}Ni + ^{63}Cu$	$^{121,123}La$	347	1.03	.510	4.13×10^5	$(4.52\pm.60)\times10^5$	*
$^{121}Sb + ^{40}Ar$	^{161}Tm	340	1.00	.676	4.76×10^5	$(5.00\pm.50)\times10^5$	*
$^{107,109}Ag + ^{63}Cu$	$^{170,172}Os$	347	1.03	.635	6.20×10^4	$(5.17\pm1.2)\times10^5$	*
$^{37}Cl + ^{169}Tm$	^{206}Rn	148-186	1.03	.80	1.7×10^3	$(1.6\pm.3)\times10^3$	#
$^{35}Cl + ^{169}Tm$	^{204}Rn	150-185	1.03	.80	1.053×10^3	$(4.87\pm1.09)\times10^2$	#
$^{37}Cl + ^{175}Lu$	^{212}Ra	150-190	1.03	.80	60	$(1.39\pm.27)\times10^2$	#
$^{37}Cl + ^{181}Ta$	^{218}Th	155-190	1.03	.80	5.56	9.06±2.55	#
$^{37}Cl + ^{186}W$	^{223}Pa	170-195	1.03	.80	24.6	8.04±4.4	#

*From Beckerman and Blann, PRC May 1978, p. 1615

#Present work

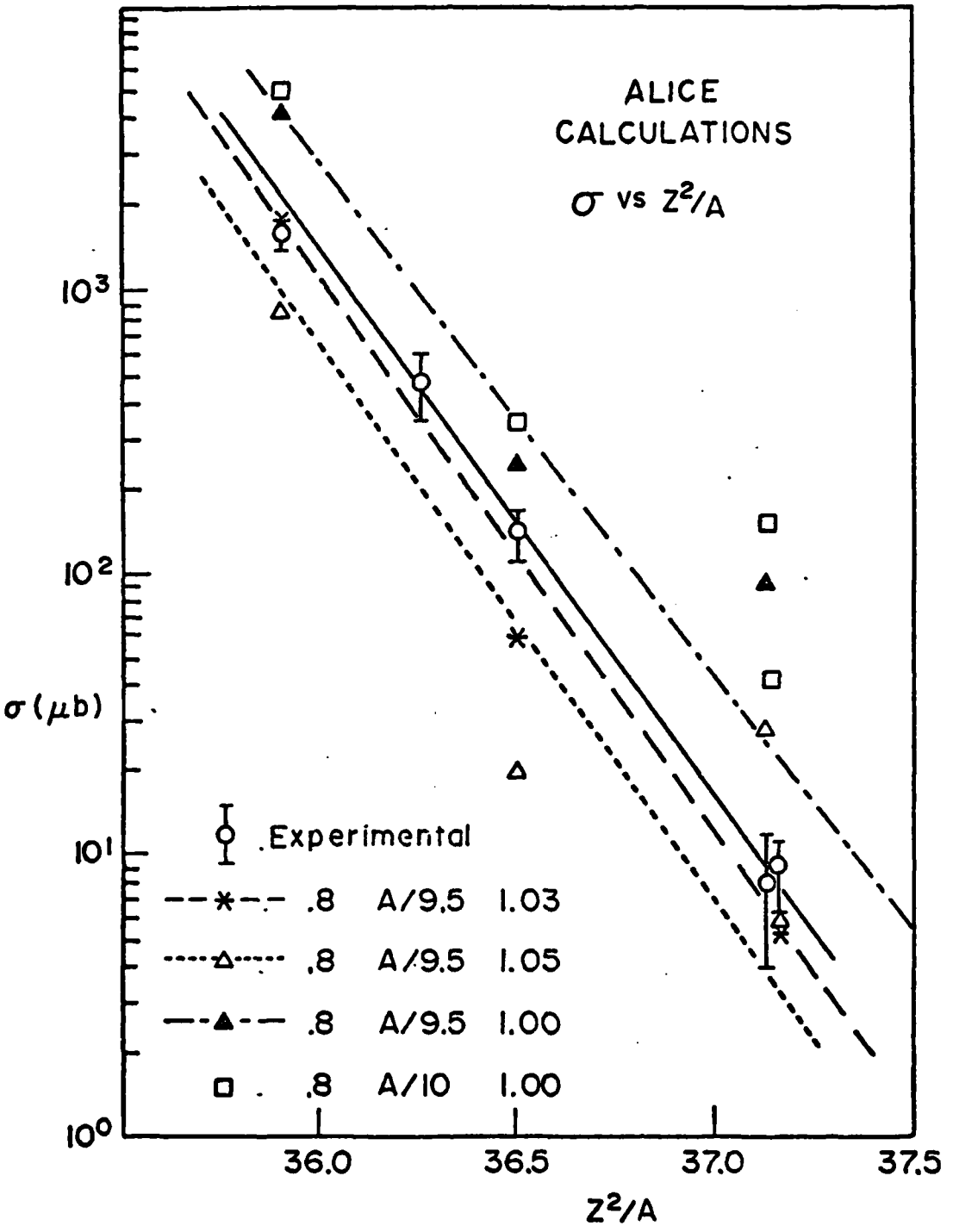
ALICE
CALCULATIONS
σ vs Z²/A
10³
10²
10¹
10⁰
σ (μb)
Experimental
.8 A/9.5 1.03
.8 A/9.5 1.05
.8 A/9.5 1.00
.8 A/10 1.00
36.0
36.5
37.0
37.5
Z²/A

FIGURE 54

values for use in more sophisticated statistical evaporation codes such as CASCADE or MBII. The ℓ-crit values change for different lab energies and figure 5 shows the total $d\sigma/dl$ versus ℓ plots for the reactions studied only at the peak experimental cross section value. The corresponding portions of the total fusion cross section that survive fission are shown in figure 6. Note the scale changes and the multiplicative factor of the evaporation portions. This demonstrates that only about 10^{-5} to 10^{-4} of the systems survives fission depending on the reaction studied. It also shows that at high angular momentum states, here with an ℓ value greater than 30, the chance of a compound nucleus surviving fission is negligible. Below 30, it demonstrates that fission is still the dominant process at all values with evaporation remaining only a very small part of the total cross section.

ALICE, then, has been shown to be an effective tool in the prediction of <u>total</u> evaporation residue formation in heavy ion fusion reactions. It is not adequate in the prediction of specific modes of evaporation, however. Parameters can be selected that match various specific evaporations, but there has been little success in matching total and specific evaporations.

The purpose of this study has been to chart the expected decrease in evaporation cross section with an increase in Z^2/A. The proton number was varied from 86 to 91 and the atomic number from 204 to 223. In this small range from Z^2/A of 35.9 to 37.2, the cross section for the survival against fission of a compound nucleus

decreased by a factor of 200. The ALICE code, using 10 different parameter sets, correctly paralleled this decrease and confirmed in the heavier region, a parameter set used with success in the lighter systems. The trends charted in this study must be reversed or the detection machinery improved if heavier systems with even higher Z^2/A are to be studied. Currently the Heavy Ion Group has initiated projects to determine the dependence on excitation energy (cold nucleus) and on shell effects ($^{40}Ca + {}^{160,162,163,164}Dy$), since there seems to be a dependence upon both the configuration and the excitation in regards to the stability of the compound system. Hopefully this study has shown the feasibility of continued study of the production of heavy compound systems and the possibility of continuation of that study into heavier domains.

REFERENCES

1. G.N. Flerov, in Proceedings of the European Conference on Nuclear Physics, (Aix en Provence), Vols. I and II, Journal de Physique, Paris (1972).

2. A. Marinov, C.K. Batty, A.I. Kilvingon, G.W.A. Newton, V.J. Robinson and J.D. Hemingway, Nature, London, 229, 464 (1971).

3. Hodgson, Nuclear Heavy Ion Reactions, Ch. 4, Oxford, 1978.

4. Ibid.

5. M. Beckerman, unpublished.

6. M. Blann and F. Plasil, ALICE: A Nuclear Evaporation Code, U.S. Atomic Energy Commission Report, No. COO-3494-10, 1973 (unpublished).

7. C. Bolton, W. Schier, H. Tsoupas, H. Enge, M. Salomaa, A. Sperduto and A. Grove, Mass, Velocity Angular and Charge-State Distributions from the Fusion of ^{32}S and ^{112}Sn, Physical Review C, Vol. 18, No. 1, July 1978.

8. H. Enge, private communication.

9. M. Lefort, Nuclear Fusion Between Heavy Ions, Reports on Progress in Physics 24, 129-173 (1976).

10. S. Cohen, F. Plasil and W.J. Swiatecki, Ann. Phys. 82, 557 (1974).

11. Ibid., M. Lefort.

12. R. Bass, Phys. Lett. 47B, 139 (1973).

13. Ibid., M. Lefort.

14. Ibid., Hodgson.

15. V.F. Weisskopf and D.H. Ewing, Phys. Rev. 57, 472 (1940).

16. D.W. Lang, Nucl. Phys. 42, 353 (1963); Nucl. Phys. 77, 545 (1966).

17. T.D. Thomas, A. Rev. Nucl. Sci. 18, 343 (1968).

18. J.R. Grover and J. Gelat, Phys. Rev. 157, 802 (1967).

19. Ibid., S. Cohen.

20. D. Horn, Heavy Ion Reactions with Proton Rich Nuclei, (Ph.D. Thesis, Mass. Inst. of Tech., August 1976).

21. F.G. Perey, Phys. Rev. 131, 745 (1963).

22. D. Wilmore and P. Hodgson, Nucl. Phys. 55, 673 (1964).

23. J.R. Huizenga and G. Iog, Nucl. Phys. 29, 462 (1961).

24. W.D. Myers and W.J. Swiatecki, Nuclear Masses and Deformations, Nuc. Phys. 81, 1-60 (1966).

25. M. Beckerman and M. Blann, MB-II A Statistical Fission/Evaporation Code for Treating Spin Dependent Level Densities with Explicit Angular Momentum Coupling, U. Rochester, Report #UR-NSRL-135A, March 1977.

26. Ibid.

27. Ibid., S. Cohen.

28. Ibid., M. Beckerman.

29. Ibid., C. Bolton.

30. H.C. Britt and A.R. Quinton, Phys. Rev. 3, 124 (Nov. 1961).

31. H.D. Betz, G. Hortig, E. Leischner, Ch. Schmelzer, B. Stadler and J. Weilrauch, Phys. Lett 22, 643 (1966).

32. V.S. Nikolaev and I.S. Smitriev, Phys. Lett. 28A, 277 (1968).

33. J.M. Levine, Heavy Nuclei, Superheavy Nuclei and Neutron Stars, Oxford Univ. Press, 1975.

34. M. Salomaa, H. Enge, Nuc. Inst. and Methods, 145, 271-277 (1977).

35. H. Enge and D. Horn, Nucl. Inst. and Methods. 145, 277-282 (1977).

36. H. Enge, Rev. Sci. Inst. 35, 278 (1964).

37. H. Enge, Nucl. Inst. and Methods. 162, 161-180 (1979).

38. R.G. Markhorn, S.M. Austin and H. Laumer, Nucl. Inst. and Methods 129, 141-145 (1975).

39. H. Enge, D. Grogan, A. Sperduto, M. Salomaa, A. DiRienzo and W. Schier, Bull. of Amer. Phys. Soc. 24, 14 (1979).

40. A. DiRienzo, H. Enge, S. Gazes, M. Salomaa, A. Sperduto, H. Wegner and W. Schier, to be published in Physical Review C.

41. F. Van Spluntern, Evaporation Residue Cross Section Calculations for A > 190 Compound Nuclei Formed in Heavy-Ion Fusion Reactions, (M.S. Thesis, Univ. of Lowell, Mass 1979).


DATE
FILME
7-8